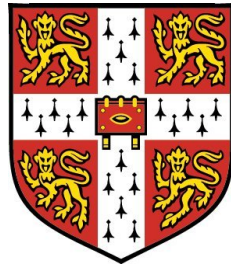


# The Capillary Interaction Between Objects at Liquid Interfaces



Pestheruwe Liyanaralage Himantha Manoj Cooray

Churchill College

University of Cambridge

A thesis submitted for the degree of

*Doctor of Philosophy*

February 2013



I hereby declare that this thesis is the result of my own work and includes nothing which is the outcome of work done in collaboration except where declared in the Acknowledgments and specified in the text.

This thesis is submitted for the degree of Doctor of Philosophy at the University of Cambridge. No part of this work has been submitted, or, is being concurrently submitted for a degree, diploma or other qualification at the University of Cambridge or any other University. The thesis contains less than 60,000 words.

Parts of this work have been presented in the following publication:

*The capillary interaction between two vertical cylinders,*  
Himantha Cooray, Pietro Cicuta, and Dominic Vella,  
Journal of Physics: Condensed Matter **24**, 28 (2012): 284104.

P.L. Himantha Manoj Cooray  
Cambridge, February 2013



# Acknowledgments

I am extremely grateful for my supervisors, Pietro Cicutta and Dominic Vella, for the continuous inspiration, guidance and motivation they gave me throughout my time as a PhD student. I must especially thank them for their patience and trust towards me. They immensely helped me improve my research skills and knowledge, gave me the freedom to select research directions, and also provided many important comments on drafts of this thesis.

I am also grateful to J. Li, who encouraged me and gave useful advice on numerical methods, and to Martin Oettel and Martin Buzza for many helpful discussions. Thanks also go to Peter Saunders who carried out the experiments presented in section [6.2.2](#), and Jurij Kotar who helped with the experimental systems.

Owen Dunn kept the group's computer system running smoothly, which was a great help for my numerical work. I also thank the other administrative and support staff of the BSS, including Pete Bone, Suresh Mistry, Tracy Inman, Sarah Adderley and Stefani Gerber for their work which enabled my research to be carried out efficiently. I appreciate the helps by the staff and fellows of the Churchill College including Barry Kingston, Philip Gaskell and Rebecca Sawalmeh who made my life in Cambridge easier.

I also thank my parents for the immeasurable support and encouragement they provided for my education throughout my life, without which I would not be able to come to Cambridge. I am also grateful to Nimalika Perera for always keeping me motivated and taking pains to make sure that I ate well. Thanks to my officemates including Simon Wongsuwarn, Elodie Aumaitre, Sarra Achouri, Catalin Chimerele, and Nicholas Thomson for being very good friends making my stay here pleasurable.

## Acknowledgments

---

I am really grateful for the funding support by the Cambridge Commonwealth trust and Overseas Research Students Awards Scheme which enabled me to become a student at Cambridge. I also appreciate the additional financial support by Churchill College, Department of Physics, Cambridge Philosophical Society and Lundgren Fund.

*To my supervisors, Pietro and Dominic,  
for their kindness and endless support.*



# Contents

<b>Overview</b>	<b>xi</b>
Summary . . . . .	xi
Structure of the thesis . . . . .	xiii
<b>1 Motivation and background</b>	<b>1</b>
1.1 Capillary interactions in the natural world . . . . .	1
1.2 Studies on capillary aggregation and self-assembly . . . . .	3
1.3 Different types of capillary interactions . . . . .	4
<b>2 Fundamentals of interface shapes</b>	<b>11</b>
2.1 Shape of a liquid–fluid interface . . . . .	11
2.1.1 Deriving the Laplace–Young equation . . . . .	11
2.1.2 Young’s law . . . . .	14
2.1.3 Boundary conditions for the Laplace–Young equation . . . . .	16
2.2 Complications for objects floating at a liquid–fluid interface . . . . .	17
2.3 Numerical methods for solving the Laplace–Young equation . . . . .	18
2.3.1 Principles of the <i>hp</i> -Meshless Cloud Method . . . . .	19
2.3.2 Adaptations and implementation of the <i>hp</i> -Meshless Cloud Method: . . . . .	24
2.A Derivation of the Young’s law . . . . .	27
<b>3 The capillary interaction between vertical cylinders at a liquid– fluid interface</b>	<b>29</b>
3.1 Theoretical Setting . . . . .	30
3.2 Existing Asymptotic Results . . . . .	35

3.2.1	Some simplifications . . . . .	35
3.2.2	Long-Range Asymptotic Solution . . . . .	35
3.2.3	Short-Range Asymptotic Solution . . . . .	37
3.3	Numerical Solution of the meniscus profiles . . . . .	38
3.4	Force of interaction between vertical cylinders . . . . .	40
3.5	Concluding remarks on vertical circular cylinders . . . . .	44
<b>4</b>	<b>Elliptical cylinders at a liquid–gas interface</b>	<b>47</b>
4.1	Theoretical setting . . . . .	50
4.2	Solution for small interface deformations . . . . .	53
4.2.1	The linearized Laplace–Young equation and the boundary condition in elliptic cylindrical coordinates . . . . .	53
4.2.2	Solution by separation of variables . . . . .	54
4.2.3	Asymptotic calculation of the force of attraction . . . . .	63
4.3	Approximation of the meniscus far away from the cylinder . . . . .	68
4.4	Numerical solution of the nonlinear Laplace–Young equation . . . . .	71
4.5	Numerical determination of the forces of attraction . . . . .	75
4.5.1	Force due to surface tension . . . . .	75
4.5.2	Force due to hydrostatic pressure . . . . .	77
4.5.3	Total force of attraction . . . . .	78
4.6	Concluding remarks on elliptical cylinders . . . . .	78
4.A	Deriving the linearized boundary condition (Eq. 4.14) for the menis- cus around an elliptical cylinder . . . . .	80
<b>5</b>	<b>Floating (and sinking) of spheres at a liquid–fluid interface</b>	<b>81</b>
5.1	An isolated sphere . . . . .	83
5.2	Theoretical setting . . . . .	86
5.2.1	Geometrical considerations . . . . .	86
5.2.2	Forces acting on a sphere . . . . .	88
5.2.2.1	Force due to hydrostatic pressure . . . . .	88
5.2.2.2	Force due to surface tension . . . . .	90
5.2.3	Vertical balance for floating . . . . .	92
5.2.4	Meniscus profile around the spheres . . . . .	92

5.3	Numerical solution of force balance and Laplace–Young equation . . . . .	93
5.4	Semi-analytical solution . . . . .	96
5.5	Maximum density of an isolated floating sphere . . . . .	99
5.5.1	Calculation neglecting buoyancy . . . . .	99
5.5.2	Calculation considering buoyancy . . . . .	101
5.6	Vertical equilibrium of a pair of identical spheres . . . . .	102
5.6.1	Semi-analytical solution . . . . .	102
5.6.2	Numerical solution of two spheres . . . . .	103
5.7	Vertical equilibrium of a hexagonal lattice of spheres . . . . .	106
5.8	Concluding remarks on the floating and sinking of spheres . . . . .	111
<b>6</b>	<b>The capillary attraction between pairs of floating particles</b>	<b>113</b>
6.1	Asymptotic results for flotation interactions . . . . .	115
6.2	Experiments on the behaviour of floating spheres . . . . .	116
6.2.1	Determination of the contact angle . . . . .	116
6.2.2	Experiments on velocities of attraction . . . . .	117
6.2.2.1	Materials and methods . . . . .	117
6.2.2.2	Image analysis, particle tracking and velocity calculation . . . . .	119
6.2.3	Experimental determination of the force of capillary interaction . . . . .	121
6.3	Numerical determination of the attraction between floating spheres	125
6.4	Limitations of the expression for the hydrodynamic interaction . . .	126
6.5	Concluding remarks on attraction between floating particles . . . . .	128
<b>7</b>	<b>Epilogue</b>	<b>129</b>
7.1	Conclusions . . . . .	129
7.2	Outlook . . . . .	132
	<b>References</b>	<b>137</b>



# Overview

## Summary

This thesis reports numerical and analytical results on the floatation and capillary interaction of granular-sized objects at liquid–fluid interfaces. Such objects create deformations at the liquid surfaces which result in their interaction with each other. It has been experimentally shown that this effect can be used for self-assembly of ordered structures, and there are examples in the natural world too.

The deformation created by a solid object at a liquid interface is governed by the Laplace-Young equation and appropriate boundary conditions. This is a nonlinear differential equation which is hard in general to solve analytically, and only approximate solutions exist for most of the interesting cases. We develop a new numerical solution to determine the shape of a liquid interface in the vicinity of multiple solid objects using the *hp*-Meshless Cloud method, which is a meshfree finite difference method. This solves the nonlinear Laplace-Young equation without any approximations.

First a system is considered where circular cylinders are immersed in a liquid. The meniscus shape is determined, and the force of interaction between a pair of cylinders is calculated as a function of the distance between them. The results are compared with previously published asymptotic solutions and experimental results. When the cylinders are sufficiently far apart, the experimental results agree with both the numerical and asymptotic results. However, as the cylinders move closer, the asymptotic solution is unable to explain the experimental results because this solution is valid only in regions with small meniscus slopes. In contrast, the numerical solution is able to accurately explain the experimental results at all distance ranges.

The numerical solution is further extended to solve for two elliptical cylinders at a liquid interface. Additionally, a new analytical solution is also developed for this problem. For the case of an isolated cylinder, this analytical solution is able to predict the same contact line shapes and meniscus profiles as the numerical solution. Both the solutions show that the force of attraction between a pair of elliptical cylinders is larger when they are in the tip-to-tip orientation, and smaller in the side-to-side orientation. The difference between the forces in the two orientations diminishes at large inter-cylinder separations. It is also shown that the meniscus far away from an elliptical cylinder is same as one created by a circular cylinder with perimeter equal to that of the elliptical cylinder.

The numerical solution is further developed to solve for multiple floating spheres. This is a complicated condition compared to the vertical cylinders because the vertical locations of the spheres and the horizontal projections of the three-phase contact lines are not known *a priori*. A new algorithm is developed to simultaneously satisfy the force balance, Laplace-Young equation and the geometric properties of the spheres. This shows that floating and sinking of a pair of spheres can depend on their relative positions. An unexpected and new result is obtained: at an intermediate inter-particle distance range, a sphere that would sink in isolation can float as a part of a pair or a cluster. A simple and new semi-analytical solution is also developed, which also predicts the same behaviour. Additionally, the numerical solution predicts that a sphere that would float in isolation would sink as a part of a pair at very small inter-particle distances.

This numerical solution is then extended to determine the force of attraction between pairs of floating spheres. This is studied experimentally as well, by tracking the movement of particles at a liquid interface. Asymptotic solutions have previously been published for this problem. The numerical solution shows that the force deviates from the predictions of these asymptotic expressions when the density of the spheres is high. At small densities such as those used in the experiments, the asymptotic solutions correctly predict the force of attraction.

## Structure of the thesis

Different types of capillary interactions are introduced in Chapter 1, with a review of previous experimental and theoretical studies in this discipline. Chapter 2 presents the theoretical fundamentals governing the capillary interactions, and describes the derivation of the basic equations. This chapter also describes the numerical method that I use to solve the nonlinear Laplace–Young equation.

In Chapter 3, I provide the numerically obtained results for the force of capillary interaction between pairs of vertical circular cylinders at a liquid interface. These results are compared with experimental results and asymptotic solutions previously published by other groups.

Chapter 4 provides an extension of the numerical method to determine the capillary interaction between elliptical cylinders. A new asymptotic solution is also developed for this problem.

Chapter 5 presents a method for solving a more complicated problem: the capillary interaction between floating spheres. Using this solution, it is shown that the floating and sinking behaviour of a sphere can be affected by the presence of other spheres in its vicinity. A new “semi-analytical” solution that approximates this behaviour is also developed.

Using the numerical solution presented in Chapter 5, the force of attraction between floating spheres is determined in Chapter 6. This chapter also presents experiments where the attraction between floating particles was studied.

In Chapter 7, conclusions are made summarizing the major results. It also reviews a range of future research which can be carried out based on the results and methods presented in this thesis.



# Chapter 1

## Motivation and background

A solid object at an otherwise planar liquid–fluid interface can produce interfacial deformations due to its boundary conditions, i.e. by imposing height variations along a three-phase contact line or by imposing a non-zero derivative condition on the interface along this contact line. A deformed interface can exert forces, resulting in “capillary interactions” between such objects (Binks and Horozov, 2006). These interactions are ubiquitous and strong compared to interactions due to electrostatic and thermal effects.

The work presented in this thesis deals with capillary interactions between objects well above the colloidal scale, in the granular regime. Since these objects are larger than tens of micrometers, they are not significantly affected by the thermal and electrostatic forces. However, they are still small compared to the *capillary length*, the length scale in which the interfacial deformations take effect. (For an air–water interface, this value is approximately 2.7 mm). Objects in this size range are predominantly affected by capillary forces when placed at a liquid–fluid interface.

### 1.1 Capillary interactions in the natural world

Capillary forces result in a wide range of remarkable phenomena in nature from plants and animals to inorganic systems. The most popular example is the insects known as “water striders” which are capable of walking on water supporting

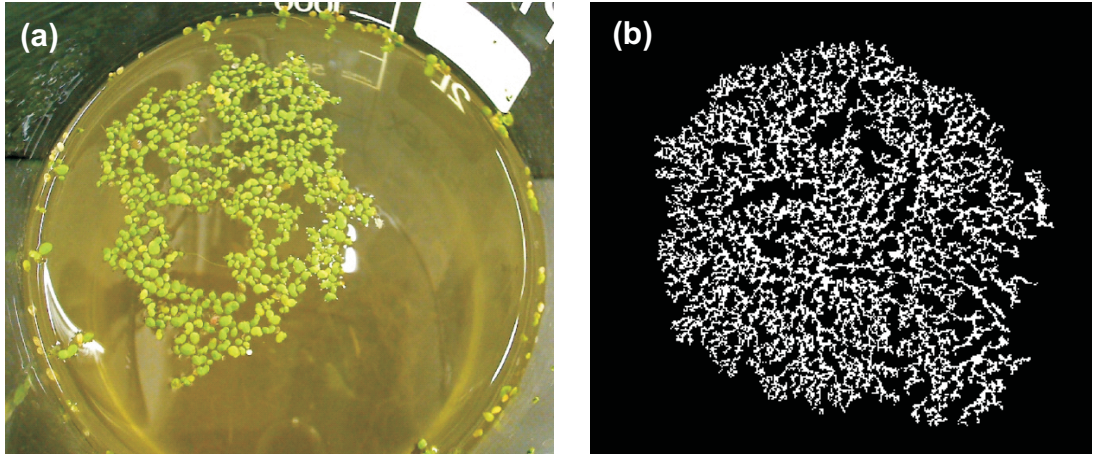


Figure 1.1: Objects supported by the surface tension of water interact due to capillary forces and tend to produce aggregates. The figure shows two examples I investigated: (a) is an aggregate produced by growing duckweed (diameter  $\approx 2\text{ mm}$ ), and (b) is produced by Pliolite rubber particles (diameter  $\approx 0.3\text{ mm}$ ).

their weight by means of surface tension (Gao and Jiang, 2004). Objects thus supported by means of surface tension at a liquid–fluid interface create interfacial deformations, which may result in “capillary attraction” forces between them if they are in the vicinity of each other. An example is duckweed, which is a small plant that grows on surfaces of ponds during summer, and aggregates to produce clusters that can eventually grow to cover the whole surface of a pond. This effect was reported by Miall (1898), and figure 1.1(a) shows such an aggregate produced by duckweed growing in the laboratory. Capillary–induced aggregation processes also have impacts for bigger plants that disperse their seeds by water, i.e. hydrochory. Chambert and James (2008) showed that seeds with pointed ends can get attached to vertical surfaces, such as plant stems, because of capillary attraction. This is also true in the animal kingdom, where mosquitoes lay their eggs as interfacial aggregates whose form depend on the species (Christophers, 1945; Hinton, 1968; Saliternik, 1942). Using synthetic particles of a shape similar to mosquito eggs, Loudet and Pouligny (2011) studied the capillary forces that lead to this aggregation process. It is thought that this brings an advantage to the mosquito eggs because upon the aggregation, they can then collectively attach to a stable structure and remain safe.

## 1.2 Studies on capillary aggregation and self-assembly

In addition to natural objects, man-made granular-sized objects also show exciting aggregation behaviour. Figure 1.1(b) is such a cluster produced by capillary interaction of rough Pliolite rubber particles on water. [Hórvölgyi et al. \(1991\)](#) studied such aggregates produced by glass beads on water and observed that the clusters undergo further secondary packing after aggregation. They also reported that smaller aggregates demonstrated fractal properties while larger aggregates crossed over to non-fractal nature.

Sheets of these aggregates are known as “particle rafts” and their mechanical properties have been studied (see [Cicuta and Vella \(2009\)](#), for example) by compressing them in a Langmuir trough. They found that the stress profile in this two-dimensional particle monolayer was analogous to that of three-dimensional granular systems. [Berhanu and Kudrolli \(2010\)](#) employed a different experimental procedure for compressing the particle aggregates by moving them downwards through a conical funnel, and analyzed how the heterogeneity of the clusters varied.

The process of capillary aggregation in a circular domain was numerically and analytically studied by [Bleibel et al. \(2011\)](#). When the range of interaction between pairs of particles was large compared to the domain size, the whole system aggregated into one single cluster. At smaller ranges of interaction, they produced ring-like pre-clusters which then moved towards the centre. For capillary forces, this range of interaction is equivalent to the capillary length, which will be described in section 2.1.1 ( Eq. 2.10). [Lukaschuk et al. \(2006\)](#) analyzed the process of capillary aggregation of particles in the presence of surface waves and reported that the particles preferentially moved to nodes or antinodes of the waves. [Han and Kim \(2012\)](#) used dumbbell-shaped plates on the surface of water to produce clusters and studied how the packing behavior varied with the shape of the plates.

In contrast to random aggregates mentioned above, one can tune the geometry and surface properties of the individual “building blocks” to enable capillary self

assembly and produce ordered structures. [Hosokawa et al. \(1996\)](#) first used this method to produce thin film micro-structures by self-assembly of small objects floating on water. In addition to attractive capillary forces, they also utilized repulsive capillary forces. This was achieved by having some objects flat, which created downwards deformations of the liquid surface, and having some objects curled-up at the edges to create upwards surface deformations. Further self-assembly experiments were carried out by [Bowden et al. \(1997, 1999, 2000\)](#) where hexagonal building blocks with hydrophilic and hydrophobic faces were used to produce ordered structures.

Capillary forces can also be utilized for self-assembly in three dimensions. [Clark et al. \(2001\)](#) used metallic polyhedral plates with specifically designed hydrophobic and hydrophilic faces. A thermally curing hydrophobic adhesive was added to the hydrophobic sides, and the plates were stirred inside water. The adhesive binded the hydrophobic faces by means of capillary forces until it was cured to produce a stable structure. [Clark et al. \(2002\)](#) introduced an improvement to this process by using a template to control the size and shape of the final structures produced. The templates were circular metal plates with internal cavities, in which the building blocks assembled. Such capillary-based self assembly methods were reviewed by ([Mastrangeli et al., 2009](#); [Syms et al., 2003](#)). Examples of structures produced by such processes include assemblies of micromirrors ([Srinivasan et al., 2002](#)), inductors ([Scott et al., 2004](#)), and LEDs ([Xiong et al., 2003](#)).

### 1.3 Different types of capillary interactions

Understanding the forces of capillary interaction is crucial for the study of the above phenomena. [Kralchevsky and Nagayama \(2000\)](#) and [Kralchevsky and Denkov \(2001\)](#) classified the capillary interaction forces into several categories, which are schematically shown in figure 1.2. The two main classes of forces are normal capillary forces and lateral capillary forces. For a pair of objects at a liquid-fluid interfaces, a normal capillary force acts normal to the contact line and a lateral capillary force acts approximately along the contact line. A review on normal capillary forces can be found in [Butt and Kappl \(2009\)](#). These forces

### 1.3. Different types of capillary interactions

---

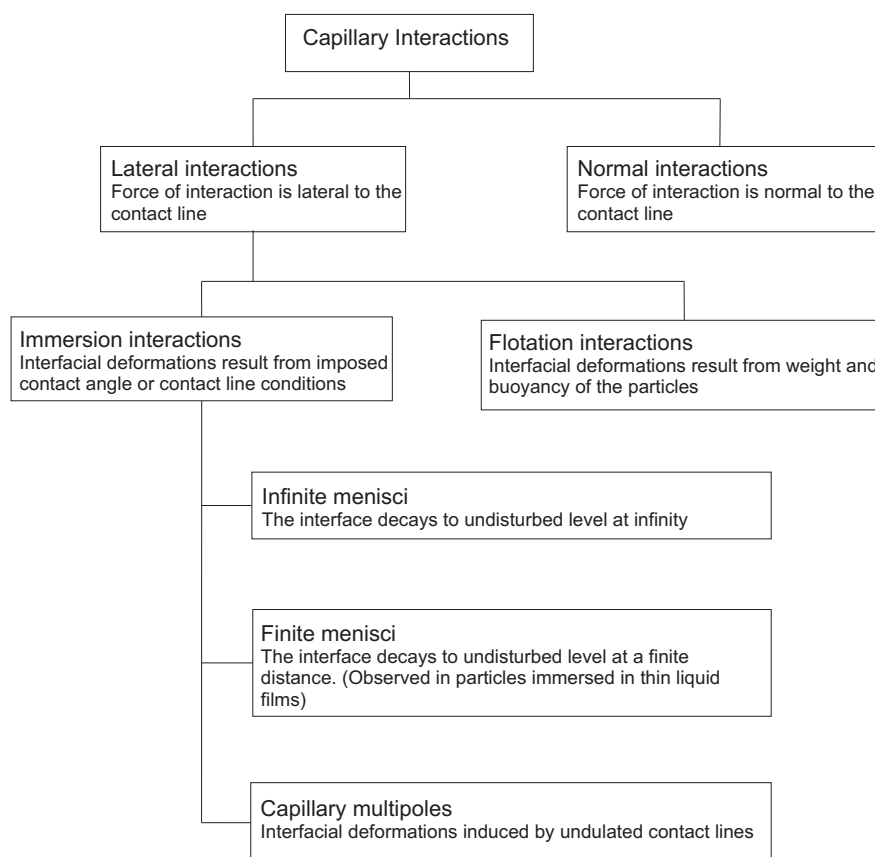


Figure 1.2: Types of capillary interactions, as classified by [Kralchevsky and Nagayama \(2000\)](#) and [Kralchevsky and Denkov \(2001\)](#). The analyses in this thesis focus on lateral capillary interactions: in particular, flotation interactions and infinite menisci immersion interactions.

result from “liquid bridges” that cause adhesion between solid particles, as shown in figure 1.3. This is commonly experienced in building sand castles using wet sand. Industrially, this is a crucial aspect to be taken care of, in avoiding wetting and lumping of hygroscopic powders such as sugar and fertilizer by condensation of atmospheric moisture. Non-volatile liquids can also produce normal capillary forces by forming a thin film on each particle, and then interconnecting many particles. An example is lubricants on bearing balls. In addition to particles in air, particles suspended in a liquid can also be affected by normal capillary forces. In this case, a different liquid which is miscible with the first liquid can create liquid bridges among the particles which then cause aggregation of particles that

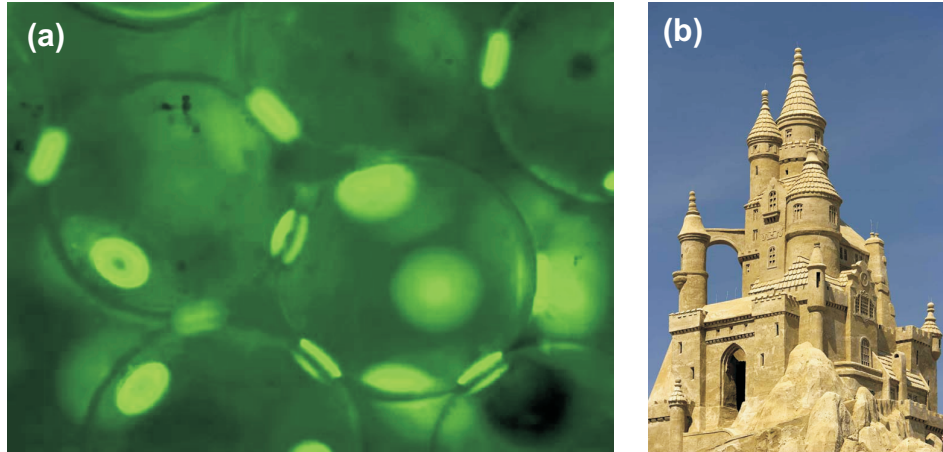


Figure 1.3: A liquid can create “capillary bridges” among solid particles that result in forces of adhesion. (a) is a fluorescence microscopic image showing capillary bridges created by water linking glass spheres with diameter  $\approx 100 \mu\text{m}$ . (Reprinted from [Herminghaus \(2005\)](#)). (b) shows a sand castle where the grains of sand are held together by capillary forces resulting from water bridges interconnecting them. (Reprinted from [Schiffer \(2005\)](#))

come close to each other due to Brownian motion ([Bloomquist and Shutt, 1940](#); [Butt and Kappl, 2009](#)).

The forces of capillary interaction analyzed in this thesis are lateral capillary interactions, which are divided into flotation forces and immersion forces ([Kralchevsky and Denkov, 2001](#); [Kralchevsky and Nagayama, 2000](#)). For a particle floating at a liquid–fluid interface, the weight needs to be balanced by buoyancy and surface tension. The interfacial deformation resulting from this requirement gives rise to lateral capillary forces. The earliest study of these forces was by [Nicolson \(1949\)](#) where the forces of interaction between bubbles at a liquid interface was analytically calculated using the approximation of linear superposition. Using the same approximation, [Chan et al. \(1981\)](#) developed asymptotic expressions for the forces of attraction between a pair of spherical particles and between a pair of infinitely long horizontal cylinders floating at a liquid–fluid interface. [Paunov et al. \(1993\)](#) developed another analytical solution valid for the attraction between spheres that are small in comparison to the capillary length. They did not use the linear superposition approximation, and solved the problem in bipolar coordinates instead, assuming small meniscus slopes. At large

inter-particle distances, their result reduces to the one developed by [Chan et al. \(1981\)](#).

Flotation forces have been experimentally studied by [Dalbe et al. \(2011\)](#); [Vassileva et al. \(2005\)](#). They measured the relative velocities of pairs of floating spherical particles by means of particle tracking, and compared this with an analytical expression obtained using the asymptotic result for the capillary attraction ([Chan et al., 1981](#)) and the hydrodynamic interaction between the spheres ([Batchelor, 1976](#)).

Knowing whether a particle will float or sink under a given set of conditions is also important. [Vella et al. \(2006a\)](#) studied this analytically and experimentally for cylinders and numerically for spheres, and determined the maximum load that these objects can support without sinking. Further experimental studies of this problem were done by [Extrand and Moon \(2009\)](#); [Kim et al. \(2010\)](#). While these studies were for isolated floating objects, the floating conditions may be different when a pair of objects are interacting, as shown by [Vella et al. \(2006b\)](#) for a pair of infinitely long horizontal cylinders. Their numerical solution showed that it is possible for cylinders that float at large separations to sink as they approach one another.

In contrast to flotation forces resulting from the vertical force balance requirement, capillary immersion forces result from the contact angles or fixed contact lines imposed by objects at liquid–fluid interfaces. An example is the interaction between a pair of vertical cylinders. In the limit of small meniscus deformations, [Kralchevsky et al. \(1993\)](#) analytically calculated the force of attraction between these objects and [Ceco et al. \(1996\)](#); [Velev et al. \(1993\)](#) experimentally measured the force between pairs of glass cylinders at a liquid interface by means of a torsion microbalance. Immersion forces can also act between spheres resting on a flat solid surface partially covered with a thin liquid layer. [Maenosono et al. \(1999\)](#) analyzed the relative movement of such spheres using video microscopy, and using the theoretical results for the capillary attraction by [Kralchevsky and Nagayama \(1994\)](#), calculated the viscous drag force which counterbalanced this capillary force. Capillary attraction and aggregation has also been observed between particles trapped in foam films that are much smaller in thickness (100 times thinner) compared to the size of the particles ([Velikov et al., 1998](#)). [Gart](#)

[et al. \(2011\)](#) developed a theoretical argument to show that in these cases, the interfacial deformations decay to zero at a finite distance away from a particle, and hence, these are called “finite menisci” in contrast to usual menisci which decay at infinity.

The particles can also be trapped in a curved liquid interface. Such systems are industrially used in Pickering emulsions ([Denkov et al., 1992](#); [Pickering, 1907](#)), and can also occur in vesicles and biomembranes. The adsorbed particles can change the shape of the interface and result in interactions. [Kralchevsky et al. \(1995b\)](#) determined the interaction between particles trapped in a thin spherical liquid film by numerically solving the linearized Laplace–Young equation, with the particles imposing fixed contact angle conditions and fixed contact line conditions separately. Capillary interactions can also occur between objects as small as protein molecules in biomembranes. Although the weight of these molecules are too small to create meniscus deformations, their inhomogeneous wetting conditions can deform the interface. This was studied theoretically by [Gil et al. \(1998\)](#); [Kralchevsky et al. \(1995a\)](#) and experimentally by [Mansfield et al. \(1999\)](#). [Zeng et al. \(2012\)](#) theoretically studied capillary forces between spherical particles trapped at anisotropically curved interfaces. These studies were in the parameter range where the weight of the particles were negligible. The effect of the weight may give rise to more interesting phenomena ([Zeng et al., 2012](#)).

[Paunov et al. \(1992\)](#) theoretically showed that a special type of interaction can occur between a vertical wall and a partially immersed spherical particle or a vertical cylinder. If the contact angle of the wall is  $90^\circ$  forcing the meniscus slope to be zero in the direction normal to it, the particle feels the same attractive force as if it was interacting with its mirror image with respect to the wall. These forces are hence called “capillary image forces”. [Kralchevsky et al. \(1994\)](#) extended the theory of image forces to the interaction between a floating particle and a vertical wall, and proved that repulsive forces act if the wall has a flat contact line with zero height. They also showed that stable equilibrium positions of the sphere can exist at finite distances from the wall, which was also experimentally realized by [Velev et al. \(1994\)](#).

If the contact line around a particle is undulated, this can lead to capillary multipoles. Examples are rough, heterogeneous or non-spherical particles at a

flat liquid interface, and spherical particles at a curved interface. An early example for the study on this discipline is [Lucassen \(1992\)](#). [Danov and Kralchevsky \(2010\)](#); [Lucassen \(1992\)](#); [Stamou et al. \(2000\)](#) theoretically studied the force of attraction between capillary multipoles. The force between a pair of capillary multipoles generally depends on the mutual orientation and can result in rotation and alignment of the two particles. When capillary multipoles aggregate, they can produce patterns that depend on the order of the multipole. Particles with different orders of the multipole cannot produce a single lattice upon aggregation, and results in phase separation ([Kralchevsky and Denkov, 2001](#)). Because of the direction-dependent nature, capillary multipoles can be used effectively for the self assembly of ordered structures ([Bowden et al., 1997, 1999](#)).

Most of the theoretical studies mentioned above analyze the capillary interactions by solving the linearized Laplace–Young equation, which is valid only at small interfacial deformations, and often assume linear superposition of menisci created by individual objects. In contrast, I present accurate numerical solutions for the nonlinear Laplace–Young equation without using any such approximations. The following chapters demonstrate that the limitations of existing solutions, and new phenomena discovered using the new numerical solution. I also derive simpler analytical solutions for two problems, independently verifying the findings of the numerical solution. The thesis also presents experiments that were carried out to determine the forces of capillary interaction.



# Chapter 2

## Fundamentals of interface shapes

In this chapter, I introduce the Laplace–Young equation which governs the shape of a liquid–fluid interface. I then discuss boundary conditions for solving of the Laplace–Young equation in situations of interest, and the vertical force balance that enables objects to remain floating at a liquid–fluid interface.

### 2.1 Shape of a liquid–fluid interface

#### 2.1.1 Deriving the Laplace–Young equation

The shape of a liquid–fluid interface is governed by the Laplace–Young equation. In this section we reproduce the derivation of this equation (taken from [Butt et al. \(2003\)](#)), and then express it in Cartesian coordinates. Here the Laplace–Young equation is derived using the force balance on a small part of a liquid–fluid interface as shown in [figure 2.1](#). This equation can alternatively be derived using a thermodynamic approach, see for example [Roura \(2005\)](#).

In [figure 2.1](#),  $X$  is a point on the interface. The curve  $ACBD$  is the set of points located at a distance  $S$  from the point  $X$ . (This is same as the intersection between the interface and a sphere with radius  $S$  is drawn centred on  $X$ ). It is assumed that the interfacial region bounded by this curve is sufficiently small that the curvature in it is constant.  $AXB$  and  $CXD$  are two perpendicular lines placed on the interface.

This interfacial part is affected by two forces: force due to the surface tension

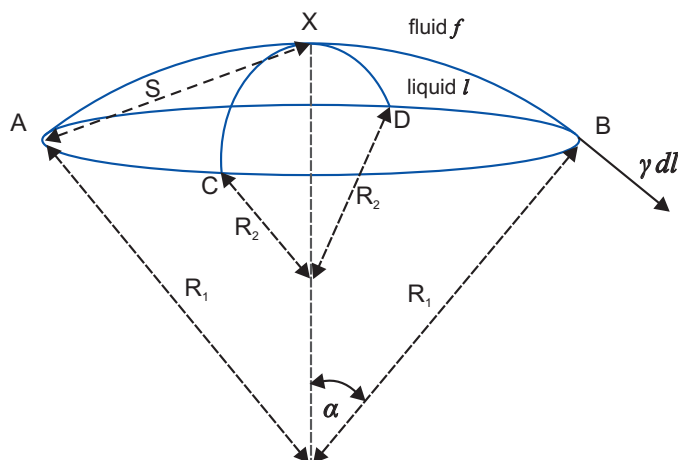


Figure 2.1: The Laplace–Young equation can be derived considering the force balance on the part of a liquid–fluid interface as shown here.

acting downwards, and force due to the pressure acting upwards. To achieve equilibrium, these two forces need to balance each other. If  $\gamma$  is the surface tension, the force of surface tension acting on a small line segment with length  $dl$  around  $B$  is  $\gamma dl$ , as marked in the figure. Hence the downward component of this force is  $\gamma dl \sin \alpha$ . For small sections, i.e.  $S \ll R_1, R_2$ ,

$$\sin \alpha \approx \frac{S}{R_1}, \quad (2.1)$$

with  $R_1$  is the radius of curvature along  $AXB$ . Then the vertical force is

$$\gamma \frac{S}{R_1} dl. \quad (2.2)$$

The sum of the vertical components of the force at points  $A, B, C$  and  $D$  along line segments of length  $dl$  is

$$dF = 2S\gamma \left( \frac{1}{R_1} + \frac{1}{R_2} \right) dl. \quad (2.3)$$

We know

$$\frac{1}{R_1} + \frac{1}{R_2} = -\kappa \quad (2.4)$$

where  $\kappa$  is the mean curvature which is independent of the orientations of  $AXB$

and  $BXD$  as long as they are orthogonal.  $\kappa$  is defined to be positive if the interface is convex towards the liquid. Combining Eq. (2.3) with Eq. (2.4) and integrating along one quadrant of the borderline gives the total downward surface tension force to be

$$F_\gamma = -\pi S^2 \gamma \kappa. \quad (2.5)$$

Next we consider the force acting on the concave side of the interface due to the pressure difference  $\Delta P = P_{liquid} - P_{fluid}$  between the two sides of the interface. This force is given by

$$F_{hp} = \pi S^2 \Delta P. \quad (2.6)$$

For the interface is in equilibrium,  $F_\gamma = F_{hp}$ , from which we deduce the Laplace–Young equation

$$\Delta P = -\gamma \kappa. \quad (2.7)$$

If the pressure difference is due to the density difference between the liquid and fluid phases,

$$\Delta P = -\zeta g \Delta \rho, \quad (2.8)$$

where  $\Delta \rho = \rho_l - \rho_f$  with  $\rho_l$  and  $\rho_f$  are the densities of the liquid and fluid phases,  $g$  is the acceleration due to gravity and  $\zeta$  is the height of the interface from a point where the pressure difference across the interface (or the curvature according to Eq. 2.7) is zero. Substituting this into Eq. (2.7) gives

$$\zeta = \kappa \frac{\gamma}{\Delta \rho g}. \quad (2.9)$$

Introducing the capillary length defined by

$$\ell_c = \sqrt{\frac{\gamma}{\Delta \rho g}}, \quad (2.10)$$

Eq. (2.9) may be written

$$\zeta = \kappa \ell_c^2. \quad (2.11)$$

If the depth  $\zeta$  is given as a function of  $x$  and  $y$ , which are Cartesian coordinates,

the mean curvature (Pozrikidis, 2009) is given by

$$\kappa = -\frac{\zeta_{xx}(1 + \zeta_y^2) + \zeta_{yy}(1 + \zeta_x^2) - 2\zeta_{xy}\zeta_x\zeta_y}{2(1 + \zeta_x^2 + \zeta_y^2)^{\frac{3}{2}}}, \quad (2.12)$$

where the subscripts denote derivatives with respect to  $x$  and  $y$ . This equation can be converted to other coordinate systems by expressing the curvature in the relevant coordinate systems (see Gray (1998), for example).

As described in section 1.3, there are several analytical solutions for the Laplace–Young equation where the problem is simplified by linearisation so that the interfacial deformation approximately satisfies:

$$\zeta = \ell_c^2 \nabla^2 \zeta. \quad (2.13)$$

This approximation is valid when the meniscus slopes are small:

$$\frac{\partial \zeta}{\partial x} \ll 1, \quad \frac{\partial \zeta}{\partial y} \ll 1. \quad (2.14)$$

There are a limited number of asymptotic solutions where the fully nonlinear Laplace–Young equation has been solved. An example is Lo (1983) where the shape of the meniscus around a vertical cylinder with a radius very small compared to the capillary length was solved. It is possible to solve the nonlinear Laplace–Young equation numerically for more complex boundaries, as done by Hill and Pozrikidis (2011); Pozrikidis (2010, 2011). However, there remains a wide range of interesting problems that have not been solved using the full Laplace–Young equation without using approximations such as Eq. (2.14). In this thesis, I present new findings from such solutions.

### 2.1.2 Young’s law

It is common to solve the Laplace–Young equation subject to a contact angle condition. This relies on the notion that the angle of contact for a given three-phase system is constant. This is a result due to Young (1805) and reproduced here based on an argument by Butt et al. (2003). For a more rigorous alternative

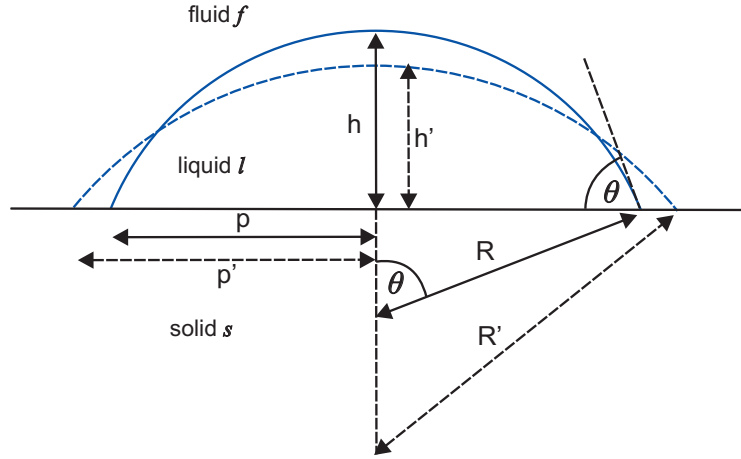


Figure 2.2: Schematic of a liquid droplet resting on a solid plane, surrounded by a fluid. Young’s law can be derived considering the change of Gibb’s free energy resulting from an infinitesimal spreading of this drop.

derivation, see [Roura and Fort \(2004\)](#). This derivation is for a circular liquid drop on a plane solid surface, surrounded by a fluid. Then the change of Gibbs free energy (see [Butt et al. \(2003\)](#); [Roura and Fort \(2004\)](#), for example) resulting from the drop spreading by an infinitesimal amount is considered. It is assumed that the droplet is small enough that gravitational effects can be neglected, and that the droplet is large enough so that the curvature is small and the effect of the Laplace pressure on the Gibbs free energy is negligible. The droplet produces a three-phase contact line, around which there are three types of interfacial tensions. They are defined as  $\gamma_{sl}$ ,  $\gamma_{sf}$  and  $\gamma_{lf}$ , and they are for the solid–liquid, solid–fluid and liquid–fluid interfaces, respectively. Young’s law relates these surface tensions to the contact angle  $\theta$  at the three phase contact line, so that

$$\gamma_{sl} = \gamma_{sf} - \gamma_{lf} \cos \theta. \quad (2.15)$$

The derivation of this equation is given in Appendix [2.A](#).

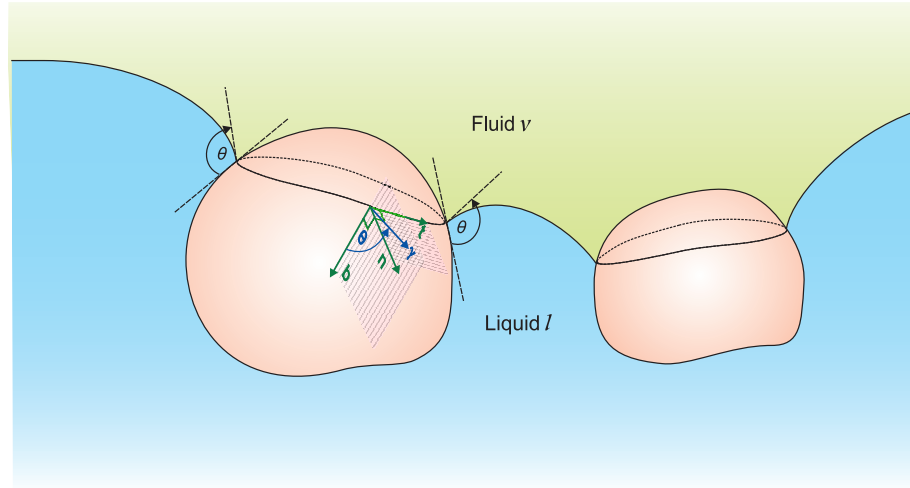


Figure 2.3: Schematic diagram of a pair of arbitrary objects at a liquid–fluid interface. The contact angle is defined on a vertical plane only if the contact line is flat. In general, it is defined on the plane containing vectors  $\mathbf{n}$  and  $\mathbf{b}$ .  $\mathbf{n}$  is the outward normal to the object surface and  $\mathbf{t}$  is the tangent to the contact line.  $\mathbf{b}$  is the binormal to  $\mathbf{n}$  and  $\mathbf{t}$ .  $\gamma$  is tangent to the liquid–fluid interface.

### 2.1.3 Boundary conditions for the Laplace–Young equation

For a meniscus in contact with a solid object, the appropriate boundary condition is a fixed contact angle  $\theta$ . In a simple case like a droplet on a flat surface as discussed in the previous section,  $\theta$  is the angle with which the surface of the droplet meets the solid surface. However, there are other cases where the contact angle cannot be implemented in a simple manner. Figure (2.3) shows a pair of solid bodies at a liquid–fluid interface, where the contact angle is non-trivial to express mathematically. In this case, we first define  $\mathbf{t}$  as the running tangent to the contact line,  $\mathbf{n}$  as the running outward normal to the object surface and  $\mathbf{b}$  as the binormal to  $\mathbf{t}$  and  $\mathbf{n}$  given by

$$\mathbf{b} = \mathbf{n} \times \mathbf{t}. \quad (2.16)$$

Then the contact angle is set with respect to the plane containing  $\mathbf{n}$  and  $\mathbf{b}$  (Kralchevsky et al., 1993). If  $\hat{\gamma}$  is the unit tangent to the liquid interface on

this plane and  $\hat{\mathbf{b}}$  is the unit binormal, then the contact angle boundary condition reads

$$\hat{\mathbf{b}} \cdot \hat{\boldsymbol{\gamma}} = \cos \theta \quad (2.17)$$

at the surface of the solid object.

For completeness, figure 2.3 also shows two points on the sides of the object where the contact line is flat. At these two points, the above boundary condition reduces to a special case where the contact angle is defined on a vertical plane. Such flat regions can result from the symmetry of the system.

The other boundary condition we use is the fact that the liquid–fluid interface must be undisturbed at an infinite distance from the solid bodies. (This is true in all analyses presented in this thesis except in section 5.7 where an infinite lattice of floating spheres is studied). This boundary condition is mathematically expressed as

$$\lim_{x,y \rightarrow \infty} \zeta(x,y) = 0, \quad (2.18)$$

where  $x, y$  are distances measured from the solid objects.

## 2.2 Complications for objects floating at a liquid–fluid interface

In contrast to solid bodies with fixed locations, if the objects are floating, their vertical locations, and as a result, the configuration of the three–phase contact line remain unknown *a priori*. The vertical forces need to be balanced as a part of the solution, and the interfacial torques also need to be taken into account. I present a new method of doing this for floating spheres in Chapter 5. In solving for floating spheres, the torque balance need not be considered because Singh and Hesla (2004) showed that the net torque acting on a sphere at a liquid interface is zero regardless of the shape of the contact line, provided that the contact angle is constant.

## 2.3 Numerical methods for solving the Laplace–Young equation

We first attempted solving the nonlinear Laplace–Young equation for the interface shape between two interfacial objects using the standard finite difference method on a Cartesian grid. Although this was a simple method, it was not successful for several reasons. Firstly, the mismatch between the square grids and the boundaries of the objects we used gave rise to inaccuracies, and resulted in non-smooth contact lines. Using a circular grid would resolve this problem but then cause problems at the axis of symmetry. Secondly, the meniscus slopes are largest at the boundaries of the solid objects and then decay to zero at the edges of the domain. As a result, it is desirable to have a dense grid near the object boundaries. However, with the standard finite difference method, it is not easy to have such a variable grid spacing.

These difficulties led us to consider the *hp*-meshless cloud method, which is a meshfree finite difference method developed by [Liszka et al. \(1996\)](#). This method does not require a grid and only uses a collection of nodes “sprinkled” in the domain and on the boundary. As a result, it eliminates both of the drawbacks of standard meshed methods mentioned above. The nodes can be positioned on a boundary with any shape. This was a very significant advantage especially in the solution of floating spheres (Chapter 5), where the horizontal projection of the contact line does not match any standard coordinate system. Since a mesh is not required, the density of nodes can easily be varied in the domain.

The *hp*-meshless cloud method also has some additional advantages. In the standard finite difference method, each data point can only satisfy a single equation, and as a result, the grid points on the boundary satisfy only the boundary condition while the points inside the domain only satisfy the differential equation being solved. In contrast in the *hp*-meshless cloud method, one node can satisfy more than one equation, and [Liszka et al. \(1996\)](#) developed a method for making the boundary nodes satisfy both the boundary condition and the governing differential equation. After the nodes have been distributed, if the nodal density in some region was found to be insufficient, more nodes can be automatically added

while solving the equation using the method developed by (Benito et al., 2003). Because of these advantages, we used the  $hp$ -meshless cloud method to solve the Laplace–Young equation.

### 2.3.1 Principles of the $hp$ -Meshless Cloud Method

In the  $hp$ -Meshless Cloud Method, the finite difference method is generalized by relaxing the need for a regular grid. In the standard finite difference method, the derivatives of a function are obtained directly using the locations of the grid points and properties of the grid. The differential equation to be solved is then numerically expressed using these derivatives. In the  $hp$ -Meshless Cloud Method, a different approach is used to obtain the derivatives. This method, in general, employs an irregularly positioned set of nodes, and the derivatives are determined using a Taylor series approximation. If the value of a function and its derivatives at a particular point in space are known, the Taylor series can give an approximation for the function on a region close to the original point.  $hp$ -Meshless Cloud Method is a way of reversing this procedure: the value of the function and its derivatives at a given point is obtained using the values of the function on a set of points around it and their locations, employing the Taylor series.

A detailed description of this method is given by Liszka et al. (1996); here we give a simplified summary. Assume that the solution we are seeking is given by the (unknown) function  $g(\mathbf{X})$ , where  $\mathbf{X}$  is a location in the domain or on the boundary. We also assume that this solution can be approximated near a given point  $\mathbf{X}_0$  by the function  $f(\mathbf{X})$ , so that  $f(\mathbf{X}_q) \approx g(\mathbf{X}_q)$  where  $\mathbf{X}_q$  is a data point close to  $\mathbf{X}_0$ . We then look for an approximation of  $f$  based on the locations of  $\mathbf{X}_q$  relative to  $\mathbf{X}_0$  so that

$$f(\mathbf{X}_q) = \sum_{i=0}^{n_p} [a_i * p_i(\mathbf{X}_q - \mathbf{X}_0)], \quad q = 1 \cdots m \quad (2.19)$$

In this method, Eq. (2.19) is a set of linear equations that express the Taylor expansion of the function  $f$  about the point  $\mathbf{X}_0$ . Then in one dimension the set

## 2. Fundamentals of interface shapes

---

$\{p_i(x) \mid i \in \mathbb{N}\} = P$ , where  $x = (\mathbf{X} - \mathbf{X}_0)$  is given by

$$P = \{1, x, x^2/2, x^3/6, \dots\}. \quad (2.20)$$

In two dimensions

$$P = \{1, x, y, x^2/2, y^2/2, xy, x^3/6, \dots\}, \quad (2.21)$$

and the coefficients  $a_i$  are approximations for the function  $f$  and its derivatives at  $\mathbf{X}_0$ .

Using the Taylor series for a two dimensional function, the final set of linear equations resulting from Eq. (2.19) may be written as follows:

$$[A] D\mathbf{f} = \mathbf{F}, \quad (2.22)$$

$$[A] = \begin{bmatrix} 1 & j_1 & k_1 & j_1^2/2 & k_1^2/2 & j_1 k_1 & \dots \\ 1 & j_2 & \dots & \dots & \dots & \dots & \dots \\ \vdots & \vdots & \vdots & \vdots & \vdots & \vdots & \vdots \\ j_m & \dots & \dots & \dots & \dots & \dots & \dots \end{bmatrix}, \quad (2.23)$$

$$D\mathbf{f} = \left( f_0, \frac{\partial f_0}{\partial x}, \frac{\partial f_0}{\partial y}, \frac{\partial^2 f_0}{\partial x^2}, \frac{\partial^2 f_0}{\partial y^2}, \frac{\partial^2 f_0}{\partial x \partial y}, \dots \right)^T, \quad (2.24)$$

$$\mathbf{F} = (f_1, f_2, \dots, f_m)^T, \quad (2.25)$$

where

$$f_i = f(x_i, y_i), \quad (2.26)$$

$$j_i = x_i - x_0, \quad (2.27)$$

$$k_i = x_i - y_0. \quad (2.28)$$

It should be emphasized that  $\mathbf{X}_0$  does not need to be a node (data point), and it can be any point in the domain. Solving Eq. (2.22) gives the value of the function  $f$  and its derivatives as a linear combination of the values of  $f$  at nodal

points around it. For the set of linear equations to be solvable, the number of data points  $m$  should be no less than the number of terms  $n$ , i.e.

$$m \geq n \tag{2.29}$$

in Eq. (2.19). Practically,  $m$  is always kept larger than  $n$ , and as a result, Eq. (2.22) is an overdetermined set of linear equations which is solved using least squares method. For this method of solution, each equation in Eq. (2.22) is weighted using a weight ( $w_i$ ) chosen by the function

$$w_i = W(\sigma_i), \tag{2.30}$$

where

$$\sigma = \sqrt{j_i^2 + k_i^2}, \tag{2.31}$$

and the weight function  $W$  should be non-increasing with  $\sigma$ . The expressions thus obtained for the derivatives by solving Eq. (2.22) can then be used to express the differential equation to be solved, same as in the ordinary finite difference method.

The method illustrated in figure 2.4 is used to select a set of nodes close to the central point  $X_0$  to be used in Eq. (2.22). The domain is divided into a number of equal sections around the central point, and a pre-defined equal number of nearest nodes are selected from each section. The central point can also be a node, but it does not have to be one. The collection of the nodes associated with the central point is called a “star” around the central point. This method ensures that the stars are symmetric and their “centres of gravity” are close to the central points. Usually, the central points coincide with a node. (However, this can be different for nodes on the boundary, as discussed later in this section.) As shown in figure 2.5, stars are created this way around each node, so that stars overlap with each other.

With this numerical method, implementing Dirichlet boundary conditions is straightforward, because this directly gives the value of the solution at a node. However, Neumann boundary conditions require special treatment. This type of boundary condition usually gives the derivative of the solution in the direction normal to the boundary. This information can be used to amend Eq. (2.22) so that

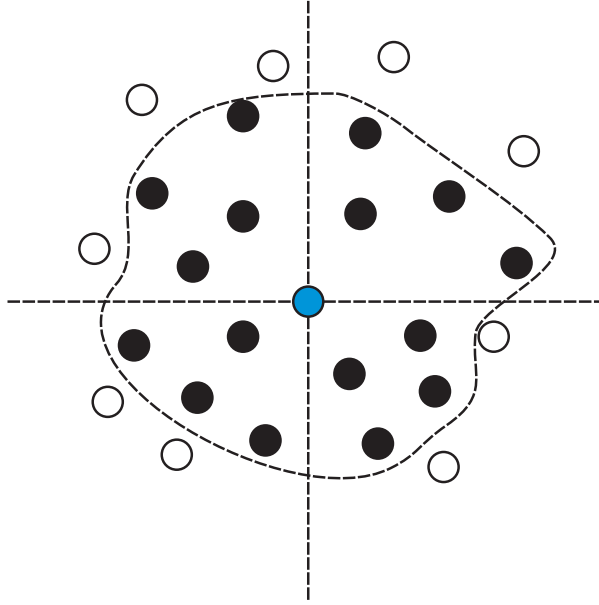


Figure 2.4: A “star” is created by dividing the domain into equal sections around the central point, and selecting an equal number of nodes from each of the sections. The central point is coloured in blue. The selected nodes are represented by filled circles, and the nodes that are not selected are shown by empty circles.

the nodes on the boundary fulfill both the boundary condition and the differential equation that is being solved. If any star contains one or more boundary nodes, in addition to Eq. (2.22), the following equation is also implemented for each of these boundary nodes:

$$\begin{aligned} \frac{\partial f}{\partial n}(x, y) &= \frac{\partial f}{\partial x}(x, y)n_x + \frac{\partial f}{\partial y}(x, y)n_y \\ &= \frac{\partial f_0}{\partial x}n_x + \frac{\partial f_0}{\partial y}n_y + j\frac{\partial^2 f_0}{\partial x^2}n_x + k\frac{\partial^2 f_0}{\partial y^2}n_y + \frac{\partial^2 f_0}{\partial x\partial y}(kn_x + jn_y) + \dots, \end{aligned} \quad (2.32)$$

where  $\hat{\mathbf{n}} = (n_x, n_y)$  is the unit normal to the boundary. Implementing Eq. (2.22) for each of the nodes in the domain and Eq. (2.32) for each of the nodes on the boundary yields

$$[A] D\mathbf{f} = \mathbf{F}, \quad (2.33)$$

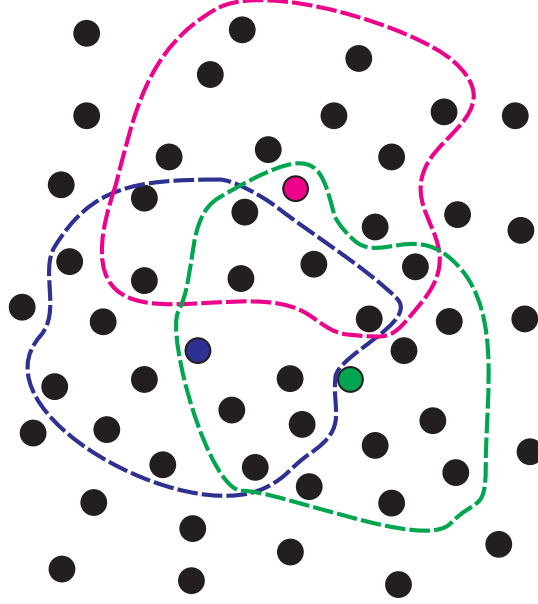


Figure 2.5: Each node is used as a central point at one time, and the “stars” overlap with each other. The coloured curves represent the collection of nodes formed around the central points of the same colour.

$$[A] = \begin{bmatrix} 1 & j_1 & k_1 & j_1^2/2 & k_1^2/2 & j_1 k_1 \\ 1 & j_2 & k_2 & j_2^2/2 & k_2^2/2 & j_2 k_2 \\ \vdots & & & & & \\ 1 & j_m & k_m & j_m^2/2 & k_m^2/2 & j_m k_m \\ 0 & n_{1,x} & n_{1,y} & j_1 n_{1,x} & k_1 n_{1,y} & (k_1 n_{1,x} + j_1 n_{1,y}) \\ 0 & n_{2,x} & n_{2,y} & j_2 n_{2,x} & k_2 n_{2,y} & (k_2 n_{2,x} + j_2 n_{2,y}) \\ \vdots & & & & & \\ 0 & n_{b,x} & n_{b,y} & j_b n_{b,x} & k_b n_{b,y} & (k_b n_{b,x} + j_b n_{b,y}) \end{bmatrix}, \quad (2.34)$$

$$D\mathbf{f} = \left( f_0, \frac{\partial f_0}{\partial x}, \frac{\partial f_0}{\partial y}, \frac{\partial^2 f_0}{\partial x^2}, \frac{\partial^2 f_0}{\partial y^2}, \frac{\partial^2 f_0}{\partial x \partial y} \right)^T, \quad (2.35)$$

$$\mathbf{F} = \left( f_1, f_2, \dots, f_m, \frac{\partial f_1}{\partial n}, \frac{\partial f_2}{\partial n}, \dots, \frac{\partial f_b}{\partial n} \right)^T, \quad (2.36)$$

where  $m$  is the number of nodes in the star and the first  $b$  nodes of these are on

the boundary. To ensure a solution

$$m + b \geq n_p \tag{2.37}$$

needs to be satisfied. If a central point is located on the boundary, the star cannot have nodes located in all directions, unlike the stars with central points inside the domain. This imbalance can result in inaccuracies of the derivatives calculated using Eq. (2.33). Therefore, when a star is needed around a boundary node, the central point is slightly displaced in the direction normal to the boundary by a distance  $\delta n$  into the domain to avoid this problem.

### 2.3.2 Adaptations and implementation of the *hp*-Meshless Cloud Method:

The *hp*-Meshless cloud method was implemented using Matlab to solve the Laplace-Young equation with the relevant boundary conditions. In this section I list the specific adaptations of the already discussed method that were necessary to do this.

In selecting nodes to produce a star, the space around the central point was divided into 4 quadrants, and 12 nodes from each quadrant were selected using the method described in figure 2.4. A 4<sup>th</sup> order Taylor series was used in Eq. (2.33) for the calculation of the derivatives. As recommended by Liszka et al. (1996), the weight function introduced in Eq. (2.30) was selected to be

$$W(\sigma) = \frac{1}{24\sigma^2} \tag{2.38}$$

for equations implementing the Neumann boundary condition, and

$$W(\sigma) = \frac{1}{\sigma^3} \tag{2.39}$$

for other equations. The displacement  $\delta n$  of the central points of stars based on boundary nodes was selected to be one fifth of the minimum distance between two nodes at the boundary.

The *hp*-Meshless cloud method reduces the problem of solving a linear partial

differential equation into a problem of solving a set of linear equations. In the case of a nonlinear partial differential equation, the output would be a set of nonlinear equations. This was avoided using an iterative scheme to handle the nonlinear terms in the Laplace–Young equation, where a set of linear equations was solved at each step. The meniscus height at the  $(N - 1)^{\text{st}}$  iteration was used to give estimates of the nonlinear terms. This allows a linear equation for the meniscus height at a particular point for the  $N^{\text{th}}$  iteration to be written, namely:

$$\zeta^{[N]} = \ell_c^2 \frac{\zeta_{xx}^{[N]}(1 + \zeta_y^2)^{[N-1]} + \zeta_{yy}^{[N]}(1 + \zeta_x^2)^{[N-1]} - 2\zeta_{xy}^{[N]}(\zeta_x\zeta_y)^{[N-1]}}{\left[ (1 + \zeta_x^2 + \zeta_y^2)^{\frac{3}{2}} \right]^{[N-1]}}. \quad (2.40)$$

The boundary conditions are also nonlinear, and handled in a similar iterative scheme. This is discussed in each chapter with respect to each of the boundary conditions specific to the problem then at hand. However, obtaining the non-linear terms of the  $(N - 1)^{\text{st}}$  iteration to set the boundary condition in the  $N^{\text{th}}$  iteration gives rise to an error because the derivatives obtained by solving Eq. (2.33) are not evaluated exactly on the boundary, but at a small distance  $\delta n$  away from it. This error has been corrected in the results shown in Chapters 4–6, by using a third order Taylor series to calculate the values of the derivatives on the boundary based on those a distance  $\delta n$  away. As a result, the results shown in these chapters precisely satisfy the given contact angle boundary condition. However, this correction prevents the iterative scheme from converging at contact angles close to 0. It was therefore not used in Chapter 3 where small contact angles are discussed, and as a result, the values of contact angles in this chapter have a small error, especially when they are close to 0.

In the numerical solution discussed in Chapter 5, there is another complication, because this is a free boundary problem and the location of the boundary is not known *a priori*. I developed a new algorithm (Algorithm 1) to solve this problem, which is described in that chapter.

The iterative scheme to solve the nonlinear Laplace–Young equation is continued until the maximum difference between the interface position in two consecutive iterations is very small (i.e. corresponding for typical physical parameters to displacements on the order of  $10^{-13}$  m). Starting from an initially flat interface

## 2. Fundamentals of interface shapes

---

(corresponding to  $\theta = 90^\circ$ ), the contact angle was gradually changed from  $90^\circ$  to the desired contact angle. The final converged solution of Eq. (2.40) using the respective boundary conditions is the equilibrium shape of the meniscus. If the iterative scheme failed to converge, the collection of nodes was refined by adding more nodes in the areas of maximum error, according to the  $h$ -adaptive method proposed in (Benito et al., 2003). The minimum distance from the centre of a solid object to the edge of the domain was  $7\ell_c$ , and a typical domain contained 6000-9000 nodes.

With these modifications, the  $hp$ -Meshless Cloud Method was used to solve of nonlinear Laplace-Young equation for the variety of problems discussed in the following chapters. Further details of the numerical approach used for each problem are discussed in the corresponding chapters.

## 2.A Derivation of the Young's law

This appendix describes the derivation of the Young's law mentioned in section 2.1.2. When the drop shown in figure 2.2 spreads, the increase of its contact area with the solid is

$$dA_{sl} = 2\pi p dp. \quad (2.41)$$

The change in surface energy due to this is

$$dE_{sl} = (\gamma_{sl} - \gamma_{sf}) dA_{sl}. \quad (2.42)$$

Meanwhile, the area of the liquid–air interface also changes. The surface area of the spherical cap of the drop is

$$A_{lf} = \pi (p^2 + h^2), \quad (2.43)$$

and the change of this area is

$$\begin{aligned} dA_{lf} &= \frac{\partial A_{lf}}{\partial p} dp + \frac{\partial A_{lf}}{\partial h} dh \\ &= 2\pi p dp + 2\pi h dh. \end{aligned} \quad (2.44)$$

$dp$  and  $dh$  are related because the volume of the drop  $V$  is conserved.

$$\begin{aligned} V &= \frac{\pi}{6} (3p^2 h + h^3) \\ dV &= \frac{\partial V}{\partial p} dp + \frac{\partial V}{\partial h} dh \\ &= \pi p h dp + \frac{\pi}{2} (p^2 + h^2) dh. \end{aligned} \quad (2.45)$$

Since the volume is constant,  $dV = 0$ . Therefore,

$$\frac{dh}{dp} = -\frac{2ph}{p^2 + h^2}. \quad (2.46)$$

## 2. Fundamentals of interface shapes

---

From Pythagoras' theorem we have

$$\begin{aligned} p^2 &= R^2 - (R - h)^2 \\ &= 2Rh - h^2. \end{aligned} \quad (2.47)$$

Substitution into Eq. (2.46) gives

$$\frac{dh}{dp} = -\frac{p}{R}. \quad (2.48)$$

This result is substituted to Eq. (2.44) to obtain

$$\begin{aligned} dA_{lv} &= 2\pi p dp - 2\pi h \frac{p}{R} dp \\ &= 2\pi p \left( \frac{R - h}{R} \right) dp \\ &= 2\pi p \cos \theta dp. \end{aligned} \quad (2.49)$$

The total change in the Gibb's free energy can now be calculated as:

$$\begin{aligned} dG &= (\gamma_{sl} - \gamma_{sf}) dA_{sl} + \gamma_{lf} dA_{lf} \\ &= 2\pi p (\gamma_{sl} - \gamma_{sf}) dp + 2\pi p \cos \theta \gamma_{lf} dp \end{aligned} \quad (2.50)$$

At equilibrium we have  $dG = 0$ , which gives  $\gamma_{sl} = \gamma_{sf} - \gamma_{lf} \cos \theta$ , which is known as the Young's law.

## Chapter 3

# The capillary interaction between vertical cylinders at a liquid–fluid interface

In this chapter, I study the immersion forces between a pair of fixed vertical circular cylinders. Calculating the interaction force in this simplified geometry is a first step determining the interactions in more complex systems, but is also of interest in its own right: the capillary force between vertical cylinders has been measured experimentally using a torsion microbalance (Ceco et al., 1996; Velev et al., 1993) and, whilst generally agreeing with existing asymptotic expressions for the force (Kralchevsky et al., 1993), revealed some significant discrepancies. This chapter demonstrates that these discrepancies can largely be attributed to the simplifications made to facilitate analytical progress.

Theoretical expressions have been derived for capillary interactions between fixed vertical cylinders (Kralchevsky et al., 1993), between floating spheres (Chan et al., 1981) and between capillary multipoles (Danov et al., 2005). However, these expressions have limited validity since they are based on the solution of the *linearized* Laplace–Young equation for the shape of the interface between the objects and in some cases (Chan et al., 1981) also use linear superposition of the interfacial shape around a single object. These two approximations can be relaxed by solving the fully nonlinear Laplace–Young equation numerically. Previously,

### 3. The capillary interaction between vertical cylinders at a liquid–fluid interface

---

the finite difference method has been used to provide these numerical solutions (Pozrikidis, 2010). However, it was reported that the numerical solution obtained in this manner was very slow and the most interesting cases of complete wetting and small inter-particle separations (for which the meniscus slope is expected to be largest and hence the validity of the asymptotic results most limited) were not studied. Indeed, for the range of parameters considered in Pozrikidis (2010) no significant deviation between the numerical solution and the asymptotic results was observed. In this chapter, I discuss an implementation of the  $hp$ -meshless cloud method (Liszka et al., 1996), introduced in section 2.3. This method is chosen here for its versatility and allows the iterative solution of the nonlinear Laplace–Young equation even for conditions of complete wetting and for objects at very close range. The main reason was the great flexibility this method allowed in distributing the nodal points.

## 3.1 Theoretical Setting

We consider two vertical cylinders with radii  $R_1$ ,  $R_2$  and contact angles  $\theta_1$ ,  $\theta_2$  that pierce an otherwise planar liquid–fluid interface. This scenario is shown in figure 3.1. The planar interface is disturbed by the presence of the two cylinders because of the requirement that the interface obeys a contact angle condition at the surface of the cylinders. The height of the liquid interface is given by:

$$z = \zeta(x, y) \tag{3.1}$$

with  $z = 0$  representing the undisturbed liquid level.  $(x, y)$  are Cartesian coordinates with the  $x$ -axis lying along the line connecting the centres of the two cylinders. The shape of the meniscus,  $\zeta(x, y)$ , is described by the Laplace–Young equation (Eq. 2.11).

For a meniscus near a vertical cylinder, the appropriate boundary condition is a fixed contact angle  $\theta$ , as shown in figure 3.1. Same as in section 2.1.3, we define  $\mathbf{t}$  as the running tangent to the contact line,  $\mathbf{n}$  as the running outward normal to the cylinder wall and  $\mathbf{b}$  as the binormal to  $\mathbf{t}$  and  $\mathbf{n}$ . Then Eq. (2.17) yields the boundary condition  $\hat{\mathbf{b}} \cdot \hat{\boldsymbol{\gamma}} = \cos \theta_i$  on the surface of cylinder  $i$ , with  $\theta_i$

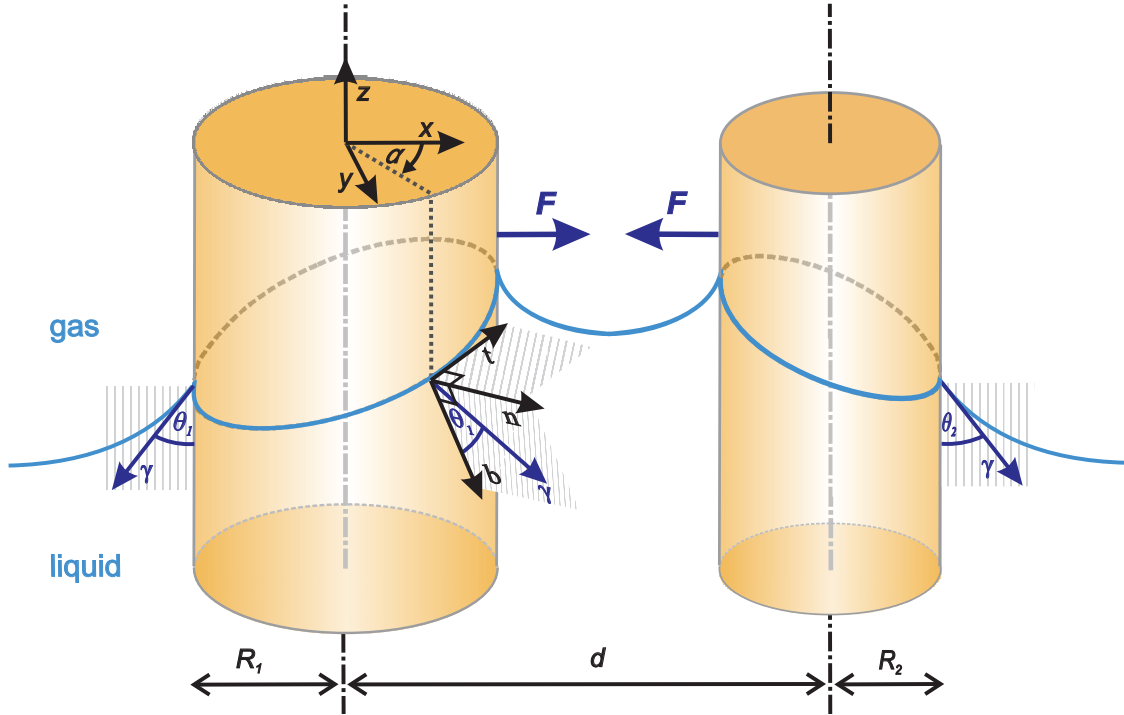


Figure 3.1: A pair of vertical cylinders at a liquid-fluid interface interact due to capillary forces, when one of the fluid phases preferentially wets the solid. Boundary conditions around the two cylinders are shown, and notation is discussed in the text.

defined on the plane containing  $\mathbf{n}$  and  $\mathbf{b}$

The solution of the Laplace–Young equation (2.11) subject to the boundary condition (2.17) on the surface of each cylinder, and the requirement that  $\zeta(x, y) \rightarrow 0$  as  $x, y \rightarrow \pm\infty$ , is sufficient to determine the meniscus profile  $\zeta(x, y)$  for a particular cylinder separation  $d$  and given cylinder radii  $R_{1,2}$  and contact angles  $\theta_{1,2}$ .

The quantity of most interest in this chapter is the lateral interaction force  $F$  between the cylinders i.e. the force that must be applied to each cylinder to maintain a particular separation  $d$ . In general, we expect that the two cylinders will be attracted to one another (so that  $F > 0$ ) but we shall see that there are circumstances under which a repulsive force exists at large separations. Once the shape of the meniscus is known, the component of the force of attraction due to

### 3. The capillary interaction between vertical cylinders at a liquid–fluid interface

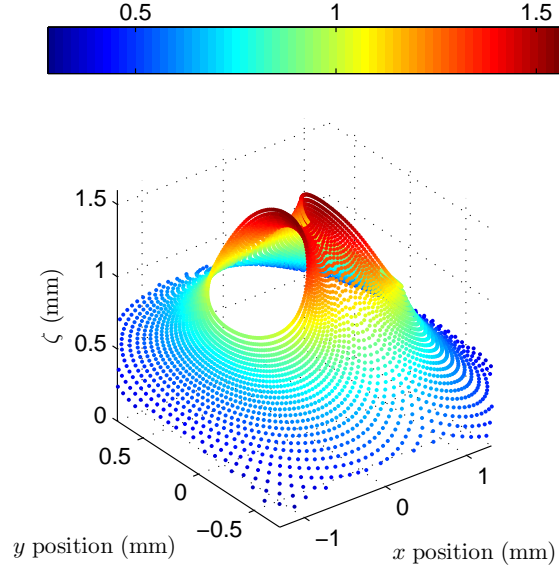


Figure 3.2: Numerical solution for the shape of the 3-dimensional meniscus near two cylinders with  $R_1 = R_2 = 365 \mu\text{m}$ ,  $d = 1150 \mu\text{m}$  and complete wetting ( $\theta = 0^\circ$ ) in a solution matching the properties of experiments in [Ceco et al. \(1996\)](#): SDS solution with  $\gamma = 36.8 \text{ mN/m}$  and  $\Delta\rho = 1000 \text{ kg/m}^3$ , so that  $\ell_c = 1.9 \text{ mm}$ .

surface tension can be calculated by integrating the force due to surface tension around the contact line, as suggested in [Kralchevsky et al. \(1993\)](#). The surface tension force acting on a cylinder is given by:

$$\mathbf{F}_\gamma = \oint \boldsymbol{\gamma} \, ds. \quad (3.2)$$

Here  $\boldsymbol{\gamma}$  is the surface tension force acting along an infinitesimal arclength  $ds$  along the contact line, and  $ds$  is given by:

$$ds = \chi \, d\alpha \quad (3.3)$$

where  $\chi$  is defined by

$$\chi = \sqrt{R_k^2 + \left(\frac{\partial\zeta}{\partial\alpha}\right)^2}, \quad k = 1, 2, \quad (3.4)$$

and  $\alpha$  is the angle between the  $x$ -axis and the line joining the centre of the

cylinder to a point on the contact line (see figure 3.1).

The vector  $\boldsymbol{\gamma}$  can be decomposed as:

$$\boldsymbol{\gamma}^{(i)} = \gamma(\hat{\mathbf{b}} \cos \theta_i + \hat{\mathbf{n}} \sin \theta_i), i = 1, 2. \quad (3.5)$$

If  $\mathbf{e}_x$ ,  $\mathbf{e}_y$  and  $\mathbf{e}_z$  are unit vectors along the  $x$ ,  $y$  and  $z$  directions, respectively, then:

$$\hat{\mathbf{n}} = \cos \alpha \mathbf{e}_x + \sin \alpha \mathbf{e}_y; \quad (3.6)$$

$$\hat{\mathbf{t}} = \frac{1}{\chi} \left( R_k \sin \alpha \mathbf{e}_x - R_k \cos \alpha \mathbf{e}_y - \frac{\partial \zeta}{\partial \alpha} \mathbf{e}_z \right); \quad (3.7)$$

$$\begin{aligned} \hat{\mathbf{b}} &= \hat{\mathbf{n}} \times \hat{\mathbf{t}} \\ &= \frac{1}{\chi} \left( -\frac{\partial \zeta}{\partial \alpha} \sin \alpha \mathbf{e}_x + \frac{\partial \zeta}{\partial \alpha} \cos \alpha \mathbf{e}_y - R_k \mathbf{e}_z \right). \end{aligned} \quad (3.8)$$

Substituting into Eq. (3.5), the  $x$  component of  $\boldsymbol{\gamma}$  becomes:

$$\gamma_x^{(i)} = \gamma \left( -\frac{\partial \zeta}{\partial \alpha} \frac{1}{\chi} \sin \alpha \cos \theta_i + \cos \alpha \sin \theta_i \right). \quad (3.9)$$

Combination of Eq. (3.9) with Eq. (3.2) and Eq. (3.3) gives:

$$F_{\gamma,x}^{(i)} = \gamma \int_0^{2\pi} \left( -\frac{\partial \zeta}{\partial \alpha} \sin \alpha \cos \theta_i + \chi \cos \alpha \sin \theta_i \right) d\alpha. \quad (3.10)$$

In addition to the force from surface tension, a force also acts on each cylinder due to the variations in hydrostatic pressure around the cylinder. This force arises from the differences in liquid level around the cylinder. The  $x$ -component of this force is given by:

$$F_{p,x} = \Delta \rho g R_k \int_0^{2\pi} \frac{1}{2} \zeta^2 \cos \alpha d\alpha. \quad (3.11)$$

Then the total force of attraction between the two cylinders is:

$$F_x = F_{\gamma,x}^{(1)} + F_{p,x}^{(1)}. \quad (3.12)$$

It should be noted that  $F_{\gamma,x}^{(1)}$  and  $F_{\gamma,x}^{(2)}$  are not necessarily equal. However, the total

### 3. The capillary interaction between vertical cylinders at a liquid–fluid interface

---

force given by Eq. (3.12) is the same for both cylinders according to Newton’s third law.

The above approach is used to calculate the force of interaction from the numerical solution for the meniscus shape. The force can also be calculated using an energy approach, as used in the asymptotic solutions discussed in section 3.2. This approach is discussed in detail in Kralchevsky et al. (1993). If the total energy of the system is  $E$  and the inter-particle centre-to-centre distance is  $d$ , then the inter-particle attractive force is given by:

$$F = \frac{dE}{dd}. \quad (3.13)$$

The interaction energy  $E$  is comprised of three components as shown below:

$$\begin{aligned} E = & \Delta\rho g \int_{S_p} \frac{1}{2} \zeta^2 \, dS \\ & + \sum_{k=1}^2 (\gamma_{sl}^{(k)} - \gamma_{sf}^{(k)}) \int_0^{2\pi} \zeta(\alpha, k) R_k \, d\alpha \\ & + \gamma \int_{S_p} \sqrt{1 + \zeta_x^2 + \zeta_y^2} \, dS. \end{aligned} \quad (3.14)$$

In Eq. (3.14), the first term represents the gravitational potential energy of the fluids, the second term is the interfacial energy between the walls of the cylinders and each of the two fluids, and the third term is the interfacial energy between the two fluids. Here  $S_p$  is the projected area of the fluids to the horizontal plane,  $\gamma_{sl}^{(k)}$  is the surface tension between the cylinder  $k$  surface and the lower liquid,  $\gamma_{sf}^{(k)}$  is the surface tension between the cylinder  $k$  surface and the upper fluid,  $\zeta(\alpha, k)$  is the height of the contact line around cylinder  $k$  where  $\alpha$  is the angle measured around a cylinder.

## 3.2 Existing Asymptotic Results

### 3.2.1 Some simplifications

There are two asymptotic limits in which the interaction force between two cylinders can be solved analytically, as described below. In both of these limits, the problem is simplified by linearisation of the Laplace–Young equation as mentioned in section 2.1.1 so that the interfacial deformation is approximately given by Eq. (2.13). This approximation is valid only when the meniscus slopes are small (Eq. 2.14).

When calculating the energy of interaction in certain asymptotic limits, it is furthermore expedient to neglect the gravitational energy of the liquid in Eq. (3.14) compared to other energies. This approximation is expected to be valid for small cylinders  $R_1, R_2 \ll \ell_c$ . We note that although we neglect the gravitational energy in the asymptotic results that follow, our numerical simulations (discussed below in section 3.3) do not neglect this energy.

However, it is also important to emphasize that the inclusion of the term linear in  $\zeta$  in Eq. (2.13) is important in the asymptotic results that follow since it is this term that ensures that the interface decays to the undisturbed level far from the cylinders — something that the solution to Laplace’s equation  $\nabla^2\zeta = 0$  is unable to do.

### 3.2.2 Long-Range Asymptotic Solution

If the separation of the two cylinders  $d$  is large compared to the capillary length  $\ell_c$ , we may consider the meniscus around a single cylinder and, assuming that the individual menisci may simply be superposed, calculate the surface energy increase that results from their interaction. This is the dominant energy that leads to the force of interaction.

A detailed solution of the meniscus shape around a single cylinder was presented by Lo (1983). Far away from the cylinder (compared to the capillary length  $\ell_c$ ) it is convenient to write the linearized Laplace–Young equation (2.13)

### 3. The capillary interaction between vertical cylinders at a liquid–fluid interface

---

in cylindrical polar coordinates to give the interface shape  $\zeta(r)$  as the solution of:

$$\zeta = \frac{\ell_c^2}{r} \frac{d}{dr} \left( r \frac{d\zeta}{dr} \right), \quad (3.15)$$

where  $r$  is radial distance measured from the centre of the cylinder. The solution of this equation that decays as  $r \rightarrow \infty$  is:

$$\zeta(r) = AK_0(r/\ell_c), \quad (3.16)$$

where  $K_0$  is the modified Bessel function of the second kind of zeroth order (Abramowitz and Stegun, 1964). In the limit  $R \ll \ell_c$  we may determine the constant of integration  $A$  as follows. The weight of liquid lifted up within the meniscus is

$$W = 2\pi\Delta\rho g \int_R^\infty r\zeta \, dr = 2\pi\gamma A \frac{R}{\ell_c} K_1(R/\ell_c) \sim -2\pi\gamma A \quad (R \ll \ell_c). \quad (3.17)$$

Using the generalized Archimedes' principle (Keller, 1998) this weight must be supported by the force of surface tension acting around the contact line, which in this case is  $2\pi R \times \gamma \cos\theta$ . Hence we find that  $A = R \cos\theta$ . We note that this result may also be obtained by careful matching of the profile from Eq. (3.16) with the meniscus shape near to the cylinder for which the slope cannot necessarily be assumed to be small (Lo, 1983).

Assuming that the two cylinders are sufficiently far apart from one another (i.e. that their separation  $d \gg \ell_c$ ) then we neglect the first and last terms of Eq. (3.14), and expect that the energy of interaction will simply be the increase in surface energy caused by the change in the height of the meniscus on cylinder 2 due to the meniscus of cylinder 1 (and vice versa). This energy is larger than the increase in gravitational potential energy of the meniscus due to the same effect and the change in energy of the liquid–fluid interface, provided that  $R_{1,2} \ll \ell_c$ . Since this energy of interaction  $\Delta E$  is caused by solid–fluid interface being replaced by solid–liquid interface we expect that the difference in the surface energies of these interfaces on cylinder 2,  $\gamma_{sl}^{(2)} - \gamma_{sf}^{(2)}$ , will be important and so we

have:

$$\Delta E = 2\pi R_2[\gamma_{sl}^{(2)} - \gamma_{sf}^{(2)}]\zeta_1(d).$$

Using Young's law (Eq. 2.15),  $\gamma_{sl}^{(2)} - \gamma_{sf}^{(2)} = -\gamma \cos \theta_2$  and Eq. (3.16) for the meniscus profile  $\zeta_1$ , we find that:

$$\Delta E = -2\pi\gamma R_1 R_2 \cos \theta_1 \cos \theta_2 K_0(d/\ell_c). \quad (3.18)$$

The force of attraction  $F$  is given by  $F = dE/dd$  and so we have that the force of interaction between the two cylinders is:

$$F = \frac{2\pi\gamma R_1 R_2}{\ell_c} \cos \theta_1 \cos \theta_2 K_1(d/\ell_c). \quad (3.19)$$

This result is given by several authors (see for example [Kralchevsky and Nagayama \(2001\)](#)) and can be derived more formally. However, the result Eq. (3.19) remains unchanged.

### 3.2.3 Short-Range Asymptotic Solution

[Kralchevsky et al. \(1993\)](#) developed another analytical solution for a pair of cylinders in the opposite limit in which the inter-particle distance is small compared to the capillary length:  $d \ll \ell_c$ . Instead of linear superposition, the linearized Laplace–Young equation is solved in bipolar cylindrical coordinates for the meniscus around two vertical cylinders. The bipolar cylindrical coordinate system ([Jeffrey, 1995](#)) does not allow the implementation of a boundary condition at infinite distance away from the cylinders. To circumvent this problem, an asymptotic matching was carried out considering  $d/\ell_c$  as a small parameter. We do not repeat this involved calculation here but merely note the final result for the force between two identical cylinders:

$$F = \frac{2\gamma\pi R^2 \cos^2 \theta}{\sqrt{d^2 - 4R^2}}. \quad (3.20)$$

### 3. The capillary interaction between vertical cylinders at a liquid–fluid interface

---

We note that Eq. (3.20) is strictly valid only in the limit  $R \ll d \ll \ell_c$  and so:

$$F \approx \frac{2\gamma\pi R^2 \cos^2 \theta}{d},$$

which is precisely the  $d \ll \ell_c$  limit of the long range force law Eq. (3.19). To make best use of this observation, Kralchevsky and Nagayama (2001) pose the composite expansion:

$$F = \frac{2\pi\gamma R_1 R_2}{\ell_c} \cos \theta_1 \cos \theta_2 K_1(d/\ell_c). \quad (R \ll \ell_c) \quad (3.21)$$

### 3.3 Numerical Solution of the meniscus profiles

Using numerical methods it is possible to solve the full nonlinear Laplace–Young equation Eq. (2.11) without the simplifying assumptions needed to make analytical progress. For this, the *hp*-Meshless Cloud Method (Liszka et al., 1996) described in section 2.3 was used. As mentioned earlier, this method does not require a regular grid, but only a collection of nodes.

These nodes can easily be positioned on the domain boundaries (the cylinders) with nodes within the domain distributed initially on concentric circles, centred at the centre of each cylinder (these circles are clipped along the centre-line between the two circles to avoid them intersecting one another). Furthermore, the radii of these circles are selected in such a way that the node density decreases exponentially with distance from the cylinders. This was an efficient way of dealing with the rapid change in interface shape near the cylinder and slower change further away.

The nonlinear terms in the Laplace–Young equation are handled using the iterative scheme described in Eq. (2.40). It is also necessary to modify the boundary condition Eq. (2.17) so that the relevant nonlinearities are handled by a similar iterative procedure. If  $\hat{\mathbf{s}}$  is the outward unit normal to the liquid surface from the contact point along the plane containing  $\mathbf{b}$  and  $\mathbf{n}$ , it can be deduced from Eq. (2.17) that:

$$\hat{\mathbf{n}} \cdot \hat{\mathbf{s}} = \cos \theta_i. \quad (3.22)$$

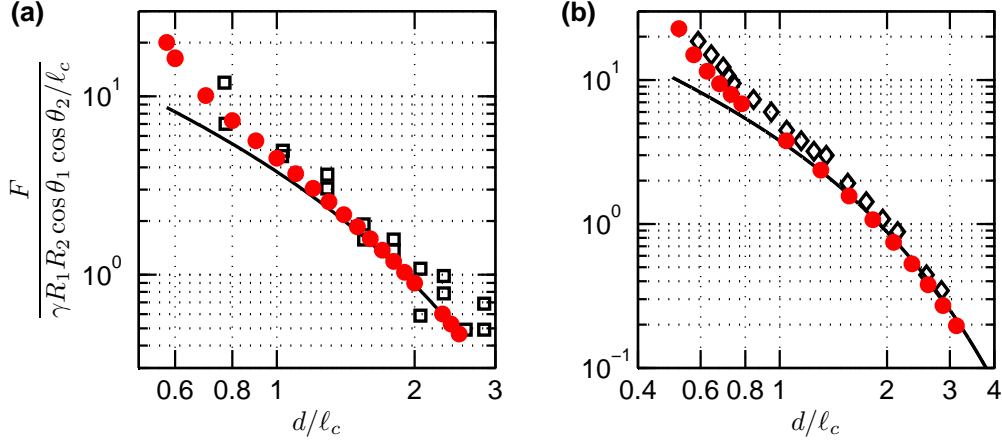


Figure 3.3: (a) Force of attraction between two identical hydrophilic cylinders with  $\theta_1 = \theta_2 = 0^\circ$  and  $R_1 = R_2 = 365 \mu\text{m}$  in a solution of SDS with  $\gamma = 36.8 \text{ mN/m}$ ,  $\Delta\rho = 1000 \text{ kg/m}^3$  so that  $\ell_c = 1.9 \text{ mm}$ . Experimental results from [Ceco et al. \(1996\)](#) ( $\square$ ) are shown along with predictions from the full numerical solution described here ( $\bullet$ ) and the asymptotic result Eq. (3.21) (solid curve). (b) Force of attraction between two similar, but not identical, hydrophilic cylinders with  $\theta_1 = \theta_2 = 0^\circ$ ,  $R_1 = 315 \mu\text{m}$  and  $R_2 = 370 \mu\text{m}$  in the same SDS solution as in (a). Experimental results from [Velev et al. \(1993\)](#) ( $\diamond$ ) are shown along with predictions from the full numerical solution described here ( $\bullet$ ) and the asymptotic result Eq. (3.21) (solid curve).

Now

$$\{\hat{\mathbf{s}}\} = -\{\zeta_x, \zeta_y, -1\} / \sqrt{\zeta_x^2 + \zeta_y^2 + 1}, \quad (3.23)$$

and we may write  $\hat{\mathbf{n}}$

$$\{\hat{\mathbf{n}}\} = \{n_x, n_y, 0\} \quad (3.24)$$

since  $\hat{\mathbf{n}}$  lies in the horizontal plane. Eq. (3.22) can then be expressed as:

$$\zeta_x n_x + \zeta_y n_y = -\cos \theta_i \sqrt{\zeta_x^2 + \zeta_y^2 + 1}, \quad (3.25)$$

which may in turn be converted to an iterative equation

$$[\zeta_x n_x + \zeta_y n_y]^{[N]} = -\cos \theta_i \left[ \sqrt{\zeta_x^2 + \zeta_y^2 + 1} \right]^{[N-1]}. \quad (3.26)$$

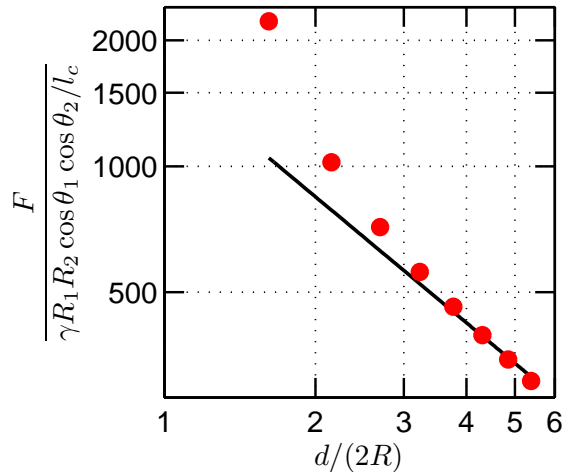


Figure 3.4: The asymptotic solution Eq. (3.21) (solid curve) agrees with numerical simulations for  $R \ll d \ll \ell_c$  (points). Here  $R_1 = R_2 = 5 \mu\text{m}$ ,  $\theta_1 = \theta_2 = 0^\circ$  and the liquid properties are those for an air–water interface (i.e.  $\gamma = 72.4 \text{ mN/m}$  and  $\Delta\rho = 1000 \text{ kg/m}^3$  so that  $\ell_c = 2.7 \text{ mm}$ ). The cylinder diameter here is  $2R \approx 3.7 \times 10^{-3} \ell_c$ .

A typical interface shape, showing the meniscus height calculated at each node point is presented in figure 3.2. With this converged meniscus shape, the force of interaction was determined by integration along the three–phase contact lines as described by Eqs. (3.2 - 3.12).

### 3.4 Force of interaction between vertical cylinders

Figure 3.3(a) and figure 3.3(b) show the attractive capillary force between two perfectly wetting cylinders (i.e.  $\theta = 0^\circ$ ). Over the whole range of available experimental data, the numerical solution agrees very well with experiments (Ceco et al., 1996). In addition, the asymptotic solution (3.21) agrees with both numerics and experiments at large inter-particle separations, as expected. However, when the two cylinders are close to one another, the experimental data deviate from this asymptotic solution. We attribute this discrepancy to the fact that at such small separations the meniscus slopes are large, invalidating the linearization

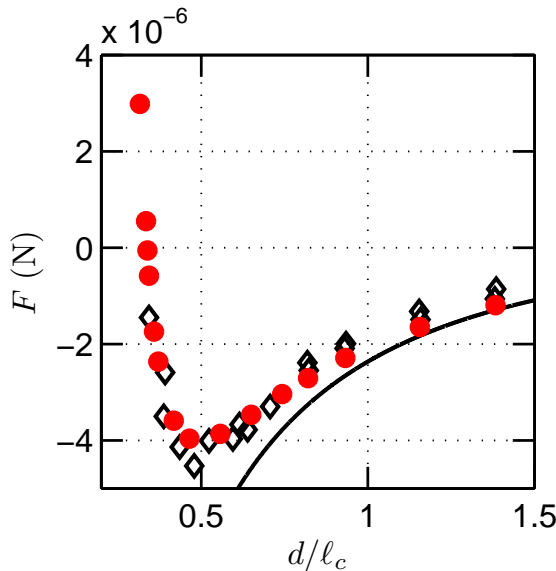


Figure 3.5: Force of interaction between two dissimilar cylinders, matching experimental conditions of (Velev et al., 1993): one cylinder is hydrophilic and the other hydrophobic, held in water with  $\gamma = 72.4 \text{ mN/m}$ ,  $R_1 = 370 \mu\text{m}$ ,  $R_2 = 315 \mu\text{m}$  and  $\theta_1 = 0^\circ$  (the value of  $\theta_2$  is not reported). Numerical results (●) are shown together with the asymptotic prediction Eq. (3.21) (solid curve) with the value  $\theta_2 = 101.5^\circ$ . The numerical simulation is able to reproduce the reduction in repulsive force observed at short ranges in the experimental results (◊) of Velev et al. (1993) and shows that the force becomes attractive at very short range. According to Velev et al. (1993), the long-range asymptotic result agrees best with experiments when  $\theta_2 = 99^\circ$ . However, carrying out the numerical solution for a range of  $\theta$  (with increments of  $0.5^\circ$ ), we found that the best match is for  $\theta_2 = 101.5^\circ$ .

of the Laplace–Young equation made in the derivation of Eq. (3.19). The high meniscus slopes present for these parameter values are clearly illustrated in the numerically generated meniscus profile shown in figure 3.2.

It is well-known that the meniscus around a single very small cylinder ( $R \ll \ell_c$ ) decays over a distance comparable to the cylinder radius  $R$ , rather than the capillary length  $\ell_c$  (Lo, 1983). (The vertical surface tension force exerted by such small cylinders are capable of lifting only small volumes of liquid, so that the perturbations to the interface are smaller.) Because of this we expect that the asymptotic force law Eq. (3.21) should be valid for cylinder separations  $d$  satisfying  $R \ll d$ . To confirm this expectation, figure 3.4 shows the results of

### 3. The capillary interaction between vertical cylinders at a liquid–fluid interface

---

numerical solutions in this regime. We observe that as  $d \rightarrow 2R$  the asymptotic result Eq. (3.21) breaks down because of the large meniscus slopes (as previously) but that for  $d \gg R$  the asymptotic expression is perfectly adequate.

As a more compelling demonstration of the predictive power of our numerical method in comparison to the asymptotic result Eq. (3.21), figure 3.5 shows the interaction force between a hydrophilic and a hydrophobic cylinder. In this situation, the asymptotic result is able to predict the long range repulsive force that is observed experimentally ( $F < 0$ ). However, it is completely unable to reproduce the fact that this repulsion changes sign and becomes a short range attraction when the cylinder separation becomes on the order of their radii.

For the interaction between two vertical plates, a physical explanation of such a transition to attraction was given by [Poynting and Thomson \(1947\)](#) and is repeated, along with illustrative calculations, in [Vella and Mahadevan \(2005\)](#). In summary, the meniscus between the two hydrophilic and hydrophobic plates has to pass through the  $\zeta = 0$  level, and as a result, its curvature significantly increases as the distance between the plates approaches zero. According to the Laplace–Young equation, this causes the liquid column between the plates to rise upwards, producing a negative hydrostatic pressure in this region, resulting in an attractive force between the plates. However, we note that this explanation, which is solely based on hydrostatic pressure, has limited applicability to the interaction between cylinders because the changes in the contact line shape at close range can result in more significant alterations to the surface tension force acting between the cylinders.

The effect of the contact angle on the difference between the numerical results and the asymptotic result Eq. (3.21) is considered in figure 3.6. The results show that the deviation is highest at the steepest meniscus,  $\theta = 0^\circ$ . This is expected because the steeper the meniscus, the larger the error introduced by linearizing the Laplace–Young equation. However, it can also be observed that even at a contact angle of  $85^\circ$ , which leads to a very small meniscus slope angle at the edge of the cylinders, there is a significant deviation from the asymptotic prediction when the two cylinders are close to one another. Comparison of results for cylinders of different radii (figure 3.6a versus figure 3.6b) suggests that there is a larger discrepancy between the asymptotic and numerical results as  $R$  increases. This

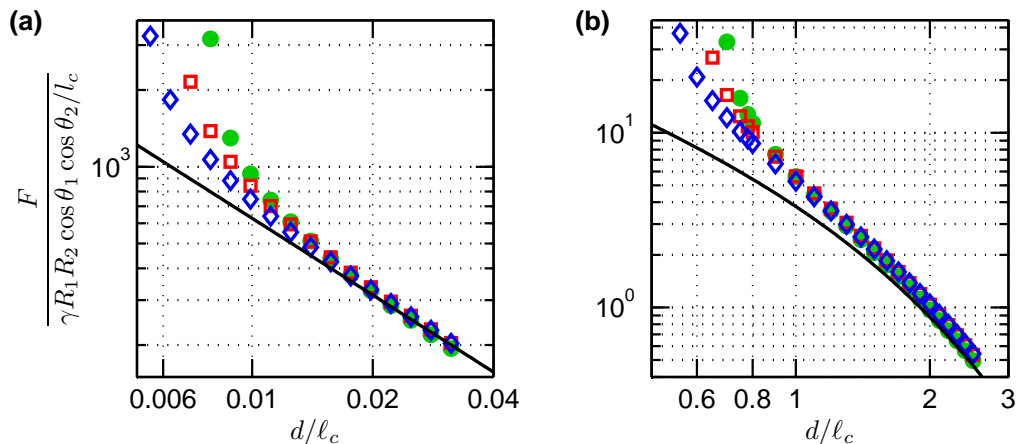


Figure 3.6: The deviation of the numerical results from the asymptotic prediction Eq. (3.21) depends on the contact angle and cylinder radius. Figure shows the numerically determined force of attraction between two identical cylinders as the radius and contact angle change. In (a)  $R = 0.0026 \ell_c$ , while in (b)  $R = 0.26 \ell_c$ . In both (a) and (b), points represent numerical results with contact angle  $\theta = 0^\circ$  ( $\bullet$ ),  $\theta = 45^\circ$  ( $\square$ ), and  $\theta = 85^\circ$  ( $\diamond$ ) while the solid curves show the asymptotic result Eq. (3.21).

is because the asymptotic prediction for the meniscus height Eq. (3.21) is derived under the assumption that  $R \ll \ell_c$ , and breaks down as  $R$  approaches  $\ell_c$ .

Finally, we discuss the validity of approximating the true force law by a power law. Such approximations are of considerable use in more complex scenarios, most notably when attempting to understand the dynamics of aggregation (Chan et al., 1981; Loudet et al., 2005; Vella and Mahadevan, 2005). Based on the composite asymptotic expansion Eq. (3.21) it is common to use the well-known result (Abramowitz and Stegun, 1964) that  $K_1(x) \sim x^{-1}$  for  $x \ll 1$  to obtain  $F \sim d^{-1}$  for  $d \ll \ell_c$ . figure 3.7 shows the effective power-law exponent determined from the numerical simulations presented in this chapter. We observe two features of this power-law exponent: firstly, the value of the power-law is *not universal* and depends both on  $d/\ell_c$  and the particle size  $R/\ell_c$ . Secondly, the regime of validity of such power-laws is extremely limited with none of those plotted in figure 3.7 valid over even a decade in  $d/\ell_c$ ! This should serve as a warning when making such simplifications or when trying to infer a simple exponent from experimental

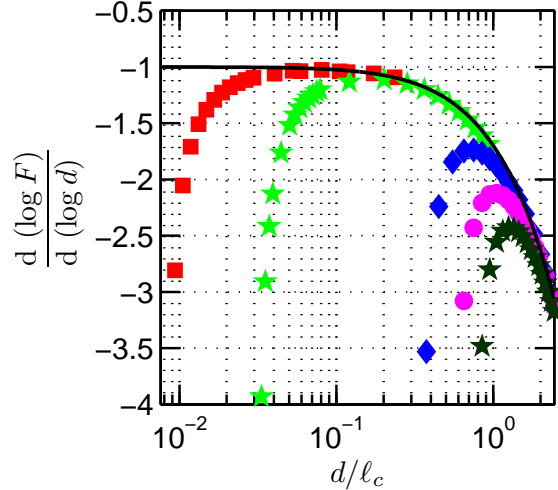


Figure 3.7: The force-law is in general not well approximated by a power law. Here, the local power-law exponent is determined as the logarithmic derivative of the numerically-determined force with respect to distance. We consider pairs of identical cylinders with  $\theta = 0^\circ$ , and a variety of radii:  $R = 0.0026\ell_c$  (■),  $R = 0.01\ell_c$  (★),  $R = 0.11\ell_c$  (◆),  $R = 0.16\ell_c$  (●),  $R = 0.26\ell_c$  (★). The result expected on the basis of the asymptotic solution Eq. (3.21) is shown for comparison (solid curve) and demonstrates the oft-assumed exponent of  $-1$  in the limit  $d \ll \ell_c$ .

data.

### 3.5 Concluding remarks on vertical circular cylinders

We have presented numerical solutions of the nonlinear Laplace–Young equation based on the *hp*-Meshless Cloud method. This provides a versatile tool for the simulation of the meniscus shape around pairs of vertical cylinders in regimes where simple asymptotic approximations are not valid. Crucially, the determination of the interface shape via this method allowed us to calculate the force-separation curve for a range of parameter values and to probe the regime of validity of the asymptotic solutions. These asymptotic solutions rely on the linearization of the Laplace–Young equation and hence fail in situations where the meniscus slope cannot be assumed to be small. In particular, this simplification

### 3.5. Concluding remarks on vertical circular cylinders

---

is not valid for contact angles near perfect wetting and/or complete hydrophobicity, and when the two objects are close to each other. In these regions, the full numerical solution is necessary. Our numerical simulations show excellent agreement with experimental results from the literature even in regimes where the asymptotic results are at variance with experiments. Finally, we demonstrated that the true interaction force-law is *not* well approximated by simple power laws and hence that caution should be used when making such approximations.



# Chapter 4

## Elliptical cylinders at a liquid–gas interface

Anisotropic objects at a liquid interface are of great practical importance because their interaction via capillary forces depends on the orientation. The anisotropic interactions can be used to drive the self-assembly of more complex structures than are seen with isotropic particles. Indeed such effects are thought to be behind the complexity in aggregates of mosquito eggs (Loudet and Pouligny, 2011; Saliternik, 1942) and whirligig beetles (Voise et al., 2011). Artificial anisotropic objects have also been shown to produce a rich variety of self-assembled aggregates (Syms et al., 2003). Attraction and assembly among floating ellipsoids (Lewandowski et al., 2008; Loudet and Pouligny, 2009), horizontal cylinders (Lewandowski et al., 2010) and other complex shapes (Lewandowski et al., 2008) have been experimentally studied.

In order to understand the behavior of anisotropic objects, it is mathematically simplest to analyze objects with an elliptical shape. There have been several studies of floating ellipsoidal particles. For example, capillary interaction potentials between a pair of floating ellipsoids have been experimentally measured by Loudet et al. (2005). These potentials were reported to behave according to a power law with the inter-particle distance, with the power law exponent for the tip-to-tip orientation of the two ellipsoids having a more negative value than that of the side-to-side orientation. Lehle et al. (2008b) addressed the same problem,

#### 4. Elliptical cylinders at a liquid–gas interface

---

where a perturbation solution was given assuming small meniscus slopes and negligible particle weight. They reported that at long range, the force of attraction between two ellipsoids is not orientation–dependent. In contrast at short–range, the force in the tip–to–tip configuration was predicted to be larger than that for the side–to–side configuration. However, according to [Lehle et al. \(2008b\)](#), the forces of attraction at close range are not described by power laws, and the power-law like behavior observed by [Loudet et al. \(2005\)](#) is due to the narrow range of inter-particle distances used experimentally. However, a complete solution for the capillary interaction between floating ellipsoids where the nonlinear Laplace–Young equation is solved and the particle weight is taken into consideration, is still lacking. In particular, it is important to note that all previous theoretical works have neglected the hydrostatic pressure term in the Laplace–Young equation.

Vertical elliptical cylinders offer a simplified setting to understand the behavior of floating anisotropic particles at a liquid–fluid interface. Because of their constant cross sections, the horizontal projection of the three-phase contact line is known *a priori*, simplifying the imposition of the contact angle boundary condition. This enables the solution of the nonlinear Laplace–Young equation using a numerical method. Additionally, vertical elliptical cylinders have their own practical importance. A liquid interface pinned around such a cylinder can be utilized to direct the self assembly of small floating particles. It has been shown recently that horizontally floating small cylinders attract preferentially towards the pointed end of the elliptical cylinder in such a system ([Cavallaro Jr et al., 2011](#)). The floating cylinders create quadrupolar deformations in the liquid interface and the attraction is governed by the liquid–fluid interfacial energy. The shape of the meniscus around the elliptical cylinder needs to be understood for a detailed analysis of this system. [Cavallaro Jr et al. \(2011\)](#) had the contact line of the vertical elliptical cylinder pinned on a horizontal plane, which simplified the problem. They approximated the meniscus near the cylinder as one resulting from a capillary monopole in elliptic cylindrical coordinates. It is conceptually interesting to extend such a system to a vertical elliptical cylinder where the contact line is not pinned but instead has a fixed contact angle (i.e. involving Neumann boundary conditions) and also to the case of multiple elliptical cylinders. This needs an accurate solution for the meniscus shape around an elliptical

cylinder for the case in which the position of the contact line is not known *a priori*.

An asymptotic solution for the meniscus around an isolated elliptical cylinder with a fixed contact angle has been proposed by [Hill and Pozrikidis \(2011\)](#). However, this was achieved by considering the ellipse as a small perturbation to a circle, and therefore, the solution is limited to elliptical cylinders with aspect ratios close to unity. An accompanying numerical solution was also presented for the same system where a finite difference method was employed to solve the nonlinear Laplace–Young equation using orthogonal curvilinear coordinates generated by conformal mapping. The contact line was mentioned to be descending at the tips of the elliptical cylinder and rising at the sides. No detailed figures showing the contact line of the meniscus shapes were presented there, however. Using a similar numerical method, the meniscus shape around an isolated elliptical cylinder with a pinned horizontal contact line has been calculated by [Pozrikidis \(2010\)](#).

In this chapter, I first present a new asymptotic solution for the meniscus shape around an elliptical cylinder with a fixed contact angle, in the limit of small meniscus slopes. This solution is applicable even for cylinders with large aspect ratio because elliptic cylindrical coordinates are used here, unlike previously published solutions. I then present a simpler approximation for the meniscus shape far away from the cylinder. This chapter also includes numerical solutions for the interface shape around one or two elliptical cylinders; these results were obtained by solving the nonlinear Laplace–Young equation subject to the nonlinear boundary conditions. I finally calculate the force of attraction between two elliptical cylinders in the vicinity of one another using both the numerical and asymptotic methods. For this, two specific relative orientations of the cylinders are considered: side-to-side and tip-to-tip. I also note that the cylinders do not undergo any rotational movement in these two configurations because of the symmetry conditions.

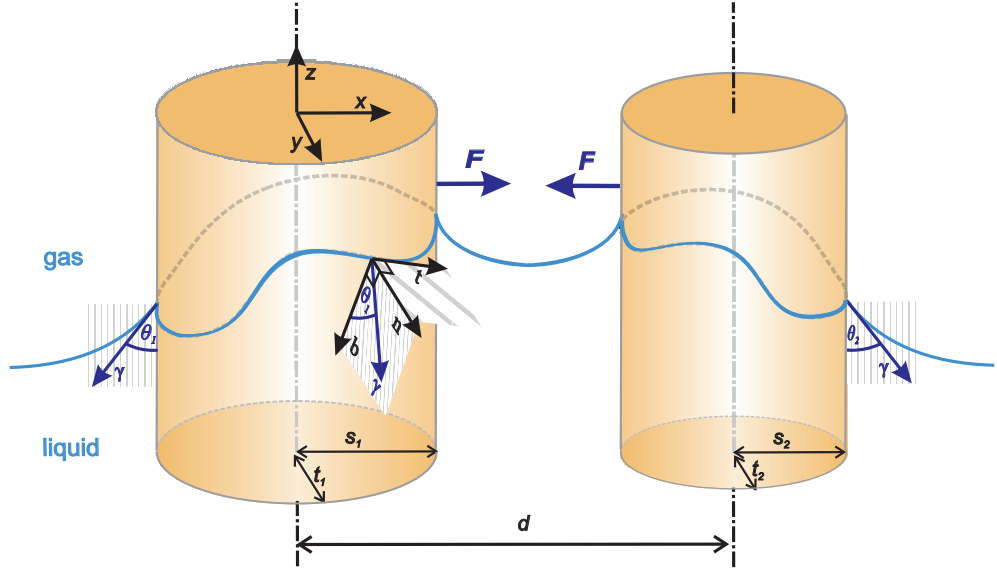


Figure 4.1: Diagram shows the physical system considered in this chapter: Two cylinders of elliptical section, maintained vertical at a liquid–gas interface and held a distance  $d$  apart. The boundary conditions at the walls of the cylinders are given by the contact angles  $\theta_1$  and  $\theta_2$ . The tangent, normal and binormal vectors at the contact line are shown in the diagram.

## 4.1 Theoretical setting

We first consider a single vertical cylinder with elliptical cross section piercing a liquid–gas interface. As before, the position of the liquid interface is given by

$$z = \zeta(x, y), \quad (4.1)$$

where  $x$  and  $y$  are distances measured along the horizontal plane. Far away from the cylinder, the interface is undisturbed by the presence of the cylinder so that  $\zeta \rightarrow 0$ . The interface height must satisfy the Laplace–Young equation, which was described in Eq. (2.11).

The liquid interface meets the wall of cylinder at a fixed contact angle  $\theta$  (see figure 4.1). In order to use this contact angle as a boundary condition for solving the Laplace–Young equation, it is convenient to introduce the elliptic cylindrical coordinate system  $(u, v, \sigma)$  as shown in figure 4.2. (More details about

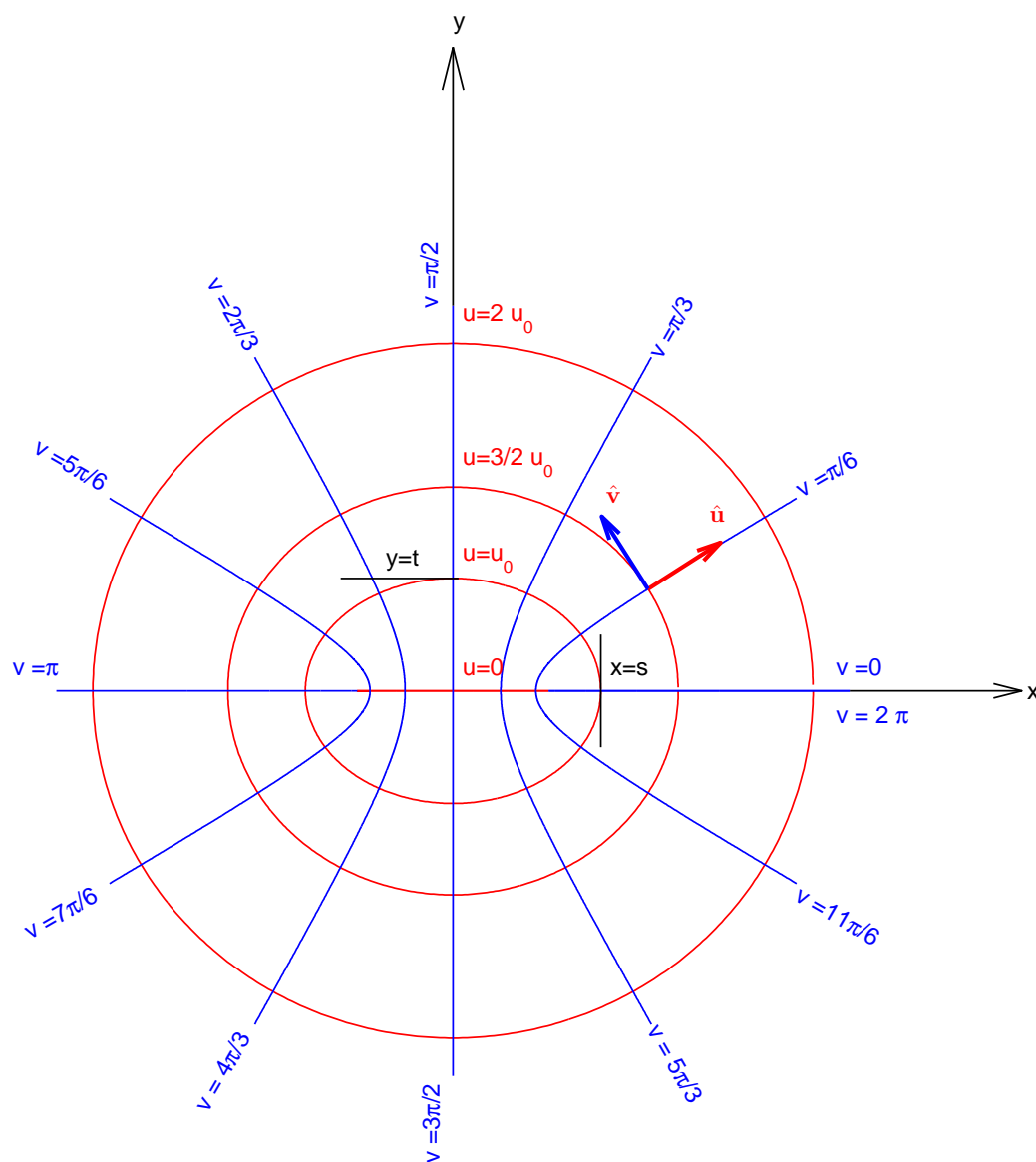


Figure 4.2: Diagram illustrating the elliptic cylindrical coordinate system  $(u, v)$  used in this chapter along with Cartesian coordinates  $(x, y)$ . The elliptic cylindrical coordinate system is adjusted in such a way that  $u = u_0$  denotes the horizontal projection of the boundary of the elliptical cylinder.

#### 4. Elliptical cylinders at a liquid–gas interface

---

this coordinate system may be found in Jeffrey (1995).) Consider the ellipse produced by taking a horizontal cross section of the elliptical cylinder. If  $s$  is the major axis of this ellipse and  $t$  is the minor axis, then the elliptic cylindrical coordinates are related to the Cartesian coordinates by

$$x = a \cos v \cosh u, \quad (4.2)$$

$$y = a \sin v \sinh u, \quad (4.3)$$

$$z = \sigma, \quad (4.4)$$

where  $a$  given by

$$a = \sqrt{s^2 - t^2}, \quad (4.5)$$

is chosen to ensure that the ellipse of interest may be written in the form  $u = u_0$ , where

$$u_0 = \operatorname{arctanh} \left( \frac{s}{t} \right). \quad (4.6)$$

In Cartesian coordinates, the position vector of a point  $P$  on this boundary is

$$\mathbf{P}_h = a \cos v \cosh u_0 \mathbf{e}_x + a \sin v \sinh u_0 \mathbf{e}_y, \quad (4.7)$$

where  $\mathbf{e}_x$  and  $\mathbf{e}_y$  are unit vectors in  $x$ , and  $y$  directions respectively, and the subscript  $h$  emphasizes that this point has been projected onto the horizontal plane.

The contact angle  $\theta$  is the angle between an outward vector normal to the surface of the cylinder and an outward vector normal to the surface of the liquid surface, both originating from the same point on the contact line. Now we determine these two vectors so that we can implement the contact angle boundary condition.

The horizontal unit tangent vector to the boundary of the cylinder is

$$\begin{aligned} \hat{\mathbf{t}}_h &= -\frac{\partial \mathbf{P}_h}{\partial v} \bigg/ \left| \frac{\partial \mathbf{P}_h}{\partial v} \right| \\ &= \frac{\sqrt{2} \cosh u_0 \sin v}{\sqrt{\cosh 2u_0 - \cos 2v}} \mathbf{e}_x - \frac{\sqrt{2} \sinh u_0 \cos v}{\sqrt{\cosh 2u_0 - \cos 2v}} \mathbf{e}_y. \end{aligned} \quad (4.8)$$

Differentiation of this gives the unit normal vector to the outer wall of the cylinder to be

$$\begin{aligned}\hat{\mathbf{n}} &= \frac{\partial \hat{\mathbf{t}}_h}{\partial v} \bigg/ \left| \frac{\partial \hat{\mathbf{t}}_h}{\partial v} \right| \\ &= \frac{\sqrt{2} \sinh u_0 \cos v}{\sqrt{\cosh 2u_0 - \cos 2v}} \mathbf{e}_x + \frac{\sqrt{2} \cosh u_0 \sin v}{\sqrt{\cosh 2u_0 - \cos 2v}} \mathbf{e}_y.\end{aligned}\tag{4.9}$$

The unit outward vector to the liquid interface  $\hat{\mathbf{s}}$  is given in Eq. (3.23). Since  $\theta$  is the angle between  $\hat{\mathbf{n}}$  and  $\hat{\mathbf{s}}$ , in consistence with Eq. (3.22) we must have  $\hat{\mathbf{n}} \cdot \hat{\mathbf{s}} = \cos \theta$ . Substitution of the expressions for  $\hat{\mathbf{n}}$  and  $\hat{\mathbf{s}}$  (Eqs. 4.9, and 3.23) into Eq. (3.22) gives

$$\frac{\sinh u_0 \cos v \zeta_x + \cosh u_0 \sin v \zeta_y}{\sqrt{\zeta_x^2 + \zeta_y^2 + 1}} = -\cos \theta \sqrt{\frac{\cosh 2u_0 - \cos 2v}{2}}.\tag{4.10}$$

Eq. (4.10) is the boundary condition that is to be imposed at  $u = u_0$  when solving the Laplace–Young equation. Additionally as  $u \rightarrow \infty$ , we also require that  $\zeta \rightarrow 0$ .

## 4.2 Solution for small interface deformations

In this section, I present a new solution for the meniscus around a single elliptical cylinder in the range of small interface deformations, i.e.  $|\nabla \zeta \ll 1|$ . I then use this result to calculate the (orientation–dependent) force of attraction between two such cylinders.

### 4.2.1 The linearized Laplace–Young equation and the boundary condition in elliptic cylindrical coordinates

We are unable to solve the fully nonlinear Laplace–Young equation (Eq. 2.11) analytically, we linearize it by assuming small meniscus slopes, i.e.  $\zeta_x, \zeta_y \ll 1$ .

Applying this assumption, the Laplace–Young equation can be linearized to

$$\begin{aligned}\zeta &\approx \ell_c^2 (\zeta_{xx} + \zeta_{yy}) \\ &= \ell_c^2 \Delta\zeta.\end{aligned}\tag{4.11}$$

Using the expression for the Laplacian operator in elliptic cylindrical coordinates (Jeffrey, 1995), this can be rewritten as:

$$\frac{\ell_c^2}{a^2(\sinh^2 u + \sin^2 v)} \left( \frac{\partial^2 \zeta}{\partial u^2} + \frac{\partial^2 \zeta}{\partial v^2} \right) = \zeta.\tag{4.12}$$

Eq. (4.12) must be solved subject to the linearized version of Eq. (4.10). Using the assumption of small meniscus slopes, Eq. (4.10) becomes

$$\sinh u_0 \cos v \zeta_x + \cosh u_0 \sin v \zeta_y \approx -\cos \theta \sqrt{\frac{\cosh 2u_0 - \cos 2v}{2}}.\tag{4.13}$$

As shown in Appendix 4.A, the analogue of Eq. (4.13) written in elliptic cylindrical coordinates is

$$\zeta_u = -a \cos \theta \sqrt{\frac{\cosh 2u - \cos 2v}{2}},\tag{4.14}$$

at  $u = u_0$ .

### 4.2.2 Solution by separation of variables

The differential equation (Eq. 4.12) can be solved by separation of variables. In this method we seek a solution of the form

$$\zeta = U(u)V(v),\tag{4.15}$$

where  $U(u)$  and  $V(v)$  are only functions of  $u$  and  $v$ , respectively. Substituting this into Eq. (4.12) and rearranging gives

$$\left( \frac{1}{U} \frac{d^2 U}{du^2} - \frac{a^2}{\ell_c^2} \sinh^2 u \right) + \left( \frac{1}{V} \frac{d^2 V}{dv^2} - \frac{a^2}{\ell_c^2} \sin^2 v \right) = 0.\tag{4.16}$$

This equation can be separated into two separate equations:

$$\left( \frac{1}{U} \frac{d^2 U}{du^2} - \frac{a^2}{\ell_c^2} \sinh^2 u \right) = c, \quad (4.17)$$

$$c + \left( \frac{1}{V} \frac{d^2 V}{dv^2} - \frac{a^2}{\ell_c^2} \sin^2 v \right) = 0, \quad (4.18)$$

for some constant  $c$ . Finally, we may write:

$$\frac{d^2 U}{du^2} - \left[ \left( c - \frac{a^2}{2\ell_c^2} \right) + \frac{a^2}{2\ell_c^2} \cosh 2u \right] U = 0; \quad (4.19)$$

$$\frac{d^2 V}{dv^2} + \left[ \left( c - \frac{a^2}{2\ell_c^2} \right) + \frac{a^2}{2\ell_c^2} \cos 2v \right] V = 0. \quad (4.20)$$

For convenience, we define constants  $b$  and  $q$  with

$$b = c - \frac{a^2}{2\ell_c^2}, \quad (4.21)$$

$$q = -\frac{a^2}{4\ell_c^2}, \quad (4.22)$$

so that Eq. (4.19) and Eq. (4.20) become

$$\frac{d^2 U}{du^2} - (b - 2q \cosh 2u) U = 0, \quad (4.23)$$

$$\frac{d^2 V}{dv^2} + (b - 2q \cos 2v) V = 0. \quad (4.24)$$

Written in this form, the second of these two equations is just the Mathieu equation while the first is the modified Mathieu equation (McLachlan, 1964). Their solutions are Mathieu functions and modified Mathieu functions, respectively.

Consider the Mathieu equation Eq. (4.24) of which the solution is a Mathieu function. There are two type of Mathieu functions: “even” and “odd”. For

positive values of  $q$ , even Mathieu functions are denoted by

$$ce_{2n}(v, q) = \sum_{r=0}^{\infty} A_{2r}^{(2n)} \cos 2rv, \quad (4.25)$$

$$ce_{2n+1}(v, q) = \sum_{r=0}^{\infty} A_{2r+1}^{(2n+1)} \cos(2r+1)v, \quad (4.26)$$

and odd Mathieu functions are denoted by

$$se_{2n}(v, q) = \sum_{r=0}^{\infty} M_{2r}^{(2n)} \sin 2rv, \quad (4.27)$$

$$se_{2n+1}(v, q) = \sum_{r=0}^{\infty} M_{2r+1}^{(2n+1)} \sin(2r+1)v. \quad (4.28)$$

In these equations,  $2n$  or  $2n+1$  is the order of the Mathieu function,  $A$  and  $M$  are coefficients that depend on the order of the Mathieu function and the parameter  $q$ . Because of the symmetric geometry of an elliptical cylinder,  $\zeta$  (and therefore  $V$ ) needs to be an even function of  $v$  with period  $\pi$ . Only even Mathieu functions of even orders fulfill this criteria. Therefore  $V = ce_{2n}(v, -q)$ , noting that the value of  $q$  given in Eq. (4.22) is negative. For positive  $q$ , such a Mathieu function has the form given in Eq. (4.25). For negative  $q$ , this changes to (McLachlan, 1964)

$$ce_{2n}(v, -q) = (-1)^n \sum_{r=0}^{\infty} (-1)^r A_{2r}^{(2n)} \cos 2rv, \quad (4.29)$$

and the general shape of such a Mathieu function is shown in figure 4.3 (a). In the definition of the coefficients  $A_{2r}^{(2n)}$ , different authors have used different normalization schemes. We use the following normalization method presented by McLachlan (1964):

$$2 \left[ A_0^{(2n)} \right]^2 + \sum_{r=1}^{\infty} \left[ A_{2r}^{(2n)} \right]^2 = 1. \quad (4.30)$$

These even Mathieu functions satisfy the following orthogonality relations

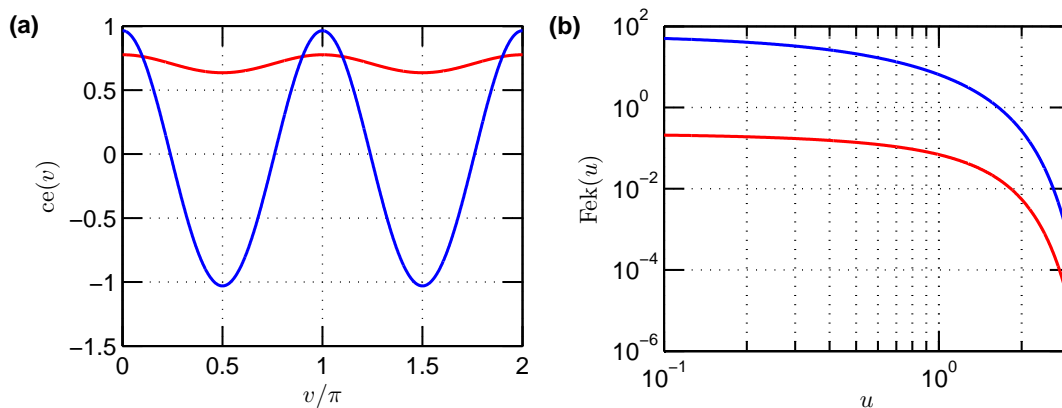


Figure 4.3: The Mathieu functions used in the solution of the meniscus around an elliptical cylinder. (a) shows the even Mathieu function  $ce_m(v, q)$  and (b) shows the modified Mathieu function  $Fek_m(v, q)$ . All the plots are for  $q = -0.2$ . Blue curves (—) denote Mathieu functions of order  $m = 0$ , and red curves (—) denote Mathieu functions of order  $m = 2$ .

(McLachlan, 1964):

$$\int_0^{2\pi} ce_m(v, q) ce_p(v, -q) dv = 0, m \neq p, \quad (4.31)$$

$$\int_0^{2\pi} ce_m^2(v, q) dv = \pi. \quad (4.32)$$

The parameter  $b$  in Eq. (4.24) is constrained by the requirement that  $V$  be periodic. In particular,  $b$  must be the Mathieu characteristic number for the given order and parameter  $q$ .

Now we consider Eq. (4.23). As  $u \rightarrow \infty$ ,  $\zeta$  (and therefore  $U$ ) approaches 0. To satisfy this condition, we must take

$$U = Fek_{2n}(u, -q). \quad (4.33)$$

Fek is the only type of modified Mathieu function (McLachlan, 1964) that reaches zero at large  $U$ . It is given by

$$Fek_{2n}(u, -q) = \frac{p'_{2n}}{\pi A_0^{(2n)}} \sum_{r=0}^{\infty} A_{2r}^{(2n)} I_r(ke^{-u}) K_r(ke^u), \quad (4.34)$$

#### 4. Elliptical cylinders at a liquid–gas interface

---

and examples for functions of this type is plotted in figure 4.3 (b). Here  $k = \sqrt{|q|}$ ,  $I_r$  is the modified Bessel function (Abramowitz and Stegun, 1964) of the first kind and order  $r$ , and,  $K_r$  is the modified Bessel function of second kind and order  $r$ .  $p'_{2n}$  is a constant given by

$$p'_{2n} = \frac{(-1)^n \text{ce}_{2n}(\pi/2, q) \text{ce}_{2n}(0, q)}{A_0^{(2n)}}. \quad (4.35)$$

Substituting the expressions derived for  $U$  and  $V$  into  $\zeta = UV$  and superposing different orders of the Mathieu functions we find that the interface shape may be written

$$\zeta(u, v) = \sum_{n=0}^{\infty} B_{2n} \text{Fek}_{2n}(u, -q) \text{ce}_{2n}(v, -q). \quad (4.36)$$

The coefficients  $B_{2n}$  must be chosen such that the boundary condition (Eq. 4.14) is satisfied. Differentiation of Eq. (4.36) with respect to  $u$  at the boundary of the cylinder  $u = u_0$  gives

$$\zeta_u(u_0, v) = \sum_{n=0}^{\infty} B_{2n} \text{Fek}'_{2n}(u, -q) \text{ce}_{2n}(v, -q). \quad (4.37)$$

By differentiating Eq. (4.34) we obtain

$$\begin{aligned} & \text{Fek}'_{2n}(u, -q) \\ &= \frac{p'_{2n}}{\pi A_0^{2n}} \sum_{r=0}^{\infty} A_{2r}^{(2n)} \left[ -ke^u I_r(ke^{-u}) K_{r-1}(ke^u) - ke^{-u} I_{r-1}(ke^{-u}) K_r(ke^u) \right]. \end{aligned} \quad (4.38)$$

Substituting the expression derived for  $\zeta_u$  in Eq. (4.37) to the boundary condition in Eq. (4.14) gives

$$-a \cos \theta \sqrt{\frac{\cosh 2u - \cos 2v}{2}} = \sum_{n=0}^{\infty} B_{2n} \text{Fek}'_{2n}(u, -q) \text{ce}_{2n}(v, -q). \quad (4.39)$$

$B_{2n}$  can be determined by making use of the orthogonality properties of the function  $\text{ce}$  presented in Eqs. (4.31, 4.32). Multiplying both sides of Eq. (4.39) by  $\text{ce}_{2n}(v, -q)$ , integrating from  $v = 0$  to  $v = 2\pi$ , and applying the orthogonality

relations gives:

$$B_{2n} = -\frac{a \cos \theta C_{2n}}{\sqrt{2} \pi \operatorname{Fek}'_{2n}(u_0, -q)}, \quad (4.40)$$

where

$$C_{2n} = \int_0^{2\pi} \operatorname{ce}_{2n}(v, -q) \sqrt{\cosh 2u - \cos 2v} \, dv. \quad (4.41)$$

The general meniscus profile may then be written

$$\zeta(u, v) = -\frac{a \cos \theta}{\sqrt{2} \pi} \sum_{n=0}^{\infty} \frac{C_{2n} \operatorname{Fek}_{2n}(u, -q) \operatorname{ce}_{2n}(v, -q)}{\operatorname{Fek}'_{2n}(u_0, -q)}. \quad (4.42)$$

In the interest of simplicity, we would like to truncate this series. We find that only the first two terms are required to properly explain the variation of the meniscus height with  $v$ , and these two terms are sufficient to describe the proper meniscus shape with acceptable accuracy (i.e. taking more terms does not lead to any noticeable improvement). We therefore use

$$\zeta(u, v) = -\frac{a \cos \theta}{\sqrt{2} \pi} \sum_{n=0}^1 \frac{C_{2n} \operatorname{Fek}_{2n}(u, -q) \operatorname{ce}_{2n}(v, -q)}{\operatorname{Fek}'_{2n}(u_0, -q)}. \quad (4.43)$$

Figures 4.4(a) and 4.5(a) show the meniscus shape produced by isolated elliptical cylinders of different ellipticity, calculated using the asymptotic solution Eq. (4.43). The contours show that far away from the elliptical cylinder, the meniscus is effectively axisymmetric. Figure 4.5(a) shows that for large aspect ratio there is a very significant deviation from this axisymmetry at close range.

This is further illustrated in Figure 4.6. The blue curves show the contact line height calculated using Eq. (4.43). Here,  $\alpha$  is defined as

$$\alpha = \arctan\left(\frac{y}{x}\right), \quad (4.44)$$

where  $(x, y)$  is a location on the contact line in Cartesian coordinates. Regardless of the aspect ratio of the elliptical cylinder, the contact line descends at the pointed ends and rises at the sides for contact angles below  $\pi/2$ . This effect is also mentioned in Hill and Pozrikidis (2011). For a cylinder with a large aspect ratio, the drop of the contact line height at the tips is very sharp indeed.

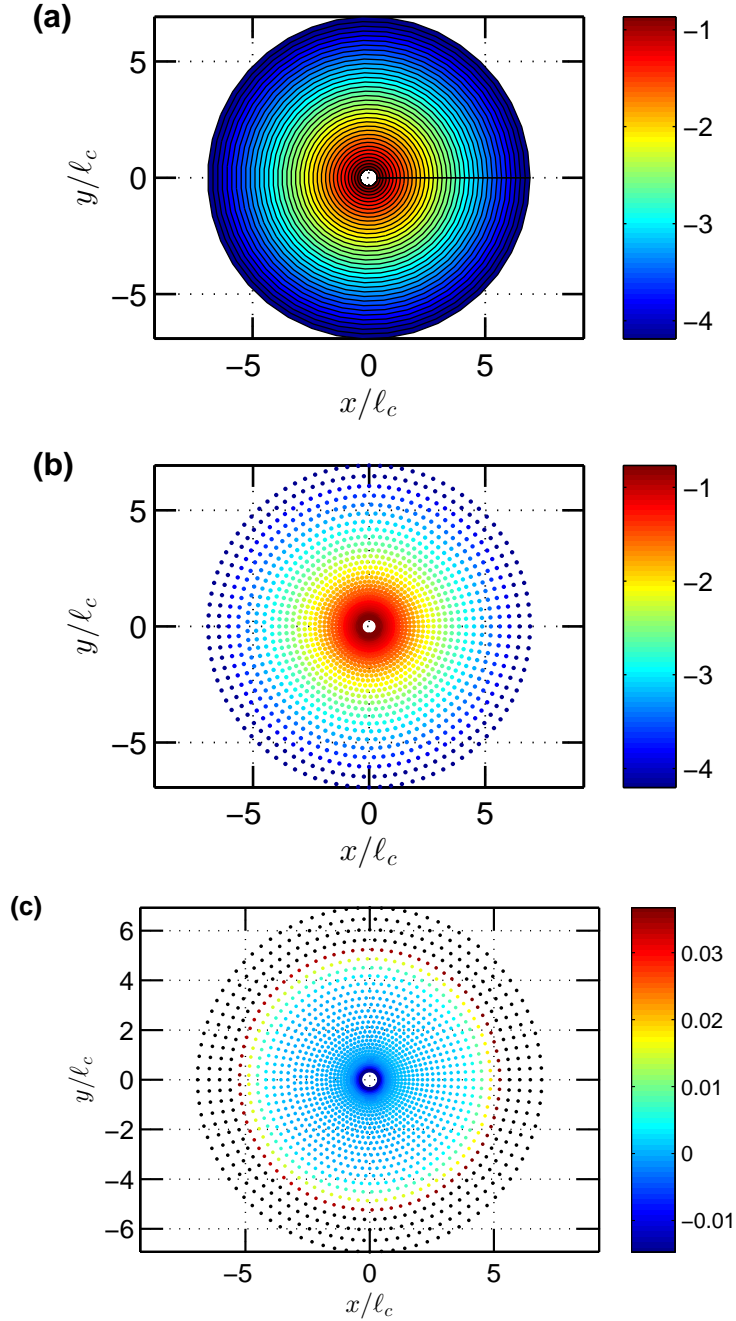


Figure 4.4: Shape of the meniscus created by an elliptical cylinder with *small* aspect ratio, i.e. major axis  $s = 0.372 \ell_c$ , minor axis  $t = 0.364 \ell_c$  and  $s/t = 1.022$ , at a water–air interface with  $\theta = 70^\circ$ ,  $\gamma = 72.4 \text{ mN m}^{-1}$ ,  $\rho_l = 1000 \text{ kg m}^{-3}$ ,  $\rho_v = 0$ ,  $\ell_c = 2.717 \text{ mm}$ . (a) is the asymptotic solution (Eq. 4.43) and (b) is the numerical solution, with the colors representing  $\log(\zeta/\ell_c)$ . (c) shows the relative error between the two solutions (Eq. 4.86). The numerical and asymptotic solutions show good agreement with each other. The high relative error at the edge of the domain is because the interface height is forced to reach 0 here in the numerical solution.

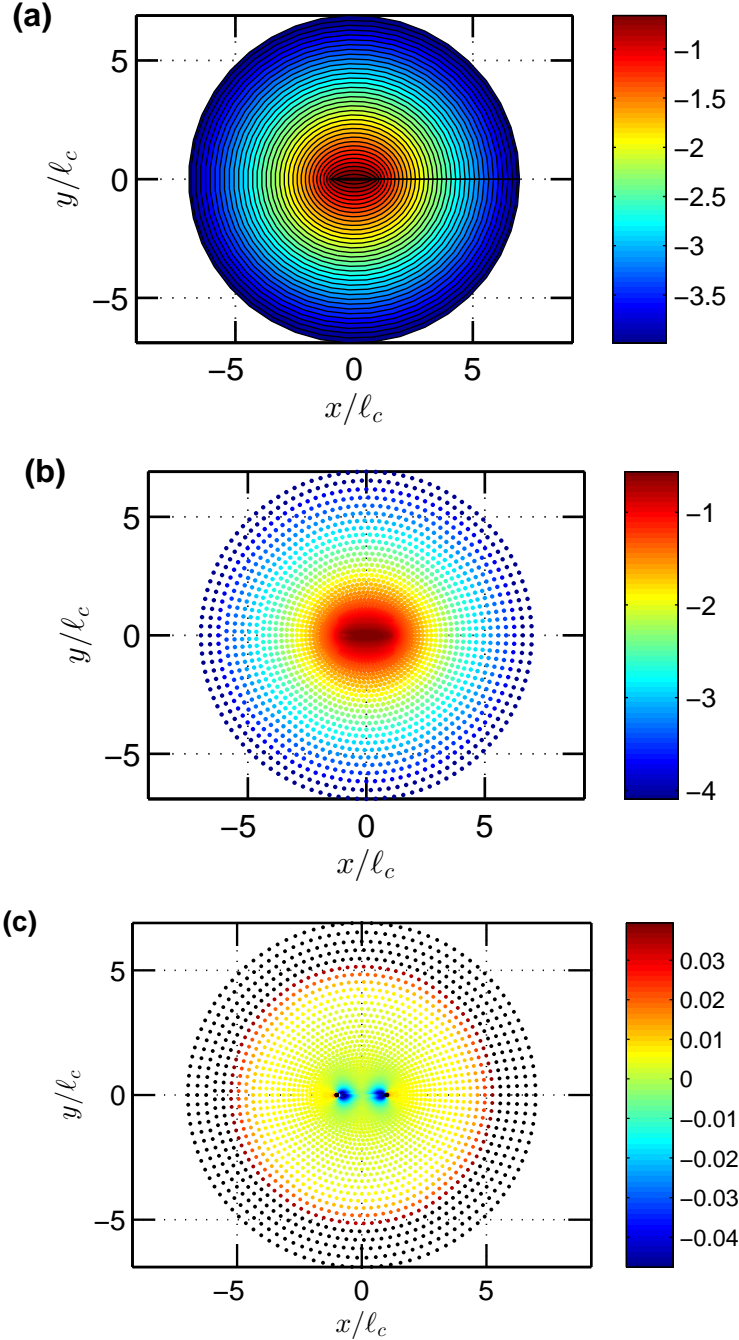


Figure 4.5: Shape of the meniscus created by an elliptical cylinder with *large* aspect ratio, i.e.  $s = \ell_c$ ,  $t = 0.037 \ell_c$  and  $s/t = 27.027$ , at a water-air interface with  $\theta = 70^\circ$ ,  $\gamma = 72.4 \text{ mN m}^{-1}$ ,  $\rho_l = 1000 \text{ kg m}^{-3}$ ,  $\rho_v = 0$ ,  $\ell_c = 2.717 \text{ mm}$ . (a) is the asymptotic solution (Eq. 4.43) and (b) is the numerical solution, with the colors representing  $\log(\zeta/\ell_c)$ . (c) shows the relative error between the two solutions (Eq. 4.86). As in figure 4.4, the numerical and asymptotic solutions show good agreement with each other, except at the edge of the domain where the interface height in the numerical solution is forced to reach 0.

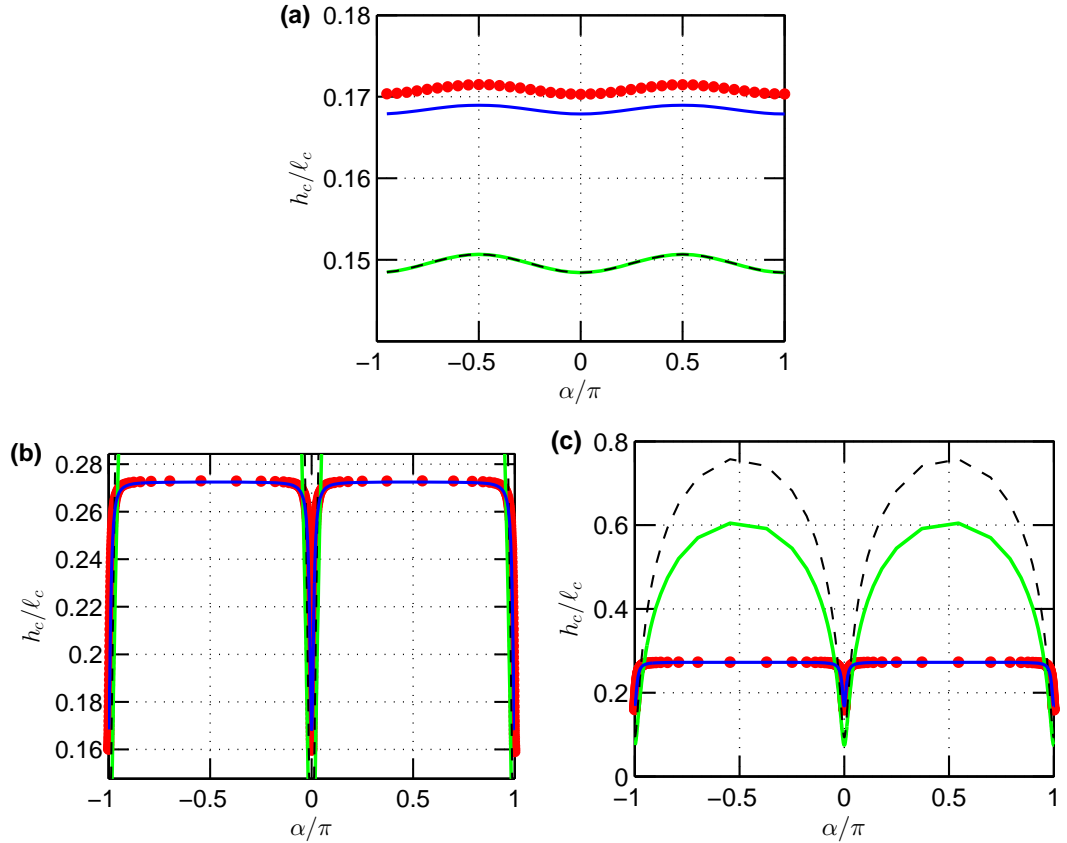


Figure 4.6: Contact line heights of menisci created by an isolated elliptical cylinder at air-water interface. (a): a cylinder with small aspect ratio ( $s = 0.372 \ell_c, t = 0.364 \ell_c, s/t = 1.022$ ); (b) and (c): a cylinder with large aspect ratio ( $s = \ell_c, t = 0.037 \ell_c, s/t = 27.027$ ), where (c) shows the complete data range of (b). The physical properties are  $\theta = 70^\circ$ ,  $\gamma = 72.4 \text{ mN m}^{-1}$ ,  $\rho_l = 1000 \text{ kg m}^{-3}$ ,  $\rho_v = 0$ ,  $\ell_c = 2.717 \text{ mm}$ . (•) denotes the contact line height obtained using the numerical solution and solid blue curve (—) denotes contact line height obtained using the asymptotic solution (Eq. 4.43 with  $u = u_0$ ). The numerical and asymptotic solutions agree very well regardless of the aspect ratio of the elliptical cylinder. Approximations for the contact line height were obtained using Eq. (3.16) which gives the meniscus profile around a circular cylinder. Using this equation, the meniscus height along the elliptical boundary of the cylinder was calculated. solid green curve (—) denotes the contact line height calculated this way using Eq. (3.16) with  $R = (s + t)/2$ , and dashed black curve (--) is the same calculation using Eq. (3.16) with  $R = R_P$ .

### 4.2.3 Asymptotic calculation of the force of attraction

Once the shape of the meniscus created by one cylinder is known, we can determine the effect of the presence of another cylinder at a distance  $d$  (figure 4.1). Assuming the menisci of the two cylinders can be linearly superimposed, the additional area of the second cylinder wetted by the liquid because of the interfacial deformation due to the first cylinder is

$$\Delta A = \int_l \zeta(u_c, v_c) dl, \quad (4.45)$$

where  $(u_c, v_c)$  is a point on the contact line of the second cylinder expressed in terms of elliptic cylindrical coordinates centred on the first cylinder,  $\zeta$  is the height of the meniscus created by the first cylinder, and  $l$  is the horizontal arc length measured along the cylinder wall. We simplify the above expression by assuming  $\zeta(u_c, v_c)$  to be constant around the contact line on the second cylinder. Then,

$$\Delta A \approx P_2 \zeta(u, v) \quad (4.46)$$

where  $(u, v)$  is the location of the centre of the second cylinder and  $P_2 = \int_l dl$  is its perimeter. Now, using Eq. (4.7):

$$\begin{aligned} dl &= \sqrt{\frac{\partial \mathbf{P}}{\partial v} \cdot \frac{\partial \mathbf{P}}{\partial v}} dv \\ &= a\xi dv \end{aligned} \quad (4.47)$$

where

$$\xi = \sqrt{\frac{\cosh 2u_0 - \cos 2v}{2}}. \quad (4.48)$$

We therefore have that the perimeter of the second cylinder may be written

$$P_2 = \int_0^{2\pi} a_2 \xi_2 dv, \quad (4.49)$$

#### 4. Elliptical cylinders at a liquid–gas interface

---

where

$$a_2 = \sqrt{s_2^2 - t_2^2}. \quad (4.50)$$

The change of wetting energy of the cylinder surface is given by

$$\begin{aligned} \Delta E &= \left( \gamma_{sl}^{(2)} - \gamma_{sv}^{(2)} \right) \Delta A \\ &= -\gamma \cos \theta_2 P_2 \zeta(u, v), \end{aligned} \quad (4.51)$$

where  $\gamma_{sl}^{(2)}$  and  $\gamma_{sv}^{(2)}$  are the solid-liquid surface tension and the solid-vapour surface tension for the second cylinder. The force of attraction can be obtained by differentiating the above expression with respect to the distance between the cylinders, we find that

$$F = -\gamma \cos \theta_2 P_2 \frac{\partial \zeta(u, v)}{\partial d}. \quad (4.52)$$

If the location of the centre of the second cylinder is  $(x, y)$  in Cartesian coordinates centred on the first cylinder, then the corresponding values of  $u$  and  $v$  are given by

$$u = \Re \left[ \operatorname{arccosh} \left( \frac{x + iy}{a_1} \right) \right], \quad (4.53)$$

$$v = \Im \left[ \operatorname{arccosh} \left( \frac{x + iy}{a_1} \right) \right]. \quad (4.54)$$

In this analysis, we consider two configurations of interaction, namely, side-to-side interaction and tip-to-tip interaction between the cylinders. Since  $v$  remains constant for these movements we have

$$\frac{\partial \zeta}{\partial d} = \frac{\partial \zeta}{\partial u} \frac{\partial u}{\partial d}. \quad (4.55)$$

For the tip-to-tip interaction using Eq. (4.53) yields

$$u = \operatorname{arccosh} \left( \frac{d}{a_1} \right), \quad (4.56)$$

$$\frac{\partial u}{\partial d} = \frac{1}{\sqrt{d^2 - a_1^2}}. \quad (4.57)$$

Combining this with Eq. (4.55) produces

$$\frac{\partial \zeta}{\partial d} = \left( \frac{1}{\sqrt{d^2 - a_1^2}} \right) \frac{\partial \zeta}{\partial u}, \quad (4.58)$$

and for this configuration we also have

$$v = 0. \quad (4.59)$$

We substitute these results into Eq. (4.52) and use the first term of the infinite series in the expression for  $\zeta$  (Eq. 4.42) which gives the average meniscus height with acceptable accuracy. This yields the force of interaction

$$F_{tip-tip} = \frac{\gamma \cos \theta_1 \cos \theta_2 P_2 C_0 \operatorname{Fek}'_0(u, -q) \operatorname{ce}_0(0, -q)}{\pi \operatorname{Fek}'_0(u_0, -q) \sqrt{2(d^2 - a_1^2)}}, \quad (4.60)$$

where

$$u = \operatorname{arccosh} \left( \frac{d}{a_1} \right), \quad (4.61)$$

$$u_0 = \operatorname{arctanh} \left( \frac{s_1}{t_1} \right), \quad (4.62)$$

and

$$a_1 = \sqrt{s_1^2 - t_1^2}. \quad (4.63)$$

#### 4. Elliptical cylinders at a liquid–gas interface

---

For the case of side–to–side interaction:

$$u = \operatorname{arcsinh} \left( \frac{d}{a_1} \right), \quad (4.64)$$

$$\frac{\partial u}{\partial d} = \frac{1}{\sqrt{d^2 + a_1^2}}, \quad (4.65)$$

and

$$v = \pi/2. \quad (4.66)$$

Using a similar calculation as for the tip–to–tip attraction we obtain

$$F_{side-side} = \frac{\gamma \cos \theta_1 \cos \theta_2 P_2 C_0 \operatorname{Fek}'_0(u, -q) \operatorname{ce}_0(\pi/2, -q)}{\pi \operatorname{Fek}'_0(u_0, -q) \sqrt{2(d^2 + a_1^2)}}, \quad (4.67)$$

where  $u$  is given in Eq. (4.64), and  $u_0$  and  $a_1$  same as in the tip–to–tip calculation (Eq. 4.62 and Eq. 4.63).

The blue and red curves in figure 4.7 show the force of attraction between pairs of identical elliptical cylinders asymptotically calculated using Eq. (4.60) and Eq. (4.67). As the two cylinders move closer, the tip–to–tip force becomes larger compared to the side–to–side force. As they move further apart, the difference between the side–to–side and tip–to–tip forces diminishes. This is similar to the behaviour of forces of attraction in the two configurations predicted in [Lehle et al. \(2008b\)](#) and experimentally observed by [Loudet et al. \(2005\)](#). (Note that the curve showing the tip–to–tip force stops before the curve showing the side–to–side force because in this configuration, the cylinders touch at larger values of  $d$ ).

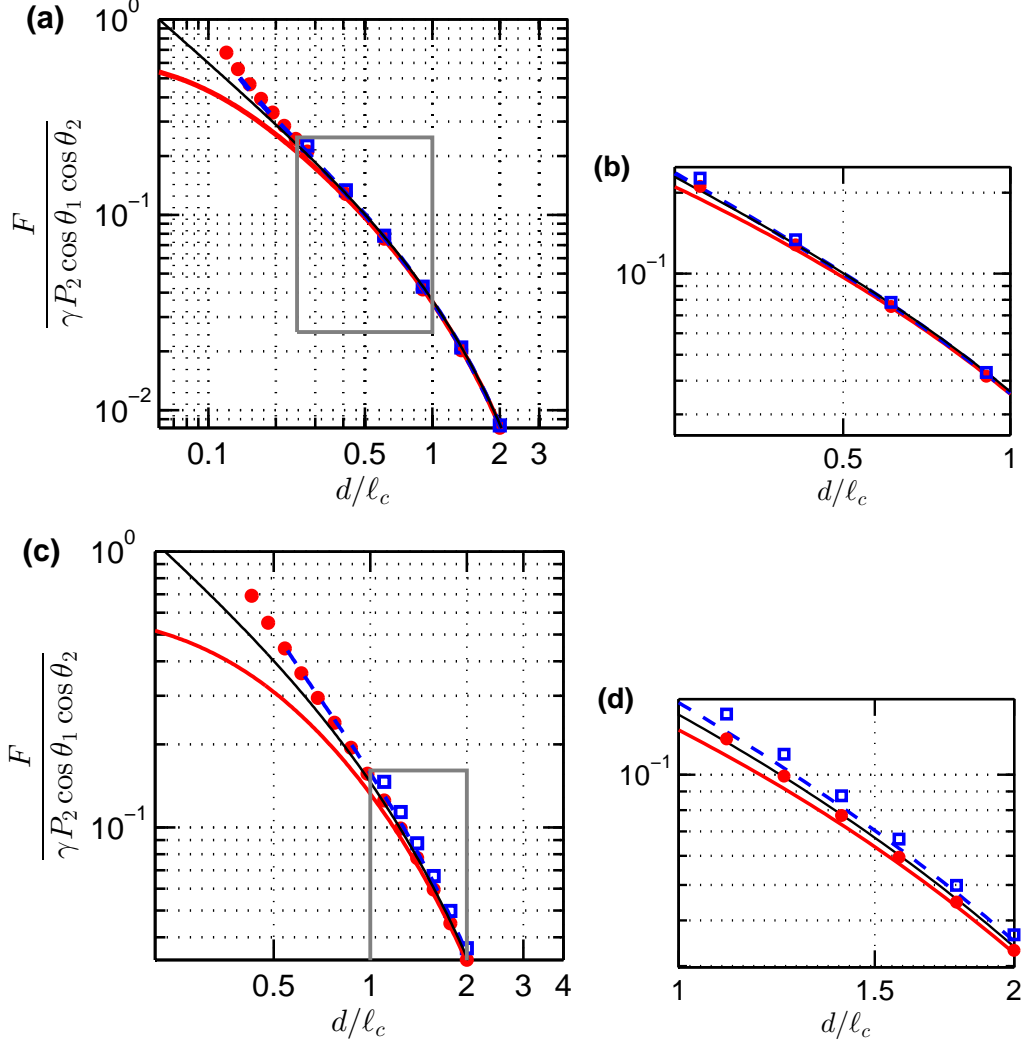


Figure 4.7: Force of attraction between pairs of elliptical cylinders. (a) and (b): a pair of small cylinders with  $s = 0.0920 \ell_c$  and  $t = 0.0092 \ell_c$ ; (c) and (d): a pair of larger cylinders with  $s = 0.3600 \ell_c$  and  $t = 0.0360 \ell_c$ . The regions shown in gray boxes are zoomed-in in the left panel. For both cases, the cylinder aspect ratio is  $s/t = 10.000$ , and the physical properties are  $\theta = 70^\circ$ ,  $\gamma = 72.4 \text{ mN m}^{-1}$ ,  $\rho_l = 1000 \text{ kg m}^{-3}$ ,  $\rho_v = 0$ , ( $\ell_c = 2.717 \text{ mm}$ ).  $\bullet$  denotes the numerical solution for side-to-side attraction,  $\square$  denotes the numerical solution for tip-to-tip attraction, solid red curve (—) denotes the asymptotic result for side-to-side attraction (Eq. 4.67), dashed blue curve (---) denotes the asymptotic result for tip-to-tip attraction (Eq. 4.60), and solid black curve (—) denotes the force of attraction between two circular cylinders with  $R = R_P$ , which is the equivalent radius obtained in Eq. (4.84). The asymptotic results match with the numerical solution at far range, and deviations occur at close range. Both methods of solution show the force in the tip-to-tip configuration is larger than in the side-to-side configuration. The approximation with the equivalent radius  $R_P$  correctly captures the far-range behaviour.

### 4.3 Approximation of the meniscus far away from the cylinder

As  $u \rightarrow \infty$ , the contours of constant  $u$  in elliptic cylindrical coordinates tend to circles with radius

$$r \sim a \cosh u, \quad (4.68)$$

and the angle measured around the centre of the cylinder tends to  $v$  so that:

$$\alpha \sim v. \quad (4.69)$$

As described in [McLachlan \(1964\)](#), in this range, the Mathieu functions can be approximated in a simpler form so that

$$\text{Fek}_{2n}(u, -q) \sim p'_{2n} \frac{1}{\pi} K_{2n} \left( \frac{2\sqrt{-q}}{a} r \right), \quad (4.70)$$

where  $p'$  is defined in Eq. (4.35). Using the definition of  $q$  from Eq. (4.22), on the above equation:

$$\text{Fek}_{2n}(u, -q) \sim p'_{2n} \frac{1}{\pi} K_{2n} \left( \frac{r}{\ell_c} \right). \quad (4.71)$$

Using this on Eq. (4.43), along with the definition of  $p'_{2n}$  (Eq. 4.35) yields

$$\zeta(r, \alpha) = -\frac{a \cos \theta}{\sqrt{2} \pi^2} \sum_{n=0}^{\infty} \frac{C_{2n} (-1)^n \text{ce}_{2n}(\pi/2, q) \text{ce}_{2n}(0, q) \text{ce}_{2n}(\alpha, -q)}{A_0^{(2n)} \text{Fek}'_{2n}(u_0, -q)} K_{2n} \left( \frac{r}{\ell_c} \right). \quad (4.72)$$

We simplify this expression by taking only the first term of the infinite series so that:

$$\zeta(r, \alpha) = -\frac{a \cos \theta}{\sqrt{2} \pi^2} \frac{C_0 \text{ce}_{2n}(\pi/2, q) \text{ce}_{2n}(0, q) p'_0 \text{ce}_0(\alpha, -q)}{A_0^{(2n)} \text{Fek}'_0(u_0, -q)} K_0 \left( \frac{r}{\ell_c} \right). \quad (4.73)$$

### 4.3. Approximation of the meniscus far away from the cylinder

---

We now compare this result with the height of meniscus around a circular cylinder, which was given in Eq. 3.16 to be

$$\zeta_{\text{circular}}(r) = R \cos \theta K_0 \left( \frac{r}{\ell_c} \right), \quad (4.74)$$

and define an “effective radius”  $R_{\text{eff}}$  so that the meniscus far away from an elliptical cylinder is equivalent to that by a circular cylinder with radius  $R_{\text{eff}}$ :

$$R_{\text{eff}}(\alpha) = -\frac{a}{\sqrt{2}} \frac{C_0 \text{ce}_{2n}(\pi/2, q) \text{ce}_{2n}(0, q) p'_0 \text{ce}_0(\alpha, -q)}{\pi^2 A_0^{(2n)} \text{Fek}'_0(u_0, -q)}, \quad (4.75)$$

and hence

$$\zeta(r, \alpha) = R_{\text{eff}}(\alpha) \cos \theta K_0(r/\ell_c). \quad (4.76)$$

If another elliptical cylinder is introduced at a distance  $d$  which is sufficiently far away from the first cylinder the force acting on the second cylinder is given asymptotically

$$F = \frac{1}{\ell_c} R_{\text{eff},1}(\alpha) \cos \theta_1 \cos \theta_2 K_1(d/\ell_c) P_2, \quad (4.77)$$

where  $P_2$  is the perimeter of the second cylinder. According to Newton’s third law, the force acting on the first cylinder must be equal to the force acting on the second cylinder i.e.

$$\frac{1}{\ell_c} R_{\text{eff},1}(\alpha) \cos \theta_1 \cos \theta_2 K_1(d/\ell_c) P_2 = \frac{1}{\ell_c} R_{\text{eff},2}(\alpha + \pi) \cos \theta_2 \cos \theta_1 K_1(d/\ell_c) P_1. \quad (4.78)$$

Because of the periodicity of the Mathieu functions we have

$$\text{ce}_{2n}(\alpha) = \text{ce}_{2n}(\alpha + \pi). \quad (4.79)$$

Using this on Eq. (4.75) gives

$$R_{\text{eff}}(\alpha) = R_{\text{eff}}(\alpha + \pi). \quad (4.80)$$

Then Eq. (4.78) simplifies to

$$\frac{R_{eff,1}(\alpha)}{R_{eff,2}(\alpha)} = \frac{P_1}{P_2}. \quad (4.81)$$

Because of the above relationship we hypothesize that  $R_{eff}$  may approximately be linearly related to  $P$ :

$$R_{eff}(\alpha) \approx R_P(\alpha) \quad (4.82)$$

$$= k(\alpha)P. \quad (4.83)$$

The following procedure was used to determine the constant of proportionality  $k$ : For a selected value of the major axis  $s$ , an array of values were selected for the minor axis  $t$ , ranging from  $t = 10^{-9}\ell_c$  to  $t = s - 10^{-10}\ell_c$ . As shown in figure 4.8 (a) and (b),  $R_{eff}(0)$  and  $R_{eff}(\pi/2)$  were calculated for each  $t$ .  $P$  was also calculated using Eq. (4.49). For most values of  $s$  and  $t$ , the ratio  $2\pi R_{eff}/P$  was reasonably close to 1. Then  $k(0)$  and  $k(\pi/2)$  were then determined by least squares fitting of  $R_{eff}$  with  $P$ . This then gives the approximation  $R_P$  (Eqs. 4.82 and 4.83). Figure 4.8 (c) shows  $R_P$  obtained by repeating the above procedure for a wide range of values of  $s$ . It shows that when  $s \ll \ell_c$ ,

$$R_P(0) \approx R_P(\pi/2) \approx \frac{P}{2\pi}. \quad (4.84)$$

This result is very significant because it means that regardless of the ellipticity of the cylinder, at far range, the meniscus is equivalent to one produced by a circular cylinder with the same perimeter. Figure 4.8 (a) and (b) show that this approximation is not affected by the aspect ratio of the cylinder. It only becomes invalid when  $s$  is in the range of, or larger than, the capillary length, where the meniscus height varies with  $v$  at far range as well. This simple approximation of  $R_{eff}$  by  $R_P$  might be applicable to vertical objects with cross sectional shapes other than ellipses as well. This prediction can be tested using numerical solutions as future work.

The black curves in figure 4.7 show the force of attraction between pairs of circular cylinders with radius  $R_P$  (Eq. 4.84). This is a good approximation for the

force of attraction between two elliptical cylinders. At close range, this approximation represents an intermediate value between the asymptotically determined side-to-side and tip-to-tip attraction forces which start to deviate from one another.

## 4.4 Numerical solution of the nonlinear Laplace–Young equation

Numerical solutions of the Laplace–Young equation were also computed for this problem. The numerical scheme described in section 2.3 was used to solve the nonlinear Laplace–Young equation and the nonlinear boundary condition for the meniscus shape around two elliptical cylinders. Note that the numerical solutions described here are of the fully nonlinear equation; this is in contrast to the asymptotic solution of the previous section where the linearized problem was solved.

As in section 3.3, the boundary condition and the Laplace–Young equation are solved using an iterative method. The values of the nonlinear terms of the  $N^{\text{th}}$  step of this iterative scheme are obtained using the meniscus heights calculated in the  $(N - 1)^{\text{st}}$  step. The boundary condition (Eq. 4.10) is implemented as

$$\frac{\sinh u_0 \cos v \zeta_x^{[N]} + \cosh u_0 \sin v \zeta_y^{[N]}}{[\sqrt{\zeta_x^2 + \zeta_y^2 + 1}]^{[N-1]}} = -\cos \theta \sqrt{\frac{\cosh 2u_0 - \cos 2v}{2}}. \quad (4.85)$$

To determine the meniscus around an isolated elliptical cylinder numerically, the nodes are positioned along ellipses originating from the cross section of the cylinder. Each ellipse is obtained by adding an equal length to the major axis and minor axis of the preceding ellipse. The added length is made gradually larger so that the distance between consecutive ellipses increases. As a result, the density of nodes is highest near the boundary of the cylinder where the meniscus slope is the highest. Because an equal length is added to both the major axis and the minor axis, the ellipses also become more and more circular towards the edge of the domain. For each ellipse,  $u$  and  $a$  are calculated using Eq. (4.6) and Eq. (4.5) respectively. A linear spacing in  $v$  is then selected and the locations of the nodes

#### 4. Elliptical cylinders at a liquid–gas interface

---

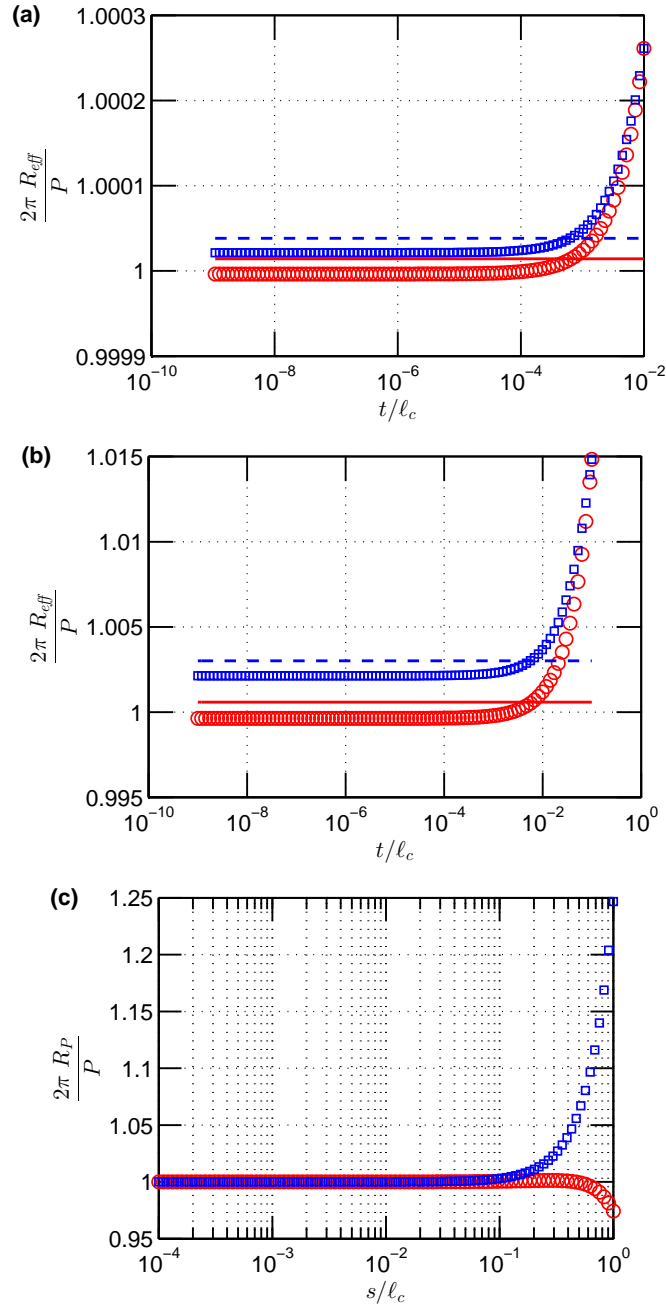


Figure 4.8: Obtaining an approximation for the effective radius  $R_{eff}$  using perimeter  $P$ . The first two figures show  $R_{eff}$  calculated for a range of values for minor axis  $t$  keeping the major axis fixed at (a):  $s = 0.01\ell_c$  and (b):  $s = 0.1\ell_c$ .  $\square$  is  $R_{eff}(0)$  and  $\circ$  is  $R_{eff}(\pi/2)$ . The equivalent radius  $R_P$ , which linearly depends on  $P$ , was obtained by least squares fitting of  $R_{eff}$  vs  $P$ . Dashed blue curve ( $--$ ) is  $R_P(0)$  and dashed red curve ( $--$ ) is  $R_P(\pi/2)$ . (c) shows the values of  $R_P$  obtained by repeating this calculation for a range of  $s$ , with  $\square$  showing  $R_P(0)$  and  $\circ$  showing  $R_P(\pi/2)$ . It shows that for sufficiently small cylinders  $R_P \approx P/(2\pi)$ .

are calculated using Eq. (4.2) and Eq. (4.3). This ensures a relatively higher nodal density near the regions around the tips of each ellipse, which also has a higher meniscus slope. When solving for the meniscus around a pair of cylinders, the above procedure is carried out for each cylinder to position the nodes. In this case, the ellipses are clipped along the centre line between the two cylinders to avoid them intersecting each other, as in section 3.3.

Figures 4.4(b) and 4.5(b) show the numerically calculated meniscii shapes produced by the code for isolated elliptical cylinders of different ellipticity. They also show the relative error between the two solutions calculated as

$$E = \frac{\zeta_{analytical} - \zeta_{numerical}}{\zeta_{numerical}}. \quad (4.86)$$

Regardless of the aspect ratio of the cylinder, the numerical and asymptotic predictions match with each other very well. There is a discrepancy at the edge of the domain because in the numerical solution, the meniscus height is forced to satisfy  $\zeta = 0$  here, while in the asymptotic solution the meniscus height tends to 0 infinite distance away from the cylinder.

The red symbols in figure 4.6 show numerically obtained contact line heights for elliptical cylinders of different ellipticity, and the blue curves show the predictions of the asymptotic solution. The numerical and asymptotic solutions show very good agreement with each other even for a cylinder with a large aspect ratio. This shows that the asymptotic solution of the meniscus height is sufficiently accurate even close to the cylinder.

As a point of reference, the green curves in the figure show the corresponding meniscus height for a circular cylinder with radius  $R$  equal to the mean of the lengths of the major and minor axes of the elliptical cylinders. The meniscus height around a circular cylinder is given by Eq. (3.16), i.e.  $\zeta(r) = R \cos \theta K_0(r/\ell_c)$ , where  $r$  is the distance from the centre of the cylinder. In performing this comparison, we take

$$r = \sqrt{x^2 + y^2}, \quad (4.87)$$

where  $(x, y)$  is a point on the ellipse produced by the above boundary.  $r$  is then substituted into Eq. (3.16) to obtain  $\zeta$ . Because of the elliptical geometry,  $r$  is not constant along the boundary. As a result  $\zeta$  descends near the tips of the ellipse,

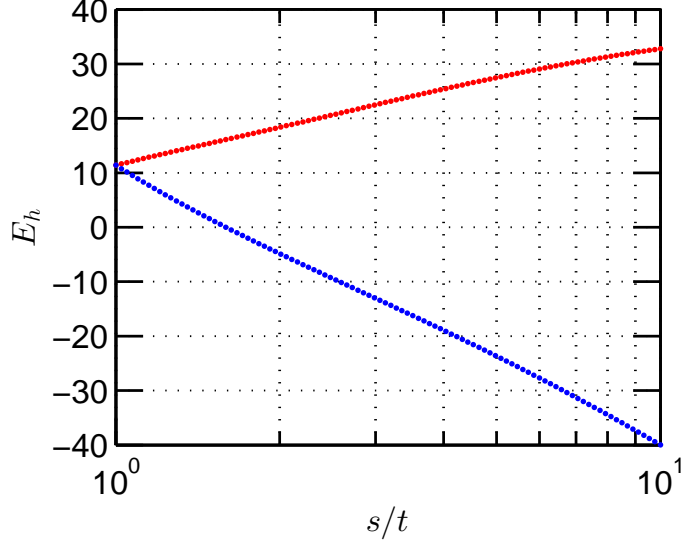


Figure 4.9: Percentage error ( $E_h$ ) between the contact line height around an elliptical cylinder obtained using two methods: asymptotic solution for an elliptical cylinder and asymptotic solution for a circular cylinder. For the first method, Eq. 4.43 gives the solution for the meniscus height around an elliptical cylinder. Using  $u = u_0$  on this equation gives the contact line height. For the second method, Eq. (3.16) gives the meniscus profile around a circular cylinder. Using this solution for a circular cylinder with  $R = (s + t)/2$ , the meniscus height along the elliptical boundary of the cylinder was calculated. The physical properties of the system are  $\theta = 70^\circ$ ,  $\gamma = 72.4 \text{ mN m}^{-1}$ ,  $\rho_l = 1000 \text{ kg m}^{-3}$ ,  $\rho_v = 0$ ,  $\ell_c = 2.717 \text{ mm}$ .  $t$  is varied keeping  $s$  fixed at  $0.372\ell_c$ .  $E_h$  is calculated using Eq. 4.88 for two different values of  $\alpha$ . The red symbols ( $\bullet$ ) corresponds to  $\alpha = 0$ , and the blue symbols ( $\bullet$ ) corresponds to  $\alpha = \pi/2$ . The error does not converge to 0 at an aspect ratio of 1 because the asymptotic solution for a circular cylinder is only accurate for far range distances of cylinders with  $R \ll \ell_c$ .

where  $r$  is higher, and rises at the sides, where  $r$  is smaller, as seen from the figure. The black curves are calculated in a similar way but using the radius  $R = R_P$ , which is given in Eq. (4.84), rather than the mean. In summary figure 4.6 shows that these approximations generally do not represent the observed contact line shapes satisfactorily, especially for cylinders with large aspect ratios.

According to figure 4.6 (a), even when the aspect ratio of the cylinder as small as 1.022, the prediction made by the circular cylinder approximation has an error larger than 12%. This is effect further analyzed in figure 4.9. The percentage

error is calculated using

$$E_h = \frac{h_{c,elliptical} - h_{c,circular}}{h_{c,elliptical}} \times 100, \quad (4.88)$$

where  $h_{c,elliptical}$  is the contact line height given by the asymptotic solution for the meniscus height around an elliptical cylinder Eq. (4.43) and  $h_{c,circular}$  is the meniscus height along the boundary of the elliptical cylinder obtained using the asymptotic solution for the meniscus height around a circular cylinder Eq. 3.16 with  $R = (s + t)/2$ . Figure 4.9 shows that the error does not reach 0 even as the aspect ratio approaches 1. This is caused by the asymptotic solution for the circular cylinder losing its accuracy at short distance ranges relative to  $R$ , and also at values of  $R$  close to  $\ell_c$ .

## 4.5 Numerical determination of the forces of attraction

### 4.5.1 Force due to surface tension

As shown in figure 4.1, the surface tension force vector lies in the plane containing  $\hat{\mathbf{n}}$  (the outward unit normal to the surface of the cylinder) and  $\hat{\mathbf{b}}$  (the binormal to  $\hat{\mathbf{n}}$  and the unit tangent to the three-phase contact line  $\hat{\mathbf{t}}$ ). These vectors need to be determined in order to calculate the force. We re-write  $\hat{\mathbf{n}}$ , which is already given in Eq. (4.9), in a slightly different notation:

$$\hat{\mathbf{n}} = \frac{1}{\xi} (\sinh u_0 \cos v \mathbf{e}_x + \cosh u_0 \sin v \mathbf{e}_y), \quad (4.89)$$

with  $\xi$  given in Eq. (4.48). The position vector of a point on the three-phase contact line is given in Cartesian coordinates by

$$\mathbf{P} = a \cos v \cosh u_0 \mathbf{e}_x + a \sin v \sinh u_0 \mathbf{e}_y + \zeta \mathbf{e}_z. \quad (4.90)$$

The unit tangent vector  $\hat{\mathbf{t}}$  can be obtained by differentiating this:

$$\begin{aligned}\hat{\mathbf{t}} &= -\frac{\partial \mathbf{P}}{\partial v} \bigg/ \left| \frac{\partial \mathbf{P}}{\partial v} \right| \\ &= \frac{1}{\tau} \left( a \cosh u_0 \sin v \mathbf{e}_x - a \sinh u_0 \cos v \mathbf{e}_y - \frac{\partial \zeta}{\partial v} \mathbf{e}_z \right),\end{aligned}\quad (4.91)$$

where

$$\tau = \sqrt{a^2 \xi^2 + \left( \frac{\partial \zeta}{\partial v} \right)^2}.\quad (4.92)$$

From this, we can calculate the unit binormal vector to  $\hat{\mathbf{n}}$  and  $\hat{\mathbf{t}}$  as:

$$\begin{aligned}\hat{\mathbf{b}} &= \hat{\mathbf{n}} \times \hat{\mathbf{t}} \\ &= \frac{1}{\xi \tau} \left( -\cosh u_0 \sin v \frac{\partial \zeta}{\partial v} \mathbf{e}_x + \sinh u_0 \cos v \frac{\partial \zeta}{\partial v} \mathbf{e}_y - a \xi^2 \mathbf{e}_z \right).\end{aligned}\quad (4.93)$$

As shown in Eq. (2.17), the contact angle  $\theta$  is defined in the plane containing  $\mathbf{b}$  and  $\mathbf{n}$  so that  $\hat{\mathbf{b}} \cdot \hat{\boldsymbol{\gamma}} = \cos \theta$ , where  $\hat{\boldsymbol{\gamma}}$  is the unit tangent to the liquid interface in the above plane, which is also the direction of the surface tension force. We define the surface tension force vector

$$\boldsymbol{\gamma} = \gamma \hat{\boldsymbol{\gamma}},\quad (4.94)$$

where the scalar  $\gamma$  is the surface tension of the liquid–fluid interface. Consistently with Eq. (3.2) the surface tension force acting on the cylinder is now given by

$$\mathbf{F}_{st} = \oint \boldsymbol{\gamma} \, ds$$

where  $ds$  is an infinitesimal arc length along the contact line, which is now given by

$$\begin{aligned}ds &= \sqrt{\frac{\partial \mathbf{P}}{\partial v} \cdot \frac{\partial \mathbf{P}}{\partial v}} \, dv \\ &= \tau \, dv.\end{aligned}\quad (4.95)$$

In Eq. (3.5), the vector  $\boldsymbol{\gamma}$  was decomposed into components in the directions

of  $\hat{\mathbf{b}}$  and  $\hat{\mathbf{n}}$  as  $\boldsymbol{\gamma} = \gamma(\hat{\mathbf{n}} \sin \theta + \hat{\mathbf{b}} \cos \theta)$ . Using this result along with the expressions for  $\hat{\mathbf{n}}$  and  $\hat{\mathbf{b}}$  (Eqs. 4.89, 4.93) we can obtain the components of  $\boldsymbol{\gamma}$  in the  $x$  and  $y$  directions:

$$\gamma_x = \gamma \left[ \frac{1}{\xi} \sinh u_0 \cos v \sin \theta - \frac{1}{\xi \tau} \cosh u_0 \sin v \frac{\partial \zeta}{\partial v} \cos \theta \right], \quad (4.96)$$

$$\gamma_y = \gamma \left[ \frac{1}{\xi} \cosh u_0 \sin v \sin \theta + \frac{1}{\xi \tau} \sinh u_0 \cos v \frac{\partial \zeta}{\partial v} \cos \theta \right]. \quad (4.97)$$

Combining the two equations above with Eq. (3.2) and Eq. (4.95) we obtain the force due to surface tension in the  $x$  direction as

$$F_{st}^{(x)} = \gamma \int_0^{2\pi} \left( \frac{\tau}{\xi} \sinh u_0 \cos v \sin \theta - \frac{1}{\xi} \cosh u_0 \sin v \frac{\partial \zeta}{\partial v} \cos \theta \right) dv, \quad (4.98)$$

and the force due to surface tension in the  $y$  direction as

$$F_{st}^{(y)} = \gamma \int_0^{2\pi} \left( \frac{\tau}{\xi} \cosh u_0 \sin v \sin \theta + \frac{1}{\xi} \sinh u_0 \cos v \frac{\partial \zeta}{\partial v} \cos \theta \right) dv. \quad (4.99)$$

### 4.5.2 Force due to hydrostatic pressure

The hydrostatic pressure force acting on an elemental area on the surface of the cylinder is

$$d^2 F_{hp} = h \rho g \, dh \, dl, \quad (4.100)$$

where  $\rho$  is the density of the fluid,  $h$  is the depth and  $l$  is as defined in Eq. (4.47).

Then the hydrostatic pressure force in the  $x$  direction is given by

$$F_{hp}^{(x)} = \int_0^{2\pi} \int_0^\zeta h \rho g \, dh \, a \xi n_x \, dv, \quad (4.101)$$

where  $n_x$  is the  $x$  component of the vector  $\hat{\mathbf{n}}$  in Eq. (4.89). Performing the

integration gives

$$F_{hp}^{(x)} = \frac{1}{2} a \sinh u_0 \Delta \rho g \int_0^{2\pi} \zeta^2 \cos v \, dv, \quad (4.102)$$

where  $\Delta \rho$  is the density difference between the two fluids. Similarly, the pressure force in the  $y$  direction is given by

$$F_{hp}^{(y)} = \frac{1}{2} a \cosh u_0 \Delta \rho g \int_0^{2\pi} \zeta^2 \sin v \, dv. \quad (4.103)$$

### 4.5.3 Total force of attraction

The total force acting on one cylinder is then obtained by adding the surface tension and the hydrostatic pressure forces together:

$$F_x = F_{st}^{(x)} + F_{hp}^{(x)}, \quad (4.104)$$

$$F_y = F_{st}^{(y)} + F_{hp}^{(y)}. \quad (4.105)$$

The blue and red symbols in figure 4.7 show the numerically determined force of attraction between pairs of identical elliptical cylinders. As was found for the asymptotic solution, the tip–to–tip force is larger than the side–to–side force when the two cylinders are close to one another; as the objects move further apart, the difference between the two forces diminish. When the two cylinders are sufficiently far away from each other, the force predicted by the asymptotic solution matches well with the numerical solution. As the objects move closer, the numerical solution deviates from the asymptotic solution. This is due to the inaccuracy of the approximations of linear superposition of the menisci and small meniscus slopes used in the asymptotic solution.

## 4.6 Concluding remarks on elliptical cylinders

An accurate numerical solution was developed to determine the meniscus shape around a vertical elliptical cylinder by solving the nonlinear Laplace–Young equation. An asymptotic solution was also developed for the meniscus shape around

an isolated elliptical cylinder. The three phase contact lines and meniscus profiles predicted by the two methods of solution agree very well even for elliptical cylinders with large aspect ratios. Using the numerical solution, the meniscus around a pair of elliptical cylinders was computed and the force of attraction between them was determined. The force was also estimated using the asymptotic solution by linear superposition of the menisci from individual cylinders. Both methods show that the force of attraction in the tip-to-tip configuration is higher than that in the side-to-side configuration when the two cylinders are close to one another. When the distance between the cylinders was sufficiently large, the force in the two configurations was found to be the same.

Considering the properties of the asymptotic solution, it was found that the meniscus created by an elliptical cylinder was identical to that created by a circular cylinder at large distances. The radius of this effective circular cylinder,  $R_{eff}$ , was also calculated. A simpler approximation for  $R_{eff}$  was sought; when the major axis of the elliptical cylinder was smaller than the capillary length, it was found that the radius ( $R_P$ ) of a circular cylinder with the same perimeter as the elliptical cylinder was a very good approximation to  $R_{eff}$ . The force of attraction between a pair of circular cylinders with radius  $R_P$  was found to be same as the force of attraction between two elliptical cylinders at far range as predicted by both the numerical and asymptotic solutions.

## 4.A Deriving the linearized boundary condition (Eq. 4.14) for the meniscus around an elliptical cylinder

The elliptic cylindrical coordinates (see figure 4.2) have the following identities:

$$\frac{x^2}{\cos^2 v} - \frac{y^2}{\sin^2 v} = a^2, \quad (4.106)$$

$$\frac{x^2}{\cosh^2 u} + \frac{y^2}{\sinh^2 u} = a^2. \quad (4.107)$$

Additionally, by differentiating Eq. (4.106) and Eq. (4.107) and substituting from Eq. (4.2) and Eq. (4.3) we obtain

$$v_x = \frac{2 \cosh u \sin v}{-a \cosh 2u + a \cos 2v} \quad (4.108)$$

$$v_y = \frac{2 \sinh u \cos v}{a \cosh 2u - a \cos 2v} \quad (4.109)$$

$$u_x = \frac{1}{a \sinh u \cos v + a \cosh u \coth u \sin v \tan v} \quad (4.110)$$

$$u_y = \frac{1}{a \cosh u \sin v + a \sinh u \tanh u \cos v \cot v}. \quad (4.111)$$

In order to expression the boundary condition Eq. (4.13) in elliptic cylindrical coordinates, we need to replace the  $x$  and  $y$  derivatives with  $u$  and  $v$  derivatives. Using the chain rule:

$$\zeta_x = \zeta_v v_x + \zeta_u u_x, \quad (4.112)$$

$$\zeta_y = \zeta_v v_y + \zeta_u u_y, \quad (4.113)$$

substituting the identities given in Eqs. (4.108 - 4.111) into Eq. (4.112) and (4.113) gives  $\zeta_x$  and  $\zeta_y$  in terms of  $u$  and  $v$ , which in combination with Eq. (4.13) finally yields Eq. (4.14).

# Chapter 5

## Floating (and sinking) of spheres at a liquid–fluid interface

A defining (and simplifying) feature of the analysis presented in Chapters 3 and 4 is that the objects are assumed in a known configuration. This may be realistic if the objects are supported by means of an externally applied force. In reality, however, it is more common for the objects of interest to be floating e.g. the range of animals that live on the surface of water. The mechanisms used by such animals to support themselves on the surface of water were reviewed by [Bush and Hu \(2006\)](#). Of these animals, the water strider has received significant attention recently: These arthropods have a layer of hair on their legs which repel water, and in turn, create a large surface tension force which supports their weight on water ([Bush et al., 2007](#); [Gao and Jiang, 2004](#)).

It is the balance between the object’s weight and the vertical restoring force provided by surface tension that determines *where* the object sits at the interface and hence the extent of the attraction between floating objects. However, if an object is too heavy then surface tension may not be enough to support it at the interface, and it may sink.

Determining under which conditions an object will float or sink is vital for both understanding the selection pressures on water–walking insects ([Vella, 2008](#)) and developing technologically viable self assembly methods. [Vella et al. \(2006a\)](#) determined the maximum load that an infinitely long horizontally floating cylin-

der can support without sinking, while [Liu et al. \(2007\)](#) analytically determined under which conditions a similar cylinder with an elliptical, triangular or hexagonal cross sections can remain floating. [Kim et al. \(2010\)](#) carried out experiments and analytical solutions in search of a cross sectional shape of a horizontal cylinder that can remain floating under a maximum load. Out of the shapes they tested, a cylinder with a “Y” shaped cross section was found to be the best.

While infinitely long cylinders are a useful paradigm within which to understand the water–walking of insects, floating spheres are of more interest for practical applications. By means of a numerical solution, [Vella et al. \(2006a\)](#) calculated the maximum density at which small spheres can float. This was experimentally studied by [Extrand and Moon \(2009\)](#), where they placed a sphere in an empty container and gradually filled with a liquid to determine under which conditions the liquid will float the sphere without engulfing it. [Liu et al. \(2009\)](#) placed a sphere at a liquid interface, and determined its floating behavior by varying the surface tension.

Multiple spheres placed at a liquid–fluid interface usually attract and produce aggregates as shown analytically by [Chan et al. \(1981\)](#); [Vella and Mahadevan \(2005\)](#), and experimentally by [Dalbe et al. \(2011\)](#). When multiple objects move towards aggregation, their floating behaviour can be different from that of isolated particles. This has previously been shown to be true for a pair of infinitely long horizontal cylinders ([Vella et al., 2006b](#)). They showed that cylinders which can float in isolation may sink as they approach one another. Several experiments have been carried out to determine the collective floating behavior of particles: [Larmour et al. \(2008\)](#) observed the loads supported by rough copper granules aggregated on water, and [Lu et al. \(2012\)](#) also experimentally studied the loading capacity of structures produced by aggregation of superhydrophobic aluminium hexagons. However, unlike for infinite cylinders, there has been no theoretical results predicting that the floating conditions of an aggregate of finite–sized particles can be different from the floating of a particle in isolation.

This chapter presents a precise numerical solution for the floating and sinking behaviour of a multiple sphere system. For the first time, this proves that the collective floating behaviour of spherical particles can indeed be different from that of an isolated sphere. I also present an approximate “semi-analytical” solu-

tion which is simpler, and yet captures some of the most interesting predictions of the numerical solution.

Unlike the analyses presented in the previous chapters, the vertical force balance is taken into account here in determining the position of the sphere and hence the contact line. There are three main forces which act on a sphere floating at a liquid–fluid interface: the force of surface tension, the hydrostatic pressure force exerted by the fluid, and the weight of the sphere itself. In the analysis presented here, we neglect any other interactions (e.g. electrostatic or dispersion) in comparison to the above forces. The validity of this assumption depends on the detailed surface chemistry of the spheres and their size. It is generally true for spheres larger than a few tens of microns.

Since the vertical position of each floating sphere is not known *a priori*, the position and shape of the three-phase contact line is also unknown. This further complicates the problem because the form of the boundary condition and the location at which it should be applied in order to solve the Laplace–Young equation depend on the configuration of the three-phase contact line. In particular, for multiple spheres, the three-phase contact line does not lie in a horizontal plane, making the solution of this problem especially difficult. In this chapter, I present numerical and asymptotic results that address this problem.

For an isolated sphere floating at a liquid–fluid interface, as shown in figure 5.1, the contact line is horizontal, and therefore the interfacial shape is axisymmetric. It is a relatively simple matter to solve for the equilibrium of such a sphere. An approximate analytical solution has been made for this system (Rapacchietta and Neumann, 1977; Vella et al., 2006a), which is summarized in section 5.1. We then consider a pair of spheres in section 5.2.

## 5.1 An isolated sphere

The setup of an isolated sphere is shown in figure 5.1, the inclination of the meniscus to the horizontal plane at the contact line ( $\psi$ ) is related to the contact angle  $\theta$  by

$$\psi = \theta - \omega. \tag{5.1}$$

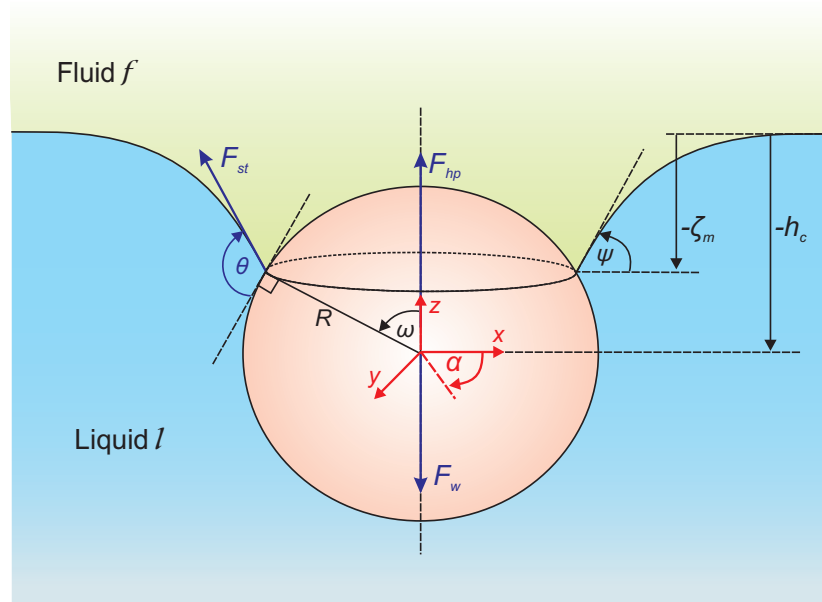


Figure 5.1: Configuration of an isolated floating sphere. This problem is simpler than the case of many spheres because the contact line is horizontal.  $R$  is the radius of the sphere, and  $\theta$  is the contact angle.  $\omega$  is the angle measured from the centre of the sphere to any point on the contact line (for multiple spheres,  $\omega = \omega(\alpha)$ ). The forces acting on the sphere are surface tension ( $F_{st}$ ), buoyancy ( $F_{hp}$ ) and weight ( $F_w$ ).

$\zeta_m$  is the depth of the contact line. Mansfield et al. (1997) presented the “Generalized Archimedes principle” which showed that for an object floating at a liquid-gas interface, the total upwards vertical force is equal to the total weight of liquid  $l$  displaced by the object and the meniscus around it. The weight of liquid displaced by the meniscus is equal to the surface tension force, and that displaced by the object is equal to the buoyancy force. Even if the upper fluid  $f$  has a non-zero density, the force of buoyancy exerted by the liquid  $l$  is not affected by the geometry of the object that is not in contact with this liquid. Vella and Mahadevan (2005) applied this principle for a spherical object and showed that the vertical hydrostatic pressure force exerted *upwards* on the sphere by liquid  $l$  is equivalent to the weight of liquid  $l$  that would occupy the section of the sphere immersed in liquid  $l$  and the volume of a cylindrical region with a cross section equal to the cross section of the meniscus around the sphere and a height equal

to the meniscus depth  $-\zeta_m$ . Similarly, the vertical hydrostatic pressure force of exerted *downwards* on the sphere by the fluid  $f$  is the weight of liquid  $f$  that occupies the above cylindrical region minus the part of the sphere immersed in the fluid  $f$ . Therefore, the net vertical hydrostatic pressure acting upwards on the sphere  $F_{hp}^{(z)}$  is:

$$F_{hp}^{(z)} = \pi R^3 (\rho_l - \rho_f) g \left( \frac{2}{3} + \cos \omega - \frac{1}{3} \cos^3 \omega - \frac{\zeta_m}{R} \sin^2 \omega \right) + \frac{4}{3} \pi R^3 \rho_f g, \quad (5.2)$$

where  $\rho_l$  and  $\rho_f$  are the densities of the liquid and fluid respectively. The surface tension force acting on the sphere is given by

$$F_{st}^{(z)} = 2\pi\gamma R \sin \omega \sin \psi. \quad (5.3)$$

In equilibrium, these two forces must balance the weight of the sphere, so we have

$$\begin{aligned} \frac{4}{3} \pi R^3 \rho_s g = & \pi R^3 (\rho_l - \rho_f) g \left( \frac{2}{3} + \cos \omega - \frac{1}{3} \cos^3 \omega - \frac{\zeta_m}{R} \sin^2 \omega \right) \\ & + \frac{4}{3} \pi R^3 \rho_f g + 2\pi\gamma R \sin \omega \sin \psi, \end{aligned} \quad (5.4)$$

where  $\rho_s$  is the density of the sphere.  $\zeta_m$  is the same as the meniscus depth of a vertical cylinder with radius  $R \sin \omega$  and contact angle  $\psi$ . Eq. (5.4) can be simplified by assuming  $\psi$  to be small, which makes  $\zeta_m \rightarrow 0$ , and according to Eq. (5.1),  $\omega \rightarrow \theta$ . Using this assumption as in (Chan et al., 1981) we obtain the approximate equilibrium condition of a single sphere to be:

$$\sin(\theta - \omega) \sin \omega = \frac{R^2 (\rho_l - \rho_f) g}{\gamma} \left[ \frac{2 (\rho_s - \rho_f)}{3 (\rho_l - \rho_f)} - \frac{1}{3} - \frac{1}{2} \cos \theta + \frac{1}{6} \cos^3 \theta \right]. \quad (5.5)$$

Instead of using the above approximation, one can eliminate  $\zeta_m$  from Eq. (5.4) by obtaining a relationship between  $\zeta_m$  and  $\psi$  from the numerical solution of the Laplace–Young equation in cylindrical coordinates. (This is a one–dimensional problem because of the axisymmetry of the meniscus). This method enables accurate determination of the equilibrium of a single floating sphere and also the maximum density of a sphere that can float, as demonstrated by Vella et al.

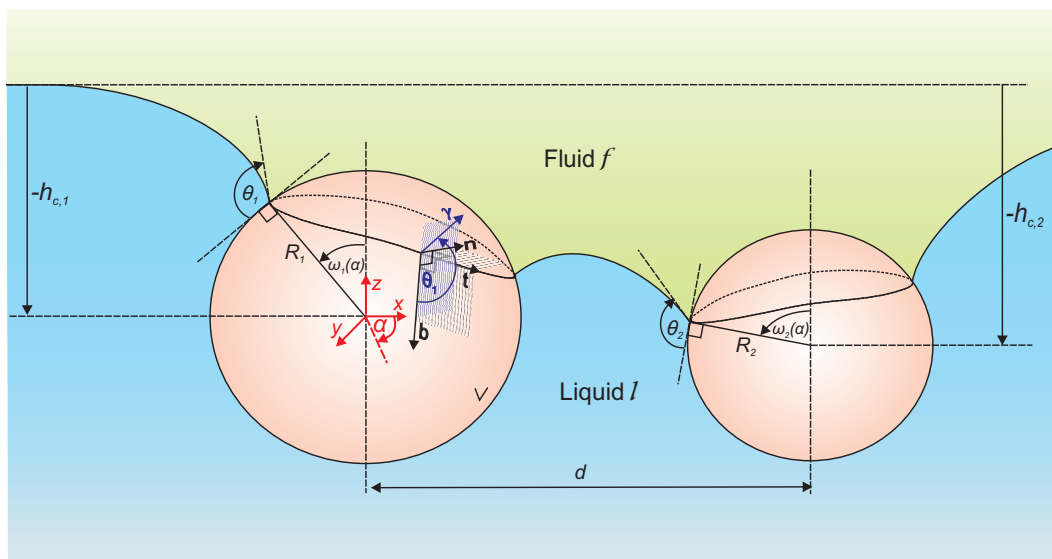


Figure 5.2: A pair of spheres floating at a liquid interface. The contact angles  $\theta_1$  and  $\theta_2$  give the boundary conditions where the interface meets the sphere. Far away, the interface is required to return to the natural liquid level, indicated by the horizontal dashed line.

(2006a).

However, there has been no solution to date for the equilibrium of a system of spheres which are close enough for their interactions to be significant. Figure 5.2 shows such a system with two spheres, where the contact lines are not horizontal. Unlike the case of a single sphere, one cannot assume axisymmetry of the meniscus to solve this problem. In the following sections I develop an accurate numerical solution which does not need such simplification, and also an approximate “semi-analytical” solution for this problem.

## 5.2 Theoretical setting

### 5.2.1 Geometrical considerations

Figure 5.2 shows a pair of spheres floating at a liquid–fluid interface. For the spheres to remain floating, each sphere needs to be in vertical equilibrium. Because of the complicated geometry of the three-phase contact lines, satisfying

the boundary conditions and calculating the forces exerted by the fluids on these spheres is no longer trivial.

For this calculation, we will find it useful to refer to spherical coordinates  $(r, \alpha, \phi)$  centred on the centre of the sphere. The position vector  $\mathbf{P}$  of a point on the surface of the sphere ( $r = R$ ) in relation to the centre of the sphere may then be written:

$$\mathbf{P} = R \sin \phi \cos \alpha \mathbf{e}_x + R \sin \phi \sin \alpha \mathbf{e}_y + R \cos \phi \mathbf{e}_z, \quad (5.6)$$

where  $\mathbf{e}_x$ ,  $\mathbf{e}_y$  and  $\mathbf{e}_z$  are unit vectors in the  $x$ ,  $y$  and  $z$  directions respectively also centred on the centre of the sphere. In these coordinates, the position of the contact line may be written:

$$\phi = \omega(\alpha). \quad (5.7)$$

We can define  $\mathbf{n}$  as the running outward normal to the sphere surface along the contact line,  $\mathbf{t}$  as the running tangent to the contact line, and  $\mathbf{b}$  as the running binormal to  $\mathbf{n}$  and  $\mathbf{t}$  as shown in figure 5.2. Then we have

$$\begin{aligned} \hat{\mathbf{n}} &= \left. \frac{\partial \hat{\mathbf{P}}}{\partial r} \right|_{\phi=\omega} \\ &= \cos \alpha \sin \omega \mathbf{e}_x + \sin \alpha \sin \omega \mathbf{e}_y + \cos \omega \mathbf{e}_z, \end{aligned} \quad (5.8)$$

and

$$\begin{aligned} \hat{\mathbf{t}} &= \frac{d\hat{\mathbf{P}}_c}{d\alpha} \\ &= \frac{1}{\lambda} \left[ \left( \sin \alpha \sin \omega - \cos \alpha \cos \omega \frac{d\omega}{d\alpha} \right) \mathbf{e}_x + \left( \cos \alpha \sin \omega + \sin \alpha \cos \omega \frac{d\omega}{d\alpha} \right) \mathbf{e}_y \right. \\ &\quad \left. + \sin \omega \frac{d\omega}{d\alpha} \mathbf{e}_z \right], \end{aligned} \quad (5.9)$$

where

$$\lambda = \sqrt{\sin^2 \omega + \left( \frac{d\omega}{d\alpha} \right)^2}, \quad (5.10)$$

is the normalization factor and

$$\begin{aligned}\hat{\mathbf{b}} &= \hat{\mathbf{n}} \times \hat{\mathbf{t}} \\ &= \frac{1}{\lambda} \left[ \left( \cos \alpha \sin \omega \cos \omega + \sin \alpha \frac{d\omega}{d\alpha} \right) \mathbf{e}_x + \left( \sin \alpha \sin \omega \cos \omega + \cos \alpha \frac{d\omega}{d\alpha} \right) \mathbf{e}_y \right. \\ &\quad \left. - \sin^2 \omega \mathbf{e}_z \right].\end{aligned}\tag{5.11}$$

As given in Eq. (2.17), the contact angle  $\theta$  is defined in the plane containing  $\mathbf{b}$  and  $\mathbf{n}$  so that  $\hat{\mathbf{b}} \cdot \hat{\boldsymbol{\gamma}} = \cos \theta$ , where  $\hat{\boldsymbol{\gamma}}$  is the unit tangent to the liquid interface in the above plane.

## 5.2.2 Forces acting on a sphere

Using the geometrical information obtained above, we now determine each of the forces acting on the sphere.

### 5.2.2.1 Force due to hydrostatic pressure

We define buoyancy as the net vertical hydrostatic pressure force acting on the sphere. The depth of a point on the surface of the sphere below the undeformed interface is

$$h = -h_c - R \cos \phi,\tag{5.12}$$

where  $h_c$  is the height of the centre of the sphere above the undeformed liquid level i.e.  $h < 0$  when the sphere floats below the liquid level. The hydrostatic pressure on the surface of the sphere relative to the undeformed interface level is

$$p = h\rho_i g,\tag{5.13}$$

where  $i = l, f$  indicates the fluid in contact with the sphere. An elemental area on the surface of the sphere is given in terms of variables  $R$ ,  $\alpha$  and  $\phi$  by

$$dA = R^2 \sin \phi \, d\phi \, d\alpha.\tag{5.14}$$

Then the buoyancy force  $F_{hp}^{(z)}$ , which is the vertical component of the hydrostatic force, is given by

$$F_{hp}^{(z)} = \int -\cos \phi p \, dA. \quad (5.15)$$

Using the equation of the three-phase contact line  $\phi = \omega(\alpha)$  to separate the regions immersed in the two fluids we get

$$F_{hp}^{(z)} = R^2 g \int_0^{2\pi} \left[ \begin{aligned} &\rho_l \int_{\omega(\alpha)}^{\pi} (h_c + R \cos \phi) \sin \phi \cos \phi \, d\phi + \\ &\rho_f \int_0^{\omega(\alpha)} (h_c + R \cos \phi) \sin \phi \cos \phi \, d\phi \end{aligned} \right] d\alpha. \quad (5.16)$$

This gives

$$F_{hp}^{(z)} = \frac{1}{6} R^2 \Delta \rho g \int_0^{2\pi} [2R \cos^3 \omega(\alpha) - 3h_c \sin^2 \omega(\alpha)] \, d\alpha + \frac{4}{3} \pi R^3 \bar{\rho} g, \quad (5.17)$$

where

$$\Delta \rho = \rho_l - \rho_f, \quad (5.18)$$

and

$$\bar{\rho} = \frac{\rho_l + \rho_f}{2}. \quad (5.19)$$

If the contact line is horizontal, i.e.  $\omega$  is independent of  $\alpha$ , the above expression simplifies to

$$F_{hp, \omega}^{(z)} = \frac{1}{3} \pi R^2 \Delta \rho g (2R \cos^3 \omega - 3h_c \sin^2 \omega) + \frac{4}{3} \pi R^3 \bar{\rho} g. \quad (5.20)$$

As well as giving a vertical buoyancy force, the hydrostatic pressure may give rise to a net horizontal force on these partially submerged spheres. This horizontal

component in the  $x$  direction in figure 5.2 is given by

$$\begin{aligned} F_{hp}^{(x)} &= \int h \rho g \sin \phi (-\cos \alpha) dA \\ &= \int \int R^2 \rho g (h_c + R \cos \phi) \sin^2 \phi \cos \alpha \, d\phi \, d\alpha, \end{aligned} \quad (5.21)$$

which yields

$$\begin{aligned} F_{hp}^{(x)} &= R^2 g \int_0^{2\pi} \left[ \rho_l \int_{\omega(\alpha)}^{\pi} (h_c + R \cos \phi) \sin^2 \phi \, d\phi + \right. \\ &\quad \left. \rho_f \int_0^{\omega(\alpha)} (h_c + R \cos \phi) \sin^2 \phi \, d\phi \right] \cos \alpha \, d\alpha. \end{aligned} \quad (5.22)$$

This simplifies to

$$\begin{aligned} F_{hp}^{(x)} &= \frac{1}{6} R^2 g \int_0^{2\pi} \left[ (\rho_l - \rho_f) (3h_c \cos \omega \sin \omega - 2R \sin^3 \omega - \omega) \right. \\ &\quad \left. + 3\pi h_c \rho_l \right] \cos \alpha \, d\alpha. \end{aligned} \quad (5.23)$$

Since the last term of the above equation disappears upon integration, we find that

$$F_{hp}^{(x)} = \frac{1}{6} R^2 \Delta \rho g \int_0^{2\pi} (3h_c \cos \omega \sin \omega - 2R \sin^3 \omega - \omega) \cos \alpha \, d\alpha. \quad (5.24)$$

### 5.2.2.2 Force due to surface tension

The direction of the surface tension force is given by  $\hat{\gamma}$  found in Eq. (2.17). We define

$$\boldsymbol{\gamma} = \gamma \hat{\gamma} \quad (5.25)$$

where the scalar  $\gamma$  is the surface tension of the liquid–fluid interface. Same as in Eq. (3.2), the surface tension force acting on the sphere is given by

$$\mathbf{F}_{st} = \oint \boldsymbol{\gamma} \, ds$$

where  $ds$  is an infinitesimal arc length along the contact line i.e.

$$ds = R\lambda d\alpha, \quad (5.26)$$

with  $\lambda$  given in Eq. (5.10). As shown in Eq. (3.5), we can decompose the vector  $\boldsymbol{\gamma}$  as:

$$\boldsymbol{\gamma} = \gamma(\mathbf{b} \cos \theta + \mathbf{n} \sin \theta).$$

Then using Eq. (5.8) and Eq. (5.11) we obtain the horizontal and vertical components of  $\boldsymbol{\gamma}$ :

$$\boldsymbol{\gamma} \cdot \mathbf{e}_x = \gamma \left[ \frac{1}{\lambda} \left( \cos \alpha \sin \omega \cos \omega + \sin \alpha \frac{d\omega}{d\alpha} \right) \cos \theta + \cos \alpha \sin \omega \sin \theta \right]. \quad (5.27)$$

$$\boldsymbol{\gamma} \cdot \mathbf{e}_z = \gamma \left( -\frac{1}{\lambda} \sin^2 \omega \cos \theta + \cos \omega \sin \theta \right). \quad (5.28)$$

Combining Eq. (5.27) and Eq. (5.28) with Eq. (3.2) and Eq. (5.26) we obtain the vertical component of the force due to surface tension as

$$F_{st}^{(z)} = \gamma R \int_0^{2\pi} (\lambda \cos \omega \sin \theta - \sin^2 \omega \cos \theta) d\alpha, \quad (5.29)$$

and the horizontal component of the force due to surface tension as

$$F_{st}^{(x)} = \gamma R \int_0^{2\pi} \left[ \lambda \cos \alpha \sin \omega \sin \theta + \left( \cos \alpha \sin \omega \cos \omega + \sin \alpha \frac{d\omega}{d\alpha} \right) \cos \theta \right] d\alpha. \quad (5.30)$$

If the contact line is flat, i.e.  $\omega$  is constant, Eq. (5.29) reduces to

$$F_{st, \omega}^{(z)} = 2\pi R\gamma \sin \omega \sin(\theta - \omega), \quad (5.31)$$

which is same as Eq. (5.3) mentioned earlier for an isolated sphere. In addition,

Eq. (5.30) gives that  $F_{st}^{(x)} = 0$  in this case, as should be expected on symmetry grounds.

### 5.2.3 Vertical balance for floating

The net vertical force acting upwards on a sphere at an interface is

$$N = F_{st}^{(z)} + F_{hp}^{(z)} - F_w, \quad (5.32)$$

where  $F_w$  is the weight of the sphere given by

$$F_w = \frac{4}{3}\pi R^3 \rho_s g, \quad (5.33)$$

and  $\rho_s$  is the density of the sphere. Substituting the expressions for  $F_{st}^{(z)}$ ,  $F_{hp}^{(z)}$  and  $F_w$  from Eq. (5.29), Eq. (5.17) and Eq. (5.33) into Eq. (5.32) we find that

$$\begin{aligned} N = & \gamma R \int_0^{2\pi} (\lambda \cos \omega \sin \theta - \sin^2 \omega \cos \theta) d\alpha \\ & + \frac{1}{6} R^2 \Delta \rho g \int_0^{2\pi} (2R \cos^2 \omega - 3h_c \sin^2 \omega) d\alpha \\ & - \frac{4}{3} \pi R^3 (\rho_s - \bar{\rho}) g. \end{aligned} \quad (5.34)$$

For the sphere to float in equilibrium, the vertical forces need to be balanced, i.e.

$$N = 0. \quad (5.35)$$

### 5.2.4 Meniscus profile around the spheres

The height of the liquid–fluid interface is given by  $z = \zeta(x, y)$  which must satisfy the Laplace–Young equation described in Eq. (2.11), and  $z = 0$  represents the unperturbed liquid level.

In consistence with what was introduced in Eq. (3.22), the boundary condition for the meniscus in contact with the surface of a sphere is a fixed contact angle

defined by  $\hat{\mathbf{n}} \cdot \hat{\mathbf{s}} = \cos \theta$ . Here,  $\hat{\mathbf{s}}$ , as given in Eq. (3.23), is the outward unit normal vector to the liquid–fluid interface from a point on the contact line along the plane containing  $\hat{\mathbf{b}}$  and  $\hat{\mathbf{n}}$ . Substituting the expressions for  $\hat{\mathbf{s}}$  and  $\hat{\mathbf{n}}$  from Eq. (3.23) and Eq. (5.8) respectively to this definition of  $\theta$  yields the boundary condition

$$\zeta_x \cos \alpha + \zeta_y \sin \alpha = \frac{\cos \omega - \cos \theta \sqrt{\zeta_x^2 + \zeta_y^2 + 1}}{\sin \omega} \quad (5.36)$$

on the surface of a sphere. The second boundary condition on  $\zeta$  is that

$$\zeta(x, y) \rightarrow 0 \quad (5.37)$$

as  $x, y \rightarrow \infty$ .

Implementing the boundary condition Eq. (5.38) is not straightforward, because  $\omega$  and the location of the boundary are also unknown. This makes it impossible to derive an exact analytical solution for the multiple sphere problem.

### 5.3 Numerical solution of force balance and Laplace–Young equation

For a sphere floating in vertical equilibrium, the force balance Eq. (5.35), the Laplace–Young equation Eq. (2.11) and the boundary condition Eq. (5.38) need to be satisfied simultaneously. Since the boundary condition, horizontal projection of the boundary, and the vertical force all involve  $\omega$  and  $h_c$ , which are unknown, this is a free-boundary problem. As a result, solution of this problem is not trivial and there are no published solutions that satisfy all of the above three conditions. In order to develop approximate solutions, it is often assumed that  $\omega$  is constant (Chan et al., 1981) or  $F_w$  is negligible (Lehle et al., 2008a). I developed an algorithm (Algorithm 1), given schematically on page 94, which numerically solves this problem without making such approximations.

The solution of the Laplace–Young equation is performed on a horizontal plane utilizing the *hp*-meshless cloud method (Liszka et al., 1996) introduced in

---

**Algorithm 1** Solve for a system of floating spheres

---

**Require:**  $E_h > e_{h, \max}$  {This is the difference of  $h_c$  between two consecutive steps of the iteration.}

**Require:**  $E_\omega > e_{\omega, \max}$  {This indicates the difference of  $\omega(\alpha)$  between two consecutive steps of the iteration}

Assume initial values  $h_c$  and  $\omega(\alpha)$

$$h_c^{[1]} \leftarrow h_c$$

$$\omega^{[1]}(\alpha) \leftarrow \omega(\alpha)$$

$$M \leftarrow 0$$

**while**  $E_h > e_{h, \max}$  **or**  $E_\omega > e_{\omega, \max}$  **do**

$$M \leftarrow M + 1$$

Calculate the horizontal projection of boundary:

$$X(\alpha) \leftarrow R \cos \omega^{[M-1]}(\alpha) \cos \alpha,$$

$$Y(\alpha) \leftarrow R \cos \omega^{[M-1]}(\alpha) \sin \alpha.$$

Distribute the nodes on the boundaries and in the domain,

Apply the boundary conditions Eq. (5.38) and Eq. (5.37),

Solve Laplace–Young Equation Eq. (2.11), and

Obtain  $\zeta_m(\alpha)$ . {This is the meniscus height along the boundary.}

Move the sphere vertically (i.e. vary  $h_c$ ) and obtain:

$$\omega(\alpha) \leftarrow \cos^{-1} \left[ \frac{\zeta_m(\alpha) - h_c}{R} \right],$$

$N(h_c, \omega) \leftarrow F_{st}^{(z)}(\omega) + F_{hp}^{(z)}(h_c, \omega) - F_w$ . {This is the net force from Eq. (5.32)}

Find  $h_c$  where  $[N(h_c, \omega)]^2$  is minimized **and**  $\partial N / \partial h_c \leq 0$ :

$$h_c^{[M+1]} \leftarrow h_c,$$

$$\omega^{[M+1]}(\alpha) \leftarrow \omega(\alpha).$$

$N_{res} \leftarrow N(h_c^{[M+1]}, \omega^{[M+1]})$ . {This is the residual net force after the minimization}

Calculate the errors:

$$E_h \leftarrow \max |h_c^{[M+1]} - h_c^{[M]}|.$$

$$E_\omega \leftarrow \max |R [\sin \omega^{[M+1]}(\alpha) - \sin \omega^{[M]}(\alpha)]|.$$

**end while**

---

section 2.3. Since the solution depends on the unknown parameters  $\omega(\alpha)$  and  $h_c$ , we need to determine them in an iterative way. Firstly, initial guesses for  $\omega(\alpha)$  and  $h_c$  are used to find the horizontal projection of the three-phase contact line,  $\{X(\alpha), Y(\alpha)\}$ . Then the nodes for the numerical solution are dispersed on the boundary and in the domain.

For this distribution, the horizontal projection of the three phase contact line around each sphere is fitted to a cubic spline (the radius of this projection  $R_h$  is fitted as a function of  $\alpha$ ). The domain nodes are distributed along curves obtained by adding constant values to  $R_h(\alpha)$ . These curves are clipped along the centre line between the two spheres to avoid overlap. The constants added to  $R_h(\alpha)$  are selected in such a way that the density of nodes gradually decreases from the horizontal projection of the contact lines towards the outer boundary of the domain, because a higher nodal density is desirable near the regions with largest meniscus curvature. The distance from the centre of a sphere to the outer boundary of the domain was always kept above  $7\ell_c$ . This is sufficient to mimic an infinite domain.

The Laplace–Young equation Eq. (2.11) is then solved using the boundary conditions Eq. (5.38) and Eq. (5.37). To handle the nonlinear terms in the Laplace–Young equation, iterative scheme given in Eq. (2.40) was used and for boundary condition Eq. (5.38), the following was used:

$$[\zeta_x \cos \alpha + \zeta_y \sin \alpha]^{[N]} = \frac{\cos \omega - \cos \theta [\sqrt{\zeta_x^2 + \zeta_y^2 + 1}]^{[N-1]}}{\sin \omega}. \quad (5.38)$$

This numerical solution gives the meniscus shape and the meniscus height at the horizontal projection of the three-phase contact line, which is  $\zeta_m(\alpha)$ . Now that we have solved the Laplace–Young equation, we attempt to fulfill the force balance criterion. The sphere is moved vertically up and down and new  $\omega$  is calculated using

$$\omega(\alpha) = \arccos \left[ \frac{\zeta_m(\alpha) - h_c}{R} \right]. \quad (5.39)$$

When the sphere moves vertically,  $h_c$  in the above equation changes and  $\zeta_m(\alpha)$  stays constant. Using  $h_c$  and the resulting  $\omega(\alpha)$ , the net force  $N$  acting on the sphere may be calculated using Eq. (5.34). We then select the value of  $h_c$  which

minimizes  $N^2$ . In some special cases, this minimum value of  $N$  can be zero. Sometimes there are two solutions for  $N = 0$ . Because  $N$  is the net force acting upwards and  $h_c$  is a distance measured in the same direction, only a solution which satisfies

$$\frac{\partial N}{\partial h_c} < 0 \quad (5.40)$$

corresponds to a stable equilibrium of the sphere, in comparison to what was presented by [Rapacchietta and Neumann \(1977\)](#) for an isolated sphere. However, when there are no solutions of  $N = 0$ , we only get

$$\frac{\partial N}{\partial h_c} = 0 \quad (5.41)$$

at minimum  $N$ . In order to force the algorithm to converge on a stable equilibrium wherever possible, we set the general criteria for selecting a value for  $h_c$  to be minimizing  $N^2$  with

$$\frac{\partial N}{\partial h_c} \leq 0. \quad (5.42)$$

$N_{res}$  is the residual value of  $N$  after this minimization. Now using the new  $h_c$  and  $\omega(\alpha)$ , we repeat the iterations until the difference between each of  $h_c$  and  $\omega(\alpha)$  are acceptably small between two consecutive steps. This process is summarized in [Algorithm 1](#).

## 5.4 Semi-analytical solution

[Lo \(1983\)](#) used the method of matched asymptotic expansions to calculate the meniscus height  $\zeta_m$  around a cylinder with  $R \ll \ell_c$  by solving the nonlinear Laplace–Young equation. Here I develop a new approximate solution for multiple spheres by making use of this result.

For a sphere with a horizontal contact line,

$$h_c = \zeta_m - R \cos \omega. \quad (5.43)$$

Now we take advantage of the fact that the meniscus around a sphere with a flat contact line is identical to the meniscus around a vertical cylinder with radius

$R \sin \omega$  and meniscus slope angle  $\psi = \theta - \omega$ . Therefore, combining Eq. (5.43) and Eq. (5.1) with (3.19) from Lo (1983) we obtain the location of the centre of an isolated sphere:

$$h_{c,s}(\omega) \approx -R \cos \omega + R \sin \omega [c_1 \ln \epsilon + c_2 + c_3(\epsilon \ln \epsilon)^2 + c_4 \epsilon^2 \ln \epsilon + c_5 \epsilon^2]. \quad (5.44)$$

where

$$\epsilon = \frac{R \sin \omega}{\ell_c} \ll 1 \quad (5.45)$$

and  $c_1 \dots c_5$  are given by Lo (1983):

$$\begin{aligned} c_1 &= -\sin(\theta - \omega), \\ c_2 &= \sin(\theta - \omega) \left[ \ln 4 - \ln[1 + \cos(\theta - \omega)] - \Gamma \right], \\ c_3 &= \frac{1}{2} \sin(\theta - \omega) [1 + \sin^2(\theta - \omega)], \\ c_4 &= \sin(\theta - \omega) \left[ \cos^2(\theta - \omega) \left( \Gamma + \frac{1}{4} + \ln \frac{1}{4} [1 + \cos(\theta - \omega)] \right) + \frac{1}{4} - \cos(\theta - \omega) \right], \end{aligned} \quad (5.46)$$

$$\begin{aligned} c_5 &= \frac{1}{4} \sin(\theta - \omega) \cos(\theta - \omega) (\ln 4 - \Gamma) - \frac{q}{\cos(\theta - \omega)} + \frac{1}{4} \sin(\theta - \omega) + \\ &+ q(1 - \ln 4 - \Gamma) + \frac{1}{4} \sin^3(\theta - \omega) \left[ \frac{1}{2} - \Gamma^2 - \ln^2 2 + \Gamma \ln 4 - \ln 2 \right] + \\ &+ \ln[1 + \cos(\theta - \omega)] \left( \frac{1}{4} \sin^3(\theta - \omega) \left[ \ln 4 - \Gamma + \frac{1}{\cos(\theta - \omega)} \right] + q + \right. \\ &\left. - \frac{1}{4} \sin(\theta - \omega) \cos(\theta - \omega) \right) + \\ &- \frac{1}{4} \left( \ln[1 + \cos(\theta - \omega)] \right)^2 \sin^3(\theta - \omega), \end{aligned}$$

with

$$q = \frac{1}{4} \sin(\theta - \omega) [1 + \cos^2(\theta - \omega)] \ln [1 + \cos(\theta - \omega)] + \quad (5.47)$$

$$- \frac{1}{2} \sin(\theta - \omega) \cos^2(\theta - \omega) (\ln 4 - \Gamma) - \frac{1}{4} \sin(\theta - \omega) \sqrt{1 - \sin(\theta - \omega)}.$$

(The subscript  $s$  indicates that Eq. (5.44) holds only for a single sphere, i.e. the sphere is isolated.) Here  $\Gamma = 0.5772\dots$  is Euler’s constant. The shape of the meniscus far away from this sphere can be obtained by solving the linearized Laplace–Young equation. This solution is the same as that for a vertical cylinder:

$$\zeta(r, \omega) = -R \sin \omega \sin(\theta - \omega) K_0(r/\ell_c). \quad (5.48)$$

If a second sphere identical to the first one appears at a horizontal distance  $d$  away, it will create a meniscus that moves the first sphere vertically. The spheres will thus have to reach an equilibrium with a new value of  $\omega$ . Assuming the contact lines remain flat we can write the new vertical location of the spheres as:

$$h_c(\omega, d) \approx h_{c,s}(\omega) - R \sin \omega \sin(\theta - \omega) K_0(d/\ell_c). \quad (5.49)$$

For a given value of  $\omega$ , therefore, the problem is fully determined. We must calculate the value of  $\omega$  that gives a zero net vertical force acting on the sphere (i.e.  $N = 0$ ). We calculate  $N$  using Eq. (5.34) with a constant  $\omega$ , with Eq. (5.49) used to eliminate  $h_c(\omega, d)$ . We thus have:

$$N(\omega, d) = 2\pi R \gamma \sin \omega \sin(\theta - \omega) + \quad (5.50)$$

$$+ \frac{1}{3} \pi R^2 g (\rho_l - \rho_f) [2R \cos^2 \omega - 3h_c(\omega, d) \sin^2 \omega] + (\rho_l + \rho_f) 2R +$$

$$- \frac{4}{3} \pi R^3 \rho_s g.$$

Unlike previous work on a single sphere, Eq. (5.50) is an equation for the value of  $\omega$  in equilibrium dependent on the inter-particle distance  $d$ . Therefore, solving Eq. (5.50) for  $N = 0$  gives  $\omega$  as a function of the distance.

We now extend this result to a system of  $M$  identical spheres constrained to reach equilibrium with identical values of  $\omega$ . To check for this condition the

following summation calculated based on a selected sphere  $m$  is used:

$$S_m = \sum_{n=1}^M d_{m,n} \quad (5.51)$$

where  $d_{m,n}$  is the distance from the sphere  $m$  to sphere  $n$ . If

$$S_1 = S_2 = \dots = S_M \quad (5.52)$$

the equilibrium  $\omega$  for all the spheres in the system will be equal. Examples of such arrangements of spheres are spheres spaced on a lattice, or on the vertexes of an equilateral polygon. In such a case, Eq. (5.49) can be modified to

$$h_{c,m}(\omega, d) = h_{c,s,m}(\omega) - R \sin \omega \sin(\theta - \omega) \sum_{n=1}^M K_0(d_{m,n}/\ell_c), \quad (5.53)$$

with  $m$  being any sphere. This expression can be used in Eq. (5.50) as before.

## 5.5 Maximum density of an isolated floating sphere

### 5.5.1 Calculation neglecting buoyancy

As shown in figure 5.1, for a single floating sphere,  $\omega$  is constant as should be expected on grounds of symmetry. Then the vertical component of the surface tension force  $T$  is given by Eq. (5.31). If the weight of the sphere is totally balanced by the surface tension, we can write the force balance combining Eq. (5.32), Eq. (5.31) and Eq. (5.33):

$$N = 2\pi R\gamma \sin \omega \sin(\theta - \omega) - \frac{4}{3}\pi R^3 \rho_w Dg \quad (5.54)$$

where  $\rho_w$  is the density of water and  $D = \rho_s/\rho_w$  is the relative density of the sphere. From Eq. (5.31) we see that  $T$  is maximized when

$$\omega = \theta/2. \quad (5.55)$$

In a solution for the equilibrium of an isolated sphere, [Vella et al. \(2006a\)](#) showed that this result holds when the force of buoyancy is considerably small compared to the surface tension. Substituting this to Eq. (5.54) and setting  $N = 0$  gives the maximum relative density of a sphere that can float with its weight totally balanced by surface tension to be

$$D_{max,T} = \frac{3\gamma \sin^2 \frac{\theta}{2}}{2\rho_w g R^2}. \quad (5.56)$$

If  $D \leq D_{max,T}$ , the sphere floats and if  $D > D_{max,T}$ , the sphere sinks. This equation also shows that surface tension alone can support spheres with very large densities when  $R \ll \ell_c$ . Therefore, in the results where we analyze the behaviour of spheres close to sinking, we use fairly large radii in order to be able to use moderate densities which can correspond to practical conditions.

Another way of determining whether the sphere is sinking or floating at a given  $D$  is numerical minimization of  $|N|$  with respect to  $\omega$  in Eq. (5.54), and determining  $N_{res}$ , which is the residual value of  $|N|$  after the minimization. If  $N_{res}$  is found to be on the order of the machine precision, we conclude that the sphere is floating, while if  $N_{res}$  is several orders of magnitude higher than the machine precision, there is no condition of equilibrium, and the sphere must sink. Figure 5.3(a) compares the values of  $N_{res}$  obtained using this method with  $N_{res}$  obtained using the numerical solution shown in Algorithm 1, also carried out neglecting the buoyancy. The relative densities are normalized by dividing with  $D_{max,T}$  obtained from Eq. (5.56). Since  $N_{res}$  obtained by the numerical solution and numerical minimization of the analytical expression Eq. (5.54) are both discontinuous at the value given by the analytical expression Eq. (5.56), we conclude that checking whether  $N_{res}$  is above or below the machine precision is an effective method of determining whether a sphere is sinking or floating. We shall therefore employ a similar method to understand whether a pair of spheres is floating or sinking.

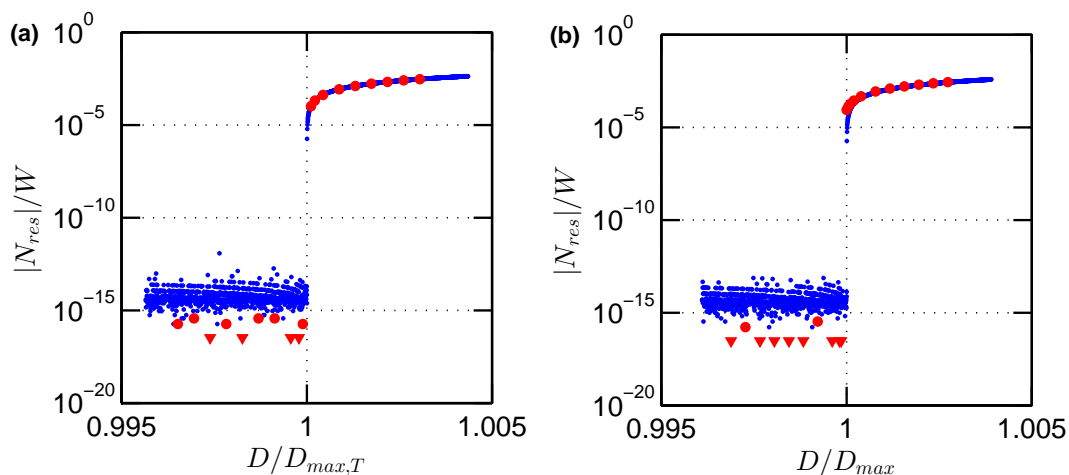


Figure 5.3: Residual net force  $N_{res}$  calculated (a) neglecting buoyancy (section 5.5.1), and (b) considering buoyancy (section 5.5.2) for a sphere with  $R = 0.2209 \ell_c$  m, and  $\theta = 70^\circ$ , at a water-air interface with  $\rho_l = 1000 \text{ kg m}^{-3}$ ,  $\rho_f = 0$ ,  $\gamma = 72.4 \text{ mN m}^{-1}$ ,  $\ell_c = 2.7167 \text{ mm}$ ,  $D_{max,T} = 10.1167$  and  $D_{max} = 11.2839$ . ( $\bullet$ ) and ( $\blacktriangledown$ ) show the numerical solution (Algorithm 1), with ( $\blacktriangledown$ ) representing zero  $N_{res}$ . ( $\cdot$ ) is the numerical minimization of the analytical expressions Eq. (5.54) and Eq. (5.57). When buoyancy is neglected,  $D_{max,T}$  is obtained by analytical optimization Eq. (5.56), and this also matches very well with the values predicted by the numerical solution and numerical minimization of the analytical expression Eq. (5.54). When buoyancy is considered,  $D_{max}$  is obtained by a numerical optimization of the analytical expression Eq. (5.57). This also matches with the numerical solution. However, this is a slight discrepancy here because the result from (Lo, 1983) used in Eq. (5.57) is a truncated asymptotic expression, which loses its accuracy as  $R \rightarrow \ell_c$ . According to Eq. (5.56), spheres with such large radii need to be used in order to achieve sinking at moderate densities.

## 5.5.2 Calculation considering buoyancy

When the force of buoyancy is taken into consideration, in addition to the surface tension and weight, the net force acting on the sphere can be obtained by

combining Eq. (5.32), Eq. (5.20), Eq. (5.31) and Eq. (5.33)

$$\begin{aligned}
 N = & 2\pi R\gamma \sin \omega \sin(\theta - \omega) \\
 & + \frac{1}{3}\pi R^2 g [(\rho_l - \rho_f)(2R \cos^2 \omega - 3h_{c,s}(\omega) \sin^2 \omega) + (\rho_l + \rho_f)2R] \\
 & - \frac{4}{3}\pi R^3 \rho_w Dg,
 \end{aligned} \tag{5.57}$$

with  $h_{c,s}(\omega)$  given by Eq. (5.44). Unlike in section 5.5.1 where buoyancy was neglected, it is not possible to analytically minimize  $|N|$  with respect to  $\omega$  due to the complexity of Eq. (5.57). However, it is of course still possible to numerically minimize  $|N|$ , and evaluate  $N_{res}$  to check whether a sphere is floating or sinking at a given  $D$ . The highest density of a sphere that can float with its weight balanced by both surface tension and buoyancy is defined as  $D_{max}$ . Operationally, this is found as the largest value of  $D$  which gives a  $N_{res}$  on the order of the machine precision. Figure 5.3(b) compares the values of  $N_{res}$  obtained using the numerical minimization of Eq. (5.57) and using the numerical solution Algorithm 1. There is a good match between the results obtained using the two methods, except for the inaccuracies in the result from (Lo, 1983) used in deriving Eq. (5.57) as mentioned in the figure caption.

## 5.6 Vertical equilibrium of a pair of identical spheres

### 5.6.1 Semi-analytical solution

Eq. (5.50) gives an approximate expression for the net vertical force acting on a sphere when it is at a distance  $d$  from an identical sphere. Numerical minimization of  $N$  with respect to  $\omega$  gives  $N_{res}$ . As before, a value of  $N_{res}$  on the order of the machine precision means an equilibrium exists, i.e. the object floats.

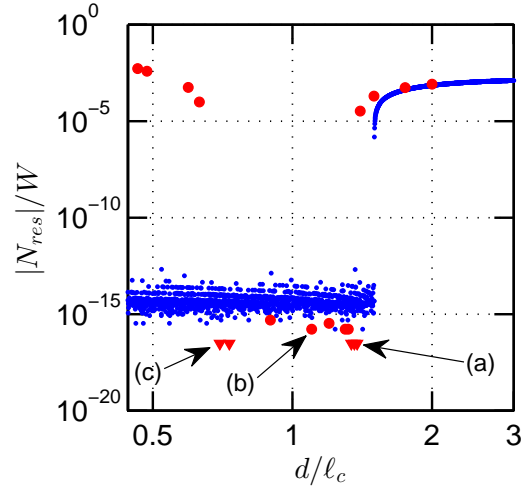


Figure 5.4: The residual net force  $N_{res}$  as a function of the inter-particle distance  $d$  for a pair of spheres with  $R = 0.2209 \ell_c$ ,  $D = 11.3015$  and  $\theta = 70^\circ$ , on a water-air interface with  $\rho_l = 1000 \text{ kg m}^{-3}$ ,  $\rho_f = 0$ ,  $\gamma = 72.4 \text{ mN m}^{-1}$ ,  $\ell_c = 2.7167 \text{ mm}$  and  $D_{max, single} = 11.2839$ . ( $\bullet$ ) and ( $\blacktriangledown$ ) show the numerical solution (Algorithm 1), with ( $\blacktriangledown$ ) representing zero  $N_{res}$ . ( $\bullet$ ) is the semi-analytical solution, which is the numerical minimization of the analytical expressions Eq. (5.50). Meniscus cross sections at the distances labeled with (a), (b) and (c) are plotted in figure 5.5.

### 5.6.2 Numerical solution of two spheres

Algorithm 1 is a general method, and it can be used to accurately solve for the equilibrium position and meniscus for pair of spheres without using any assumptions. As an output, this algorithm also gives  $N_{res}$ .

Figure 5.4 shows the results from the numerical and semi-analytical solutions. We emphasize that these results are for a density slightly larger than that at which an isolated sphere can float ( $D_{max, single}$ ). These spheres sink at far and close range but, surprisingly, they are able to float at intermediate range! Figure 5.5 and figure 5.6 illustrate the reasons behind this behaviour. As the spheres move closer to one another, they move vertically downwards due to the meniscus created by the other sphere. This increases the force of buoyancy acting on each sphere. As shown in figure 5.7(b), the buoyancy acting on the spheres at the intermediate range is larger than the maximum force of buoyancy that an isolated floating sphere can achieve by varying  $\omega$ . This can enable a sphere which would sink

## 5. Floating (and sinking) of spheres at a liquid–fluid interface

---

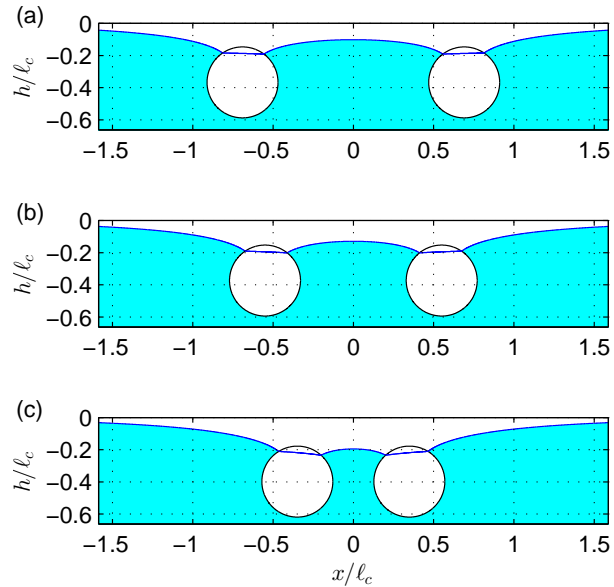


Figure 5.5: Cross sections along the principal axis of the liquid-air interface for the pair of spheres shown in figure 5.4, in the regime where they float. Panels (a), (b) and (c) are for the correspondingly marked locations in figure 5.4. The behaviour is explained in the schematic diagrams in figure 5.6

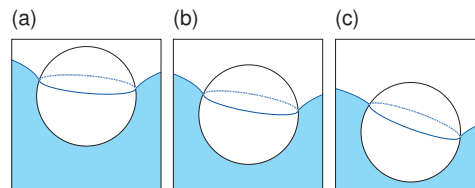


Figure 5.6: As the spheres move closer, their centres move downwards and their contact lines become more tilted. These are schematic diagrams corresponding to the cross sections in figure 5.5 (a), (b) and (c) respectively.

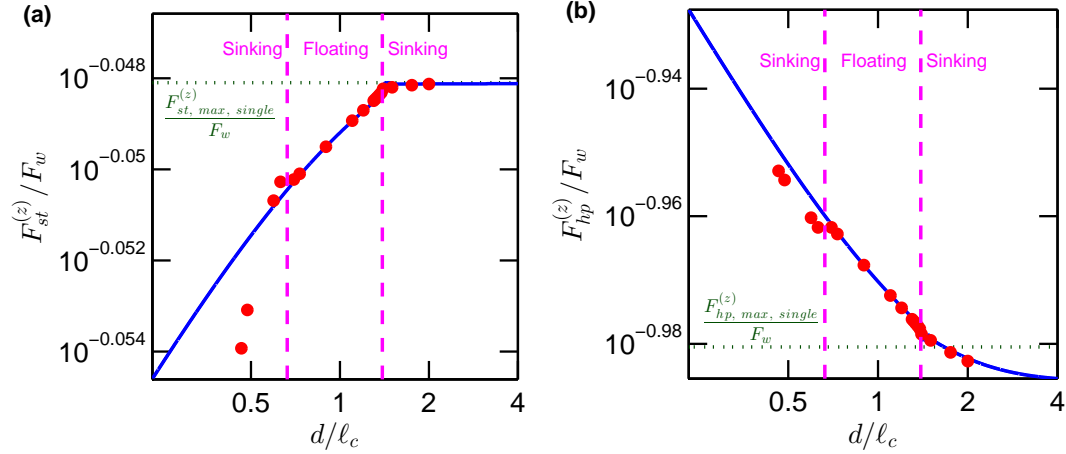


Figure 5.7: Vertical Forces of surface tension (a) and buoyancy (b) acting on each of the spheres in figure 5.4. (•) is the numerical solution and the solid curve is the semi-analytical solution described in section 5.4. The dashed lines separate the regimes of sinking and floating. The dotted lines show the maximum values of vertical surface tension and buoyancy forces that the fluids can exert on an isolated floating sphere (determined by maximization of these forces with respect to the variable  $\omega$ ). As the spheres move close to one another, the force of buoyancy exceeds the maximum for an isolated sphere, while the force of surface tension reduces. The semi-analytical solution predicts the same behaviour as the numerical solution in the region where the sphere floats. Note that the surface tension is always significantly larger than the force of buoyancy.

in isolation to float as part of a pair. This brings new insight to the physics of floating spheres, because such a dependence of the floating and sinking on the inter-particle distance has not been reported previously. We also emphasize that this effect is due to the hydrostatic pressure, which is usually neglected in analyzing capillary interactions.

As shown in figure 5.7, the force of surface tension is significantly larger than the force of buoyancy, and therefore more important for the vertical equilibrium of the sphere. The vertical force of surface tension acting on any infinitesimal length along the contact line is maximized when  $\omega = \theta/2$  see Eq. (5.55). As the spheres move close together, the contact line becomes highly sloped (i.e. the variation of  $\omega$  along the contact line increases) and, as a result, the force of surface tension does not take its maximum value all along the contact line. Figure 5.7(a)

shows that while the surface tension contribution remains high at far range, it drops as the spheres move close to one another. This causes the spheres to sink again at very close range, as observed in figure 5.4. A similar close range sinking effect has been demonstrated for horizontally floating infinite cylinders by Vella et al. (2006b), where the cylinders float only at far range.

Figure 5.8 shows a regime diagram for the sinking and floating behaviours of identical spheres. As mentioned before,  $D_{max, single}$  is the maximum density of an isolated sphere that can float. Our results show that at some densities above  $D_{max, single}$ , a pair of spheres can float. This occurs in an intermediate range of inter-particle distances. The spheres sink at far range due to the relative reduction of the buoyancy force, and at near range due to the excessive tilting of the contact line and resulting reduction of the surface tension force. The results also show that at densities below  $D_{max, single}$  a pair of spheres can sink at close range, again due to the excessive tilting of the contact line as shown in figure 5.6. The maximum density at which the two spheres can remain floating at any inter-particle is smaller than  $D_{max, single}$ .

Using the analytical solution Eq. (5.50), we can maximize  $\rho_s$  having  $\omega$  as the variable keeping  $N(\omega, d)$  within the machine precision. This gives an independent semi-analytical prediction for  $D_{max}(d)$ , which gives an approximation for the long-range sinking behaviour. However, this approximated treatment is unable to predict the short range sinking behaviour because it assumes that the contact line remains flat, whereas this short range sinking is known to be due to the tilting of the contact line.

## 5.7 Vertical equilibrium of a hexagonal lattice of spheres

We now consider an infinite hexagonal lattice of spheres as shown in figure 5.9(a). The numerical solution of this configuration is performed by solving for a single floating sphere using Algorithm 1 in a domain such as the one shown in figure 5.9(b). The boundary condition in the outer boundary of the domain is set

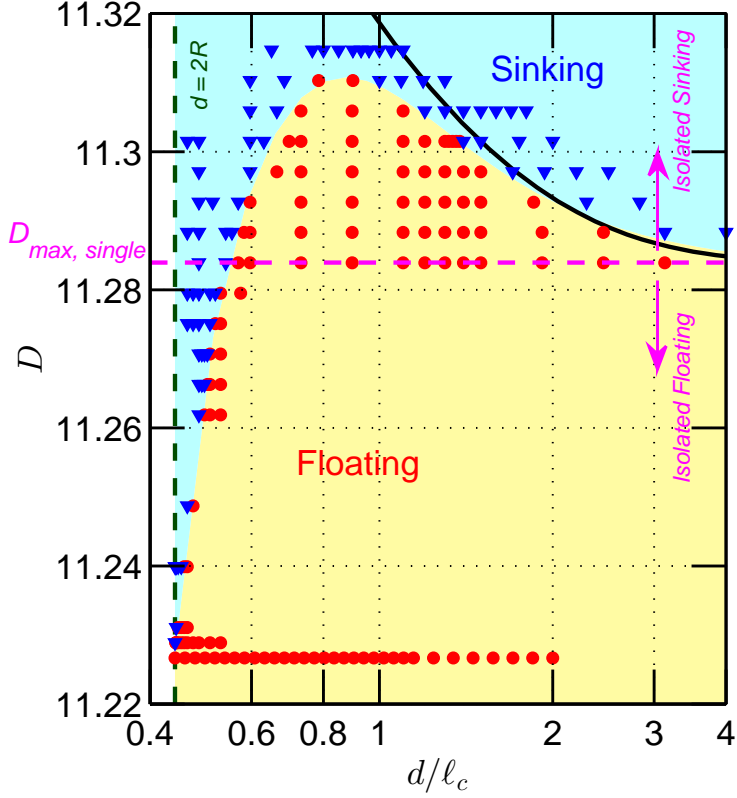


Figure 5.8: Regime diagram showing the sinking and floating behaviour for a pair of spheres with  $R = 0.2209 \ell_c$ , and  $\theta = 70^\circ$ , at a water-air interface with  $\rho_l = 1000 \text{ kg m}^{-3}$ ,  $\rho_f = 0$ ,  $\gamma = 72.4 \text{ mN m}^{-1}$ ,  $\ell_c = 2.7167 \text{ mm}$  and  $D_{max,single} = 11.2839$ . The symbols show the numerical solution (Algorithm 1), with  $(\bullet)$  denoting floating spheres and  $(\blacktriangledown)$  denoting sinking spheres. The solid curve shows  $D_{max}(d)$  as calculated using the semi-analytical solution Eq. (5.50). The numerical solution shows that spheres with densities above  $D_{max,single}$  can float as a part of a pair in an intermediate inter-particle distance range, and even spheres with densities below  $D_{max,single}$  can sink at very close range. The semi-analytical solution correctly predicts the the maximum density as a function of inter-particle distance when the inter-particle distance sufficiently large so that the close-range sinking effect is not significant.

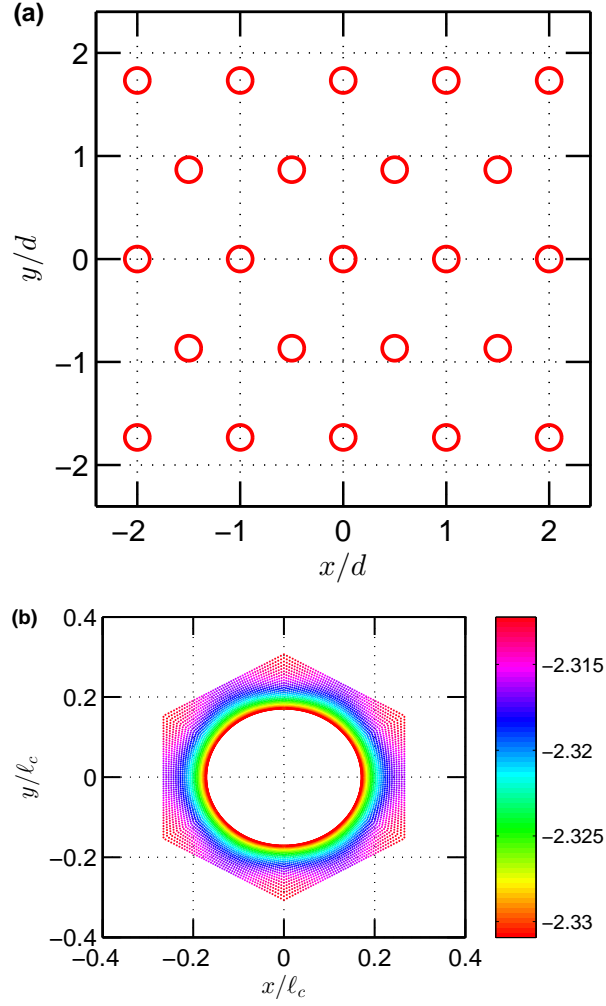


Figure 5.9: (a) Configuration of an infinite hexagonal lattice of spheres. The characteristic inter-particle distance  $d$  is defined as the distance between the centres of two nearest neighbours. (b) Meniscus profile obtained by numerical solution of (a) in a hexagonal domain with the boundary condition Eq. (5.58). The numerical solution was carried out for a hexagonal lattice of spheres  $R = 0.2209 \ell_c$ ,  $\theta = 70^\circ$ ,  $D = 13.4839$  and  $d = 0.5310 \ell_c$  on a water–air interface with  $\rho_l = 1000 \text{ kg m}^{-3}$ ,  $\rho_f = 0$ ,  $\gamma = 72.4 \text{ mN m}^{-1}$  and  $\ell_c = 2.7167 \text{ mm}$ . The dots represent the locations of nodes used for the numerical solution, with the colours denoting  $\zeta/\ell_c$ .

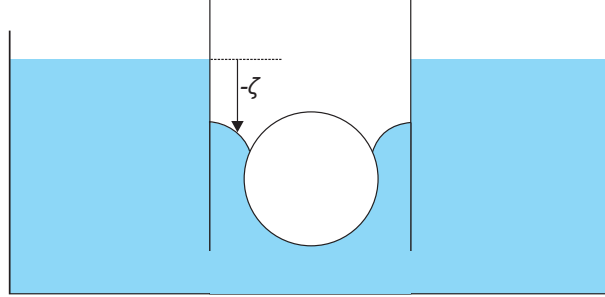


Figure 5.10: The infinite hexagonal lattice of spheres in figure 5.9 is also equivalent to the system shown here. A single sphere is floating in the centre of a vertical tube with a hexagonal cross section made of a material with a contact angle of  $90^\circ$ . The tube is inside an external liquid bath. The interfacial heights are measured relative to the (zero-curvature) liquid level of the bath. As a result all the values of  $\zeta$  in figure 5.9 (b) are negative.

to be

$$\frac{\partial \zeta}{\partial n_b} = 0, \quad (5.58)$$

where  $n_b$  is a distance in the direction normal to the boundary. This system is also experimentally equivalent to a single sphere floating at an interface contained within a vertical tube with a hexagonal cross section made of a material with a contact angle of  $90^\circ$ . The tube is situated in a bath of liquid (see figure 5.10). The pressure in the outer bath can communicate with the tube. The interfacial height  $\zeta$  is thus measured with respect to the surface where the curvature (and hence the pressure difference between the interface) is zero in the external bath.

Figure 5.11 is a regime diagram showing the sinking and floating for the hexagonal lattice of spheres. We observe that spheres with densities above  $D_{max, single}$  may float when the characteristic inter-particle distance  $d$  is not too high. The floating is possible at much higher densities above  $D_{max, single}$  compared to the case of pairs of spheres, because each sphere interacts with a large number of other spheres here.

Unlike the case of a pair of spheres, we do not observe sinking at close range. To understand this observation, recall that for a pair of spheres, the close range sinking is due to the tilting of the contact line to one side. However, in a hexagonal

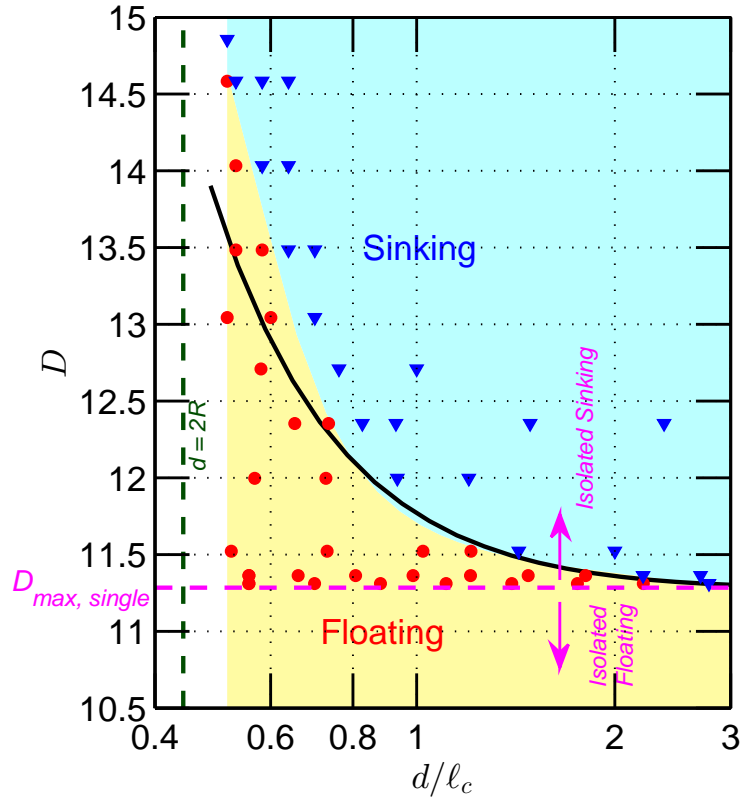


Figure 5.11: Regime diagram showing the sinking and floating behaviour for an infinite hexagonal lattice of spheres with  $R = 0.2209 \ell_c$ , and  $\theta = 70^\circ$ , on a water–air interface with  $\rho_l = 1000 \text{ kg m}^{-3}$ ,  $\rho_f = 0$ ,  $\gamma = 72.4 \text{ mN m}^{-1}$ ,  $\ell_c = 2.7167 \text{ mm}$  and  $D_{max,single} = 11.2839$ . The symbols show the numerical solution (Algorithm 1), with ( $\bullet$ ) denoting floating spheres and ( $\blacktriangledown$ ) denoting sinking spheres. The solid line is  $D_{max}(d)$  calculated using the semi-analytical solution Eq. (5.50). Both the numerical and semi-analytical solutions show that spheres with densities significantly larger than  $D_{max,single}$  can float as the spheres approach close to each other. The accuracy of the semi-analytical solution reduces at very close range.

lattice, each sphere is affected by spheres in every direction, and as a result, there is no overall tilting of the contact line. This is the reason for the absence of a close-range sinking regime.

When  $d$  is very small, the domain used for the numerical solution (figure 5.9b) becomes very small compared to the size of the sphere. As a result, Algorithm 1 fails to converge in this region. This is the reason for the absence of data points at very close range in figure 5.11. However, looking at the trend of the boundary line between the floating and sinking regimes as  $d \rightarrow 0$  we can expect that there will be no close range sinking regime.

Similar to the case of the pair of spheres, we use Eq. (5.50) to develop an analytical solution for  $D_{max}(d)$ , by maximizing  $\rho_s$  keeping  $N(\omega, d)$  within the machine precision. Here, for the calculation of  $h_c$ , Eq. (5.53) is used with a large  $M$  so that the meniscus height resulting from the sphere located farthest away is on the order of machine precision. As shown by the solid curve in figure 5.11, this solution is able to predict the boundary between the floating and sinking regimes fairly well. However, when the characteristic distance between the spheres is very small, this solution becomes less accurate compared to the numerical solution because the approximation of linear superposition of meniscii and the long-range asymptotic solution of the meniscus used in deriving Eq. (5.50) both fail in this range.

## 5.8 Concluding remarks on the floating and sinking of spheres

A numerical solution was developed utilizing a new algorithm which accurately solves for the equilibrium of multiple floating spheres. An independent semi-analytical solution which successfully approximates the results of the numerical solution was also developed. For the first time, we showed that the floating and sinking of spheres can also depend on the distances among them. For a pair of spheres, there is a limited range of intermediate distances in which they float even if their density is above the maximum density of a single sphere that can float ( $D_{max, single}$ ). Moreover, we found that even at densities below  $D_{max, single}$ ,

## 5. Floating (and sinking) of spheres at a liquid–fluid interface

---

the spheres can sink at very close range, replicating an observation made for cylinders by [Vella et al. \(2006b\)](#). For a hexagonal lattice of spheres, we show that the effect of floating above  $D_{max, single}$  is even more significant while the effect of sinking below  $D_{max, single}$  is absent.

## Chapter 6

# The capillary attraction between pairs of floating particles

In this chapter, I use the method of numerical solution presented in the previous chapter to calculate the force of attraction between a pair of floating spheres. The capillary forces are also determined experimentally here.

There have been earlier experimental studies on this problem by [Dalbe et al. \(2011\)](#); [Vassileva et al. \(2005\)](#). These studies involved placing pairs of spherical particles at liquid–fluid interfaces, and (by means of particle tracking) measuring their relative velocities. The results were then fitted using combined asymptotic expressions for the force of capillary attraction and hydrodynamic drag at low Reynolds numbers. Their results are reproduced in figure 6.1. While the results in figure 6.1 (a) agree with the asymptotic predictions, the results in figure 6.1 (b) deviate at far range. Since the asymptotic expressions are expected to be more accurate at far range compared to close range, it would be more appropriate to fit only using the far–range data. Our experimental data presented in this chapter is fitted in this way, and hence shows good agreement at far–range. For some types of particles, we observe clear deviations at close range, which seem to imply a deficiency in the description of either the hydrodynamic drag, or the capillary attraction force. We also extend our experiments for non–spherical particles.

The expressions for both hydrodynamic interaction and capillary interaction used for the fitting are based on several simplifying assumptions. In contrast, our

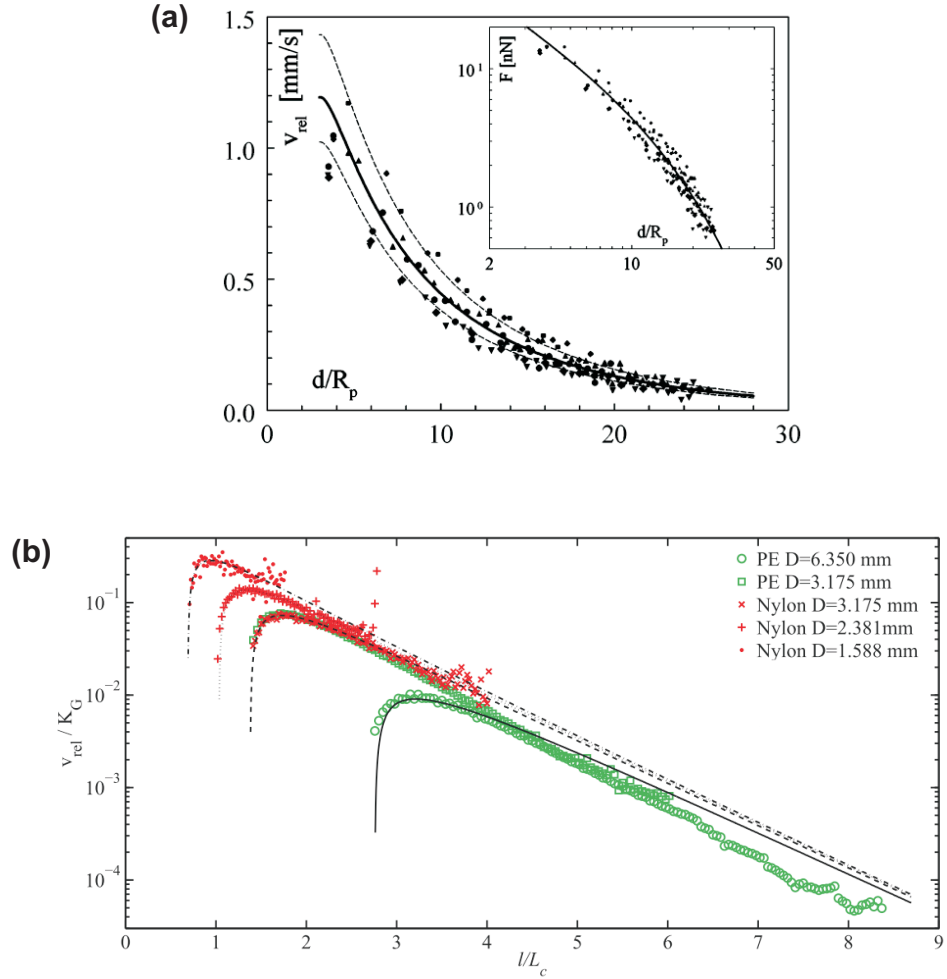


Figure 6.1: Experimental results on capillary interaction between floating spheres reprinted from (a) [Vassileva et al. \(2005\)](#) and (b) [Dalbe et al. \(2011\)](#). The relative velocities  $v_{rel}$  of different particles at liquid–fluid interfaces are plotted as a function of the inter–particle distance. In (a),  $d$  is the inter–particle distance,  $R_p$  is the radius of a particle, and in (b),  $l$  is the inter–particle distance,  $L_c$  is the capillary length, and  $K_G$  is same as the constant  $C_F$ , which will be introduced later in this chapter (Eq. 6.8). (a) also includes an inset showing the force of capillary attraction  $F$ . The symbols show experimental results, and solid curves show results of fitting this data to asymptotic predictions. Results in (a) agree with the asymptotic solution, whereas the results in (b) deviate at large inter–particle distances.

numerical solution gives an accurate solution for the force of capillary attraction. We use this solution to suggest possible reasons for the discrepancy between the experimental data and the asymptotic predictions.

## 6.1 Asymptotic results for flotation interactions

An asymptotic prediction for the force of capillary attraction between a pair of identical floating spheres has been derived by [Chan et al. \(1981\)](#), assuming small meniscus slopes and linear superposition of the menisci:

$$F = 2\pi\gamma R B^{5/2} \Sigma^2 K_1(d/\ell_c). \quad (6.1)$$

Here  $B$  is the ‘‘Bond number’’ given by

$$B = \frac{R^2}{\ell_c^2}, \quad (6.2)$$

and

$$\Sigma = \frac{2(\rho_s - \rho_l)}{3(\rho_f - \rho_l)} - \frac{1}{3} - \frac{1}{2}\cos\theta + \frac{1}{6}\cos^3\theta. \quad (6.3)$$

In addition to this capillary force two floating spheres moving relative to each other also interact hydrodynamically. Balancing the attractive capillary force with the hydrodynamic drag, the relative velocity of a pair of particles ([Dalbe et al., 2011](#); [Vassileva et al., 2005](#)) gives:

$$v = C_H G(r) F(d) \quad (6.4)$$

where  $r = d/R$ ,  $G(r)$  is the hydrodynamic mobility ([Batchelor, 1976](#)), and  $C_H$  is a constant that depends on the geometry of the sphere and viscosity of the liquid, and which also accounts for the fact that the sphere is at the interface rather than in the bulk. By interpolating values tabulated by [Batchelor \(1976\)](#) for small Reynolds numbers and small capillary numbers, [Dalbe et al. \(2011\)](#) gave a formula for the hydrodynamic mobility:

$$G(r) = 1 - \frac{3}{2r} + \frac{1}{r^3} - \frac{15}{4r^4} - \frac{4.46}{1000(r - 1.7)^{-2.867}}, \quad (6.5)$$

where  $r$  is the distance between the particles divided by the particle radius  $R$ . It should be emphasized that this formula is only strictly valid if the sphere is totally immersed in the bulk liquid; having it partially submerged gives rise to an error. (There is no analytical expression for the fluid flow around solid objects at the interface of fluids with different viscosity.)

## 6.2 Experiments on the behaviour of floating spheres

### 6.2.1 Determination of the contact angle

A spherical particle made of Teflon (relative density  $D = 2.2$ ) with a nominal diameter of 1/16 in (i.e. radius of 794  $\mu\text{m}$ ), from Bal-tec Inc., USA (product number: 14032) was used in this experiment. The particle was placed on the surface of a 50 vol% glycerol–water solution with density  $\rho_l = 1126 \text{ kg m}^{-3}$ , surface tension  $\gamma = 68.0 \text{ mN m}^{-1}$ , and capillary length  $\ell_c = 2.48 \text{ mm}$ . The fluorescent dye Rhodamine was added to the liquid. The use of glycerol reduced the movement of the particle due to environmental effects. Using a Leica DM600B fluorescence confocal microscope, images of a single particle were recorded in a series of horizontal planes ( $z$  stack). At each plane, a fluorescence image and a bright field image were recorded simultaneously, at a resolution of  $512 \times 512$  pixels. The vertical gap between two consecutive imaging planes in the  $z$ -stacks was 6.18  $\mu\text{m}$ . These images allowed for the contact angle to be measured.

Figure 5.1 schematically shows the floating particle and introduces the symbols used in the calculations in this section. Figure 6.2 shows the fluorescence images taken at two horizontal planes intersecting the particle. The regions with the presence of the liquid is bright because of the fluorescent dye, and the areas occupied by the particle and air is dark. In figure 6.2 (a), the imaging plane is totally beneath the liquid surface. The boundary of the particle on the imaging plane is a circle. The centre  $C_s$  of this circle is obtained using the higher-contrast bright field image obtained alongside the fluorescence image. Using this centre  $C_s$ , a circle is drawn to match the particle–liquid boundary in the fluorescence

image by selecting the largest circle for which the mean brightness of the pixels along the perimeter does not exceed a specified threshold  $t_c$ . This circle is shown in white in the image. The imaging plane in Figure 6.2 (b) has a region of air, and as a result, the fitted circle is outside the spherical particle.

The radii of these circles are then plotted in figure 6.3. A circle is fitted to the data shown in the figure in order to determine the centre of the sphere. Only the high-contrast images are selected for this fitting, as shown by the solid line. (Towards the bottom of the sphere, the slope of the surface of the sphere reduces, and as a result, the contrast of the fluorescent images also reduces). This gave the radius of the sphere to be  $818 \pm 2\mu\text{m}$ . The radii of the horizontal circles start to deviate from the radii of the cross sections of the sphere once it meets the liquid meniscus. It was observed that the location where this deviation occurs does not significantly depend on the value of the threshold  $t_c$  used in selecting the white circles shown in figure 6.2, as long as it properly captured the boundary of the sphere in the imaging planes that are totally beneath the liquid surface. Using this location of the deviation, and the centre of the sphere,  $\omega$  was calculated to be  $98.6 \pm 0.1^\circ$ .  $h_c$  was also obtained from this graph by measuring the vertical position of the centre of the sphere relative to the vertical position of the lowest imaging plane where the fitted circle is fully away from the fluorescence image.

According to the vertical force balance on the sphere,

$$F_{hp, \omega}^{(z)} + F_{st, \omega}^{(z)} = F_w, \quad (6.6)$$

where  $F_{hp, \omega}^{(z)}$ ,  $F_{st, \omega}^{(z)}$  and  $F_w$  are given in Eq. (5.31), Eq. (5.20) and Eq. (5.33) respectively. Solution of Eq. (6.6) using  $\omega$ ,  $h_c$  and  $R$  obtained as described above, gives  $\theta = 103.0 \pm 0.1^\circ$ .

## 6.2.2 Experiments on velocities of attraction

### 6.2.2.1 Materials and methods

The experiments are carried out using particles floating at a liquid–air interface. The liquid, a solution of 50% (by volume) glycerol solution (the same as that used in section 6.2.1, without the fluorescence dye), was contained in a petri dish

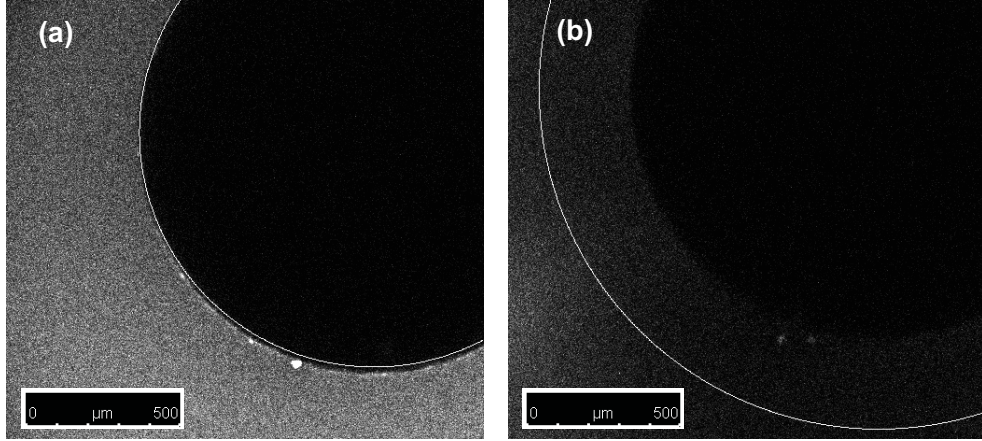


Figure 6.2: Fluorescence confocal microscopy images of the meniscus around a spherical Teflon particle floating at the interface of a 50 vol % glycerol–water solution and air, recorded in two horizontal planes. (Such a particle is schematically shown in figure 5.1). The fluorescence dye Rhodamine is added to the liquid. In (a), the imaging plane is totally beneath the liquid surface, with  $z = -272 \mu\text{m}$ , and in (b), the imaging plane intersects the meniscus, with  $z = -68 \mu\text{m}$ , where  $z$  is the height measured from a location of negligible meniscus deformation. The centre  $C_s$  of the cross section of the sphere at each imaging plane is obtained using separate bright field images. The largest circle that is centred on  $C_s$ , and of which the average brightness of pixels along the perimeter does not exceed a threshold  $t_c$  is then determined for each image. This is shown in white. When the imaging plane is totally under the liquid, this circle coincides with the boundary of the cross section of the sphere. When the imaging plane intersects the meniscus, the circle deviates away from the sphere.

with diameter 14 cm. The presence of glycerol reduced the Reynolds number, enhancing the applicability of Eq. (6.5) to the experimental system. Two types of spherical particle types are used in the experiment: the Teflon spheres described in section 6.2.1 and Chrome steel ( $D = 7.8$ ) spheres with nominal diameter 0.010086 in (i.e. radius  $128 \mu\text{m}$ ) from Bal-tec, USA (product number: 48521), along with non-spherical particles: Sodium Chloride crystals with approximate diameter 4 mm and  $D = 2.2$  and “Science Museum Hydrophobic Sand” from London Science Museum with irregular shape, approximate radius  $360 \mu\text{m}$  and  $D = 1.5$ . Pairs of particles of the same type are carefully placed on the liquid surface, and images are recorded at constant time intervals. For the chrome steel

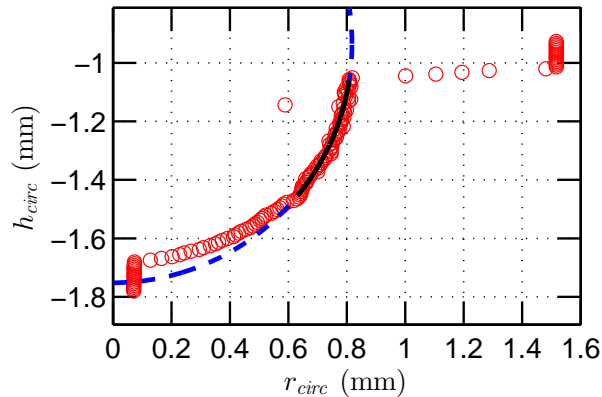


Figure 6.3: ( $\circ$ ) shows the radii of the circles in the horizontal confocal sections ( $z$  stacks) such as those in figure 6.2, for a Teflon sphere floating on a 50 vol % glycerol–water solution. A circle is fitted to the data range denoted by the solid curve to determine the radius and the centre of the spherical particle. The resulting circle is shown by the dashed curve. This enables the calculation of  $\omega$  and  $h_c$ .

particles, a Zeiss Axioplan II microscope with a magnification of 2.5 is used with a CCD camera (Allied Vision Technologies Stingray F-033, resolution  $1040 \times 1388$  pixels). Since all other particles are sufficiently large, the same CCD camera is used with a photographic lens (Micro–Nikkor 105 mm from Nikon).

These experiments on the movement of particles were carried out by Peter Saunders, Part III student in the Department of Physics, University of Cambridge.

### 6.2.2.2 Image analysis, particle tracking and velocity calculation

The images are analysed using Matlab. Particles are differentiated from the background by selecting pixels above a threshold brightness. Two methods are used to remove noise: requiring the area of each particle to be higher than a threshold value, and requiring the brightness of the brightest pixel within a particle to be above a threshold. The movement of the particles is tracked by connecting each particle in one image to the particle in the next image that is located closest to the position of the particle in the original image. Then using the details of the frame rate used, the relative velocities of the particles are calculated. Figure 6.4

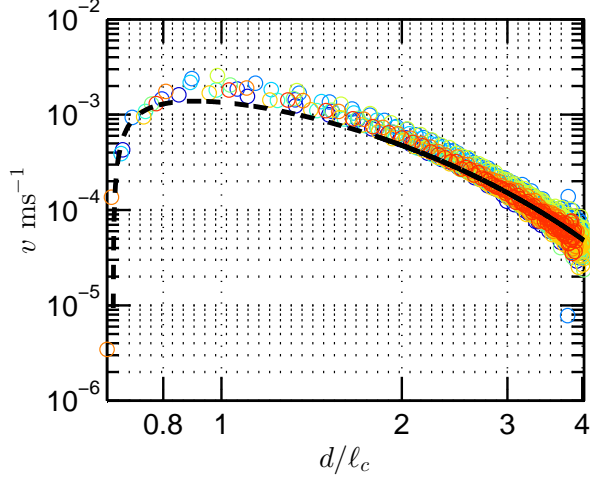


Figure 6.4: Experimental results for the relative velocities of a pair of spherical particles at a liquid interface. The liquid is a 50 vol% glycerol solution with density  $\rho_l = 1126 \text{ kg m}^{-3}$ , surface tension  $\gamma = 68.0 \text{ mN m}^{-1}$ , capillary length  $\ell_c = 2.48 \text{ mm}$  and viscosity  $\mu = 6 \text{ mPa S}$ . The particles are Teflon spheres with relative density  $D = 2.2$ , radius  $R = 0.33 \ell_c$  and contact angle  $\theta = 103^\circ$ . Symbols with different colours are different trials of the same experiment. The black curve is a fit using Eq. (6.7) carried out treating results from all the trials as a single data set. The solid part of this curve shows the data range used for the fitting, and the dashed part is the prediction from the fitted expression.

shows the relative velocities of pairs of Teflon spheres calculated this way.

To analyse this data, we combine Eq. (6.4) and Eq. (6.1) to find

$$v = C_F G(r) K_1(d/\ell_c), \quad (6.7)$$

where  $C_F$  is a constant given by

$$C_F = 2\pi\gamma R B^{5/2} \Sigma^2 C_H, \quad (6.8)$$

and  $C_H$  is another constant that was introduced Eq. (6.4). Using Eq. (6.7), the velocity data shown in figure 6.4 were fitted by adjusting the parameter  $C_F$ . The figure shows that Eq. (6.7) is a good approximation at large inter-particle separations. However, the velocities deviate from the the predicted values at small distances. Because we expect the attractive capillary force predicted by

Eq. (6.1) to be more accurate at far-range, and also since the Reynolds numbers and capillary numbers in this range are smaller, the fitting was carried out only using data in far-range, which is shown by the solid curve. For the pair of interacting particles, the Reynolds number is given by

$$\text{Re} = \frac{v R \rho_l}{\mu}, \quad (6.9)$$

where  $\mu$  is the dynamic viscosity of the liquid. The capillary number is defined as

$$\text{Ca} = \frac{\mu v}{\gamma}, \quad (6.10)$$

In the results shown in figure 6.4, the maximum Reynolds number within the data range that was used for the fitting is 0.09 and the maximum capillary number in this range is  $5.1 \times 10^{-5}$ . The Reynolds number corresponding to the maximum velocity in the whole data set is 0.40, and the corresponding capillary number is  $2.3 \times 10^{-4}$ . This increase of the Reynolds number and the capillary number at close range can reduce the accuracy of Eq. (6.5).

The fitting yields the constant  $C_F = 0.0045$ . Using this value on Eq. (6.8), along with the contact angle determined in section 6.2.1, we obtain  $C_H = 2145$ .

### 6.2.3 Experimental determination of the force of capillary interaction

By combining Eq. (6.4) and Eq. (6.8) we obtain

$$\frac{F}{\gamma R B^{5/2} \Sigma^2} = \frac{2\pi v}{C_F G(r)}. \quad (6.11)$$

The left side of this equation is the dimensionless force of capillary attraction. The fitting of the velocity data was carried out for different particles and the value of  $C_F$  was determined for each of them using the method described in the previous section. Then using Eq. (6.11), the force of capillary interaction was calculated up to short range. Figure 6.5 compares the results with the asymptotic expression for the capillary force Eq. (6.1), for particles made with different materials, sizes and shapes.

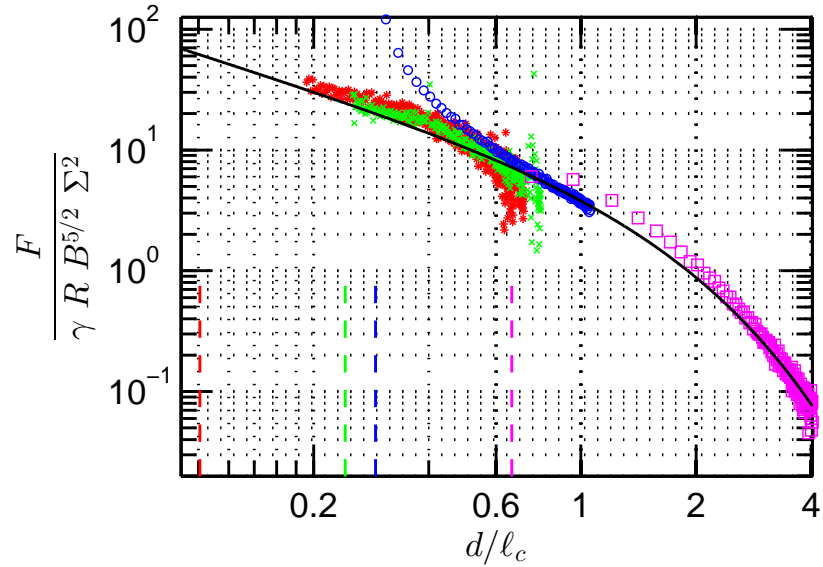


Figure 6.5: Forces of capillary attraction between different particles at a liquid–air interface, where the liquid is a 50 vol% glycerol solution with  $\rho_l = 1126 \text{ kg m}^{-3}$ ,  $\gamma = 68.0 \text{ mN m}^{-1}$ ,  $\ell_c = 2.48 \text{ mm}$ . The forces are calculated using Eq. (6.11), for which the parameter  $C_F$  was determined for each type of particle by fitting the velocity data using the method described in section 6.2.2.2. Symbols show different types of particles: chrome steel spheres with  $R = 0.1 \ell_c$  and  $D = 7.8$  ( $\bullet$ ), sodium chloride crystals with  $R \approx 0.16 \ell_c$  and  $D = 2.2$  ( $*$ ), rough hydrophobic sand with  $R \approx 0.12 \ell_c$  and  $D = 1.5$  ( $\circ$ ), Teflon spheres with  $R = 0.33 \ell_c$  and  $D = 2.2$  ( $\square$ ). The solid curve is the asymptotic solution (Eq. 6.1) for the force of attraction between a pair of spheres. The vertical dashed lines show the centre-to-centre distance where the particles would touch. i.e.  $d = 2R$ . The results show that Eq. (6.11) obtained using the asymptotic result for capillary attraction and the hydrodynamic interaction is accurate at large inter-particle separations even for non-spherical particles. However, at small separations, some particles show deviations from this prediction.

### 6.3. Numerical determination of the attraction between floating spheres

---

Particle type-	$Re_{\max, \text{ all}}$	$Re_{\max, \text{ fitting}}$	$Ca_{\max, \text{ all}}$	$Ca_{\max, \text{ fitting}}$
Teflon spheres	0.26	0.05	$1.5 \times 10^{-4}$	$2.7 \times 10^{-5}$
Steel spheres	$3.1 \times 10^{-3}$	$3.1 \times 10^{-3}$	$1.2 \times 10^{-5}$	$1.2 \times 10^{-5}$
Hydrophobic sand	0.13	0.03	$1.7 \times 10^{-4}$	$3.4 \times 10^{-5}$
NaCl crystals	$2.4 \times 10^{-3}$	$2.4 \times 10^{-3}$	$3.1 \times 10^{-6}$	$3.1 \times 10^{-6}$

Table 6.1: Maximum Reynolds numbers and capillary numbers of the data sets plotted in figure 6.5.  $Re_{\max, \text{ all}}$  and  $Ca_{\max, \text{ all}}$  are respectively the maximum Reynolds number and the maximum capillary number in the whole data set.  $Re_{\max, \text{ fitting}}$  and  $Ca_{\max, \text{ fitting}}$  are respectively maximum Reynolds number and the maximum capillary number in the data used for the fitting. For Teflon spheres and hydrophobic sand, only a subset of long-range data was used for the fitting.

The figure shows that when a pair of particles are sufficiently far apart, the hydrodynamic interaction predicted by Eq. (6.4) and the capillary attraction predicted by Eq. (6.1) can explain their overall interaction with a good accuracy. The results show that this is true even for non-spherical particles. At small inter-particle separations, deviations from these predictions can be observed for the Teflon spheres and hydrophobic sand. Table 6.1 gives the maximum Reynolds numbers for each experiment, and shows that the particles showing deviations from the asymptotic expressions have high Reynolds numbers. However, with these results alone, it is not possible to conclude whether it is the expression for the hydrodynamic interaction or the capillary interaction or the both that gives rise to these errors. As mentioned earlier, both these expressions involve simplifications which may give rise to errors at small distance ranges. In order to find out the real reason for the errors, we carry out an accurate numerical solution to determine the force of capillary attraction, by solving the nonlinear Laplace–Young equation.

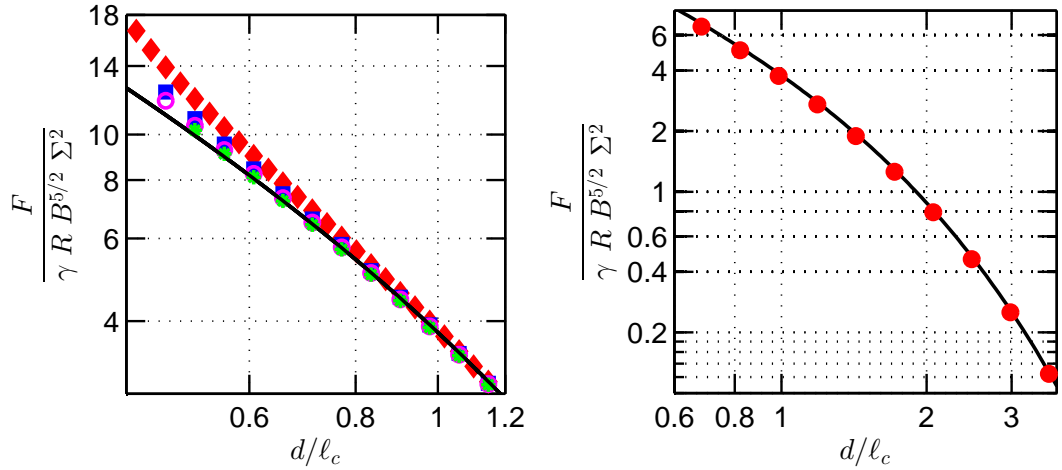


Figure 6.6: (a) shows the force of capillary attraction between a pair of spheres floating at a water–air interface with  $\rho_l = 1000 \text{ kg m}^{-3}$ ,  $\rho_f = 0$ ,  $\gamma = 72.4 \text{ mN m}^{-1}$ ,  $\ell_c = 2.7167 \text{ mm}$ . The spheres have  $R = 0.2209 \ell_c$ , and  $\theta = 70^\circ$ . As calculated in section 5.5.2,  $D_{max, single} = 11.2839$ . Symbols show spheres with different relative densities:  $D = 11.2267$  ( $\blacklozenge$  – This is the maximum density of a pair of spheres that can remain floating until they touch, as shown in the data set with lowest density in the regime diagram figure 5.8),  $D = 8.0000$  ( $\blacksquare$ ),  $D = 5.6419$  ( $\circ$ ),  $D = 3.3852$  ( $*$ ). The solid curve is the asymptotic solution Eq. (6.1). When the density of the sphere is close to  $D_{max, single}$ , there are significant deviations from the asymptotic solutions for close range. However, as the density reduces, this deviation becomes smaller. (b) shows the numerical solution for the force of attraction between a pair of spheres similar to the Teflon spheres used in the experiment. All parameters of the particles and the liquid are same as those in the experiment, except the contact angle, which is used as  $135^\circ$  in the numerical solution. The symbols are the numerical solution, and the solid curve is the asymptotic solution. Figure shows that in this range of parameters, the asymptotic solution is accurate even at very small inter-particle separations.

## 6.3 Numerical determination of the attraction between floating spheres

The numerical solution in Chapter 5 gives the equilibrium meniscus profile around a pair of floating spheres. Using this solution, and integration along the contact line we can calculate the horizontal capillary forces acting on a sphere. The total horizontal force is given by

$$F_x = F_{hp}^{(x)} + F_{st}^{(x)}, \quad (6.12)$$

where  $F_{hp}^{(x)}$  and  $F_{st}^{(x)}$  are the forces resulting from hydrostatic pressure and surface tension, given by Eq. (5.24) and Eq. (5.30), respectively.

Figure 6.6 (a) shows the numerical solution for the force of attraction between pairs of floating spherical particles with different densities. When the density of the sphere approaches the maximum density of a floating sphere ( $D_{max, single}$ ), the meniscus slope around it increases, generating a larger surface tension force. When two such spheres move close to each other, the meniscus slopes further increase due to their collective behavior. As a result, the assumption of small meniscus slopes used in deriving the asymptotic solution Eq. (6.1) becomes invalid. Therefore, the force of attraction predicted by the numerical solution, which does not use any such approximation, deviates from the asymptotic prediction.

This effect becomes less and less significant for lower sphere densities, where they can be supported without the meniscus slope becoming large, even at close range. As shown in figure 6.6 (b), in the range of parameters used in the experiment for the Teflon spheres, the force of attraction does not deviate from the asymptotic prediction even at close range.

This shows that Eq. (6.1) gives an accurate prediction for the force of attraction between the Teflon spheres, and the deviation in figure 6.5 for these particles must be due some other effect, most likely the inaccuracy of the expression for the hydrodynamic interaction.

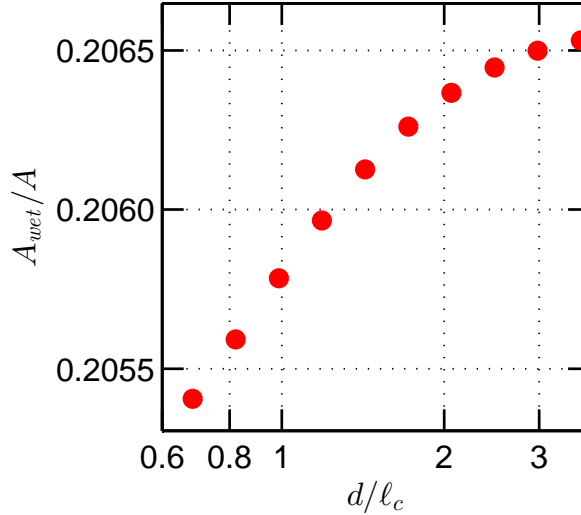


Figure 6.7: Numerical solution for the interaction between an identical pair of spheres similar to the Teflon spheres used in the experiment. The figure shows the ratio between the total area ( $A$ ) of a sphere and the area wetted by the liquid ( $A_{wet}$ ). All parameters of the particles and the liquid are same as those in the experiment, except for the contact angle which is used as  $135^\circ$  in the numerical solution. The relative change in the extent of immersion of the spheres during their movement is very small.

## 6.4 Limitations of the expression for the hydrodynamic interaction

In this section, I present the possible causes that limit the validity of Eq. 6.4, thereby resulting in a discrepancy between some experimental results and the asymptotic prediction in figure 6.5. One inaccuracy of this expression can arise as a result of the parameter  $C_H$  not being constant as the particles move towards each other because the volume of a particle submerged in the liquid will depend on the inter-particle distance. Although this change could not be measured experimentally, the numerical solution was used to determine how the extent of immersion of the particles changed as they approached one another. Figure 6.7 shows the ratio between the total area and wetted area of a pair of spheres similar to the Teflon spheres used in the experiment as a function of their inter-particle distance. It is evident that the relative change in this ratio is very small, and as

a result, we do not expect this to have a significant effect on the hydrodynamic interaction.

Derivation of Eq. 6.4 also assumes the inertial force to be negligible. (This force is given by  $-m\ddot{d}$ , where  $m$  is the mass of a particle and  $-\ddot{d}$  the acceleration as it approaches another particle.) The validity of this assumption was checked by evaluating the ratio between the inertial force ( $F_i$ ) and the capillary force of attraction ( $F$ , from Eq. 6.1) using the experimental data. For the Teflon spheres, the maximum value of this ratio was found to be  $(|F_i|/F)_{max} = 0.01$ . This evaluation could not be carried out for other types of particles because their contact angles were unknown. However, the above result suggests neglecting the inertial force is a reasonable simplification.

As shown in table 6.1, the Reynolds numbers (Re) and capillary numbers (Ca) increase as the inter-particle distance reduces. This also can result in errors in the prediction of the hydrodynamic interaction which is only valid for small values of Re and Ca. However, we note that the relative increases in Re and Ca observed in the experiments are still small.

The movement of the particle on the liquid surface also causes a surrounding curved meniscus region to travel together with it. This can result in an increased hydrodynamic resistance (Petkov et al., 1995), and a change in the hydrodynamic interaction between the two spheres. The numerical solution for the spheres similar to the Teflon particles used in the experiment showed that the maximum deformation of the liquid surface when the particles are touching each other was equal to  $0.11 \ell_c$ . Although the meniscus slopes were not large enough for the nonlinear terms of the Laplace–Young equation to have a significant effect, the meniscus deformations were themselves large, possibly affecting the hydrodynamic interaction.

Because of the drag force acting on the lower part of the spherical particles, they can have a rolling motion. The rough particles can also undergo tilting and rotation as they move towards each other. These effects can complicate their behaviour. We also note that Eq. 6.4 is strictly valid for spheres, and the non-spherical geometry of the hydrophobic sand can affect its accuracy, especially at close-range.

## 6.5 Concluding remarks on attraction between floating particles

By means of particle tracking, the relative velocities of particles at a liquid–air interface are determined. This data can be explained with sufficient accuracy at large inter-particle distances using a combination of two expressions: the asymptotic solution for capillary attraction between floating spheres (Eq. 6.1) and hydrodynamic mobility (Eq. 6.4), even for non–spherical particles. However, at short range, these predictions fail for some types of particles.

To determine which of the two expressions are responsible for this error, a numerical solution was carried out to accurately determine the force of capillary interaction between floating spherical particles. It was found that the asymptotic expression for the capillary attraction loses its accuracy at close range for large particle densities i.e. when their densities are close to the maximum density of a particle that can float. However, for the spherical particles used in our experiments, no significant deviation between the asymptotic predictions and numerical solutions are observed. The numerical solution showed that the force of attraction between these spheres is correctly explained by the asymptotic solution even at small interparticle separations. This shows that the expression for the hydrodynamic interaction between pairs of spheres must be giving rise to errors in this case.

# Chapter 7

## Epilogue

### 7.1 Conclusions

#### **A new numerical solution**

As described in Chapter 1, there are a number of published asymptotic solutions for capillary interaction between objects at liquid interfaces. However, most of these solutions are based on the assumption that the meniscus slopes are small, and simplify the problem by linearizing the Laplace–Young equation and using the linear superposition approximation. The major contribution of this thesis is a numerical solution that does not assume these simplifications, and accurately solves the fully nonlinear Laplace–Young equation with the appropriate nonlinear boundary conditions. The numerical solution was developed using the *hp*-meshless cloud method, which is a meshfree finite difference method. Additionally, two approximate analytical solutions are developed, which independently verify some of the predictions of the numerical results.

#### **Limitations of asymptotic solutions**

Asymptotic solutions for the force of attraction between pairs of objects at liquid interfaces have been already calculated for fixed vertical cylinders with circular cross section and floating spheres (Chan et al., 1981; Kralchevsky and Nagayama, 2000). Following the method developed in these papers, a new asymptotic solution for the attraction between vertical cylinders with elliptical cross section was developed in Chapter 4. The limitations of these solutions were found using the

numerical solution. It was shown that the asymptotic solutions tend to fail as the objects approach each other. For vertical cylinders, this deviation increases as the contact angle deviates from  $90^\circ$ , and for floating spheres, this deviation becomes more significant as the density of the spheres become close to the maximum density of a sphere that can float at the interface without sinking.

### **Discovery of new phenomena**

Using the numerical solution, we also discovered several phenomena that are not predicted by the existing asymptotic solutions. The failure of the asymptotic solution in these cases is due to the limitations of the linear superposition approximation – the numerical solution showed that the collective behaviour of objects at interfaces can be different from the predictions made by combining their behaviour in isolation. As an example, the linear superposition technique leads to the prediction that the interaction between a hydrophilic and a hydrophobic vertical circular cylinder is always repulsive. In Chapter 3, it was shown that this is in general true at large inter-object separations but the interaction can become attractive at very small inter-object separations.

More interesting behaviour was identified with floating spheres, as shown in Chapter 5. Compared to the vertical cylinders, this was a complicated problem because the vertical positions of the spheres and the horizontal projections of the contact lines were not known *a priori*. A new algorithm was developed which successfully solved this problem. We showed that a sphere that is too dense to float in isolation may instead float as part of a pair or of a cluster at intermediate inter-particle distances; we also showed that a sphere that can float in isolation may sink if it is a part of a pair at small inter-particle distances. In previous asymptotic solutions regarding a pair of interacting spheres, the equilibrium configuration of an isolated sphere is calculated first, and the meniscus produced by two such spheres are linearly superimposed upon one another. I developed a new “semi-analytical” solution for a pair or a cluster of spheres using an improved approach, where both the linear superposition and the determination of the equilibrium configuration of the spheres are carried out simultaneously. This produced an equilibrium that depended on the inter-particle distance, and consistently with the numerical solution predicted the floating of highly dense spheres

at intermediate range. However, this solution still had a linear superposition component so that it was unable to predict the sinking of the spheres at short range that is observed in the numerical solutions.

### **Circular cylinders**

In addition to the “semi-analytical” solution, experimental results and new analytical solutions were employed to independently verify the numerical solutions. For the force of attraction between circular cylinders, experimental results published by other groups disagreed with asymptotic solutions at small inter-object separations, but matched very well with the numerical solutions at all distance ranges. These experiments also showed that when a hydrophilic and hydrophobic cylinder approach one another, the magnitude of their repulsive force of interaction initially increases, and then starts to reduce, matching very well with our numerical solution. Ultimately, at very short range, this repulsion becomes an attraction as seen in our simulations.

### **Elliptical cylinders**

The versatility of the numerical solution enabled its extension to solve problems involving anisotropic objects, namely elliptical cylinders, which is described in Chapter 4. A new analytical solution was also developed for this problem by solving for the the meniscus shape around an isolated cylinder using elliptic cylindrical coordinates, and then using linear superposition to calculate the forces of attraction. For isolated elliptical cylinders, both solutions gave very similar contact line and meniscus profiles even when the ratio between the major and minor axes was larger than 27. Both solutions showed that the force of interaction was orientation-dependent and that the force in the tip-to-tip orientation was larger than that in the side-to-side orientation. However, this orientation-dependence becomes significant only at short range (i.e. inter-object distances that are small compared to the capillary length for large cylinders and major axis for small cylinders). This is the same distance range where the analytical solutions start to fail as already mentioned. Therefore, exact agreement between the numerical and analytical results are not observed for the anisotropic interactions. It was also shown that at large distances away from an isolated elliptical cylinder, the

shape of the meniscus was found to be asymptotically equivalent to one created by a circular cylinder with the same perimeter as that of the elliptical cylinder. It was also shown that the force of attraction between a pair of elliptical cylinders at long range was equal to the force of attraction between these “effective” circular cylinders.

### Experiments on spheres

We carried out experiments to measure the force of attraction between floating spheres in Chapter 6. These experiments also showed deviations from the asymptotic solutions at close-range. However, the force inferred from the experimental results also depended on an approximate expression for the hydrodynamic interaction between the spheres. Our numerical simulations showed that for the moderate sphere densities used in these experiments, significant deviations from the asymptotic results are not expected. This suggests that it is the inaccuracy of the expression for the hydrodynamic interaction that leads to the deviations in the measured force compared to that computed.

## 7.2 Outlook

The results presented here open the door to a wide range of future analyses of capillary interaction. The interaction between a pair of vertical circular cylinders was studied in Chapter 3. With respect to “real” scenarios of self assembly, it would be interesting to understand the behaviour of three cylinders, in particular when two cylinders are in fixed positions, what force will a third cylinder feel while approaching them? One would generally expect that this force can be calculated by linear superposition at far-range, but the results in Chapter 3 suggest that there will be deviations at close-range. Moreover, these deviations may occur not only in the magnitude, but also in the direction of the force, and the numerical solution will enable discovery of such new behaviour. A study of this nature would be the first step towards a more rigorous understanding of the structure of capillary aggregates, which have often been supposed to have a fractal nature (Hórvölgyi et al., 1991).

In Chapter 4, we introduced the “effective” radius of a circular cylinder that

approximates the meniscus created by an elliptical cylinder at far-range. It was also shown that the effective circular cylinder had approximately the same perimeter as the elliptical cylinder. It is important to determine whether this simple relationship is also valid for non-elliptical shapes with complex cross sections; such a relationship would be very useful for objects for which analytical solutions are hard to derive. This can be checked by determining the meniscus shapes around such objects by means of the numerical solution method developed in this thesis.

Rapacchietta and Neumann (1977) have shown that a floating isolated sphere can have two equilibrium positions but that only one of them is stable. The study of the interaction between pairs of spheres in Chapter 5 was limited to identical pairs and we found only one stable equilibrium for a given inter-particle distance. However, for a pair of non-identical spheres there can be more than one stable equilibrium, giving rise to different floating behaviours and forces of interaction.

In Chapter 5, the floating and sinking of clusters of spheres was also studied. These clusters were infinite in size, and it would be interesting to understand the floating behaviour of clusters of finite size. This will enable carrying out simple experiments to verify the numerical results. The possibility of carrying out experiments to verify data in the floating and sinking regime diagram (figure 5.8) for a pair of spheres is limited by the fact that the intermediate-range floating and close-range sinking regimes are spread only across a narrow density range. These density ranges depend on the parameters of the spheres, liquid, and the fluid. By varying these parameters, it may be possible to identify a combination where the density ranges involving the new phenomena is wide enough to be experimentally accessible.

Since it is relatively hard to carry out the above experiment using a range of densities for the spheres, I propose a simpler method of experimentally realizing the collective behaviour of spheres at a liquid-fluid interface. Instead of making the spheres sink, this experiment involves pulling them out of a liquid-air interface as shown in figure 7.1. Two identical spheres are connected horizontally at a fixed distance using a rigid connector, and they are slowly pulled upwards from the liquid surface using a string attached to a balance. In the vertical direction, the spheres are affected by 4 forces: weight ( $F_w$ ), surface tension force ( $F_{st}$ )

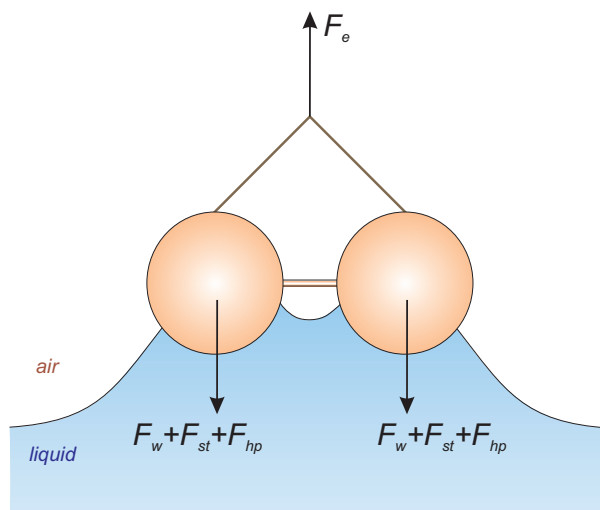


Figure 7.1: A simple experiment to demonstrate that the ability of a particle to remain at a liquid–fluid interface can be affected by the presence of other particles close by. A pair of identical spheres are held at a fixed distance apart with a rigid connector, and they are attached to a liquid–air interface. They slowly are pulled upwards using a string attached to a balance until they separate from the interface. The force exerted by the balance ( $F_e$ ) is continuously recorded. The maximum value of  $F_e$  is equal to the maximum force collectively exerted downwards by surface tension ( $F_{st}$ ), hydrostatic pressure ( $F_{hp}$ ) and particle weight ( $F_w$ ). The experiment is repeated for a range of inter–particle distances, and also carried out using an isolated particle. This data can be used to create an experimental regime diagram showing the maximum external force a pair of particles can support without separating from the liquid–air interface.

and hydrostatic pressure force ( $F_{hp}$ ) which act downwards, and the force exerted upwards by the balance ( $F_e$ ).

$F_e$  changes as the pair of spheres move upwards, and the maximum of this value  $F_{e,max,pair}$  is recorded. This corresponds to the maximum vertical force exerted by the combination of surface tension and hydrostatic pressure. This is very similar to the point of sinking in the scenarios considered in Chapter 5.  $F_{e,max,pair}$  obtained for a pair of spheres at variable inter–particle distances can be then compared with  $F_{e,max,isolated}$ , which is the maximum value of  $F_e$  obtained by repeating this experiment for an isolated sphere.  $F_{e,max,isolated}$  can also be used to calculate the contact angle ( $\theta$ ) making use of the fact that this corresponds to

the maximum of  $F_{st} + F_{hp}$  which are both functions of  $\theta$ . Once  $\theta$  is known, theoretical predictions for  $F_{e,max,pair}$  can be made using numerical or semi-analytical approaches similar to those described in Chapter 5

The experiments on the force of attraction between floating spheres presented in Chapter 6 can be further improved by measuring the contact angles of both types of spherical particles that were used. An accurate (numerical) solution for the hydrodynamic interaction between these particles may allow us to interpret the experimental data better.

Extension of the numerical method and Algorithm 1 presented in Chapter 5 to solve for floating anisotropic objects such as spheroids will enable discovery of a wide range of new phenomena. In doing this, the torque balance and the rotation of the objects will need to be considered. In addition to the floating and sinking behaviour, this will also provide insight into the structures produced by self-assembly of the anisotropic objects.



# References

- M. Abramowitz and I. A. Stegun. *Handbook of Mathematical Functions with Formulas, Graphs, and Mathematical Tables*. Dover, New York, 1964. [36](#), [43](#), [58](#)
- G. Batchelor. Brownian diffusion of particles with hydrodynamic interaction. *Journal of Fluid Mechanics*, 74(01):1–29, 1976. [7](#), [115](#)
- J. Benito, F. Urena, L. Gavete, and R. Alvarez. An h-adaptive method in the generalized finite differences. *Computer Methods in Applied Mechanics and Engineering*, 192(5):735–759, 2003. [19](#), [26](#)
- M. Berhanu and A. Kudrolli. Heterogeneous structure of granular aggregates with capillary interactions. *Physical Review Letters*, 105(9):98002, 2010. [3](#)
- B. Binks and T. S. Horozov. *Colloidal particles at liquid interfaces*. Cambridge University Press, Cambridge (U.K.), 2006. [1](#)
- J. Bleibel, S. Dietrich, A. Domínguez, and M. Oettel. Shock waves in capillary collapse of colloids: A model system for two-dimensional screened newtonian gravity. *Physical Review Letters*, 107(12):128302, 2011. [3](#)
- C. Bloomquist and R. Shutt. Fine particle suspensions in organic liquids. *Industrial & Engineering Chemistry*, 32(6):827–831, 1940. [6](#)
- N. Bowden, A. Terfort, J. Carbeck, and G. Whitesides. Self-assembly of mesoscale objects into ordered two-dimensional arrays. *Science*, 276(5310):233–235, 1997. [4](#), [9](#)

## References

---

- N. Bowden, I. Choi, B. Grzybowski, and G. Whitesides. Mesoscale self-assembly of hexagonal plates using lateral capillary forces: synthesis using the capillary bond. *Journal of the American Chemical Society*, 121(23):5373–5391, 1999. [4](#), [9](#)
- N. Bowden, S. Oliver, and G. Whitesides. Mesoscale self-assembly: capillary bonds and negative menisci. *The Journal of Physical Chemistry B*, 104(12):2714–2724, 2000. [4](#)
- J. Bush and D. Hu. Walking on water: biolocomotion at the interface. *Annual Review of Fluid Mechanics*, 38:339–369, 2006. [81](#)
- J. Bush, D. Hu, and M. Prakash. The integument of water-walking arthropods: form and function. volume 34, pages 117–192. Elsevier, 2007. [81](#)
- H. Butt and M. Kappl. Normal capillary forces. *Advances in Colloid and Interface Science*, 146(1):48–60, 2009. [4](#), [6](#)
- H. Butt, K. Graf, and M. Kappl. *Physics and chemistry of interfaces*. Wiley-VCH, 2003. [11](#), [14](#), [15](#)
- M. Cavallaro Jr, L. Botto, E. Lewandowski, M. Wang, and K. Stebe. Curvature-driven capillary migration and assembly of rod-like particles. *Proceedings of the National Academy of Sciences*, 108(52):20923–20928, 2011. [48](#)
- D. Ceco, P. Kralchevsky, V. Paunov, H. Yoshimura, and K. Nagayama. Torsion balance for measurement of capillary immersion forces. *Langmuir*, 12(3):641–651, 1996. [7](#), [29](#), [32](#), [39](#), [40](#)
- S. Chambert and C. James. Sorting of seeds by hydrochory. *River Research and Applications*, 25(1):48–61, 2008. [2](#)
- D. Chan, J. Henry, and L. White. The interaction of colloidal particles collected at fluid interfaces. *Journal of Colloid and Interface Science*, 79(2):410–418, 1981. [6](#), [7](#), [29](#), [43](#), [82](#), [85](#), [93](#), [115](#), [129](#)

- 
- S. Christophers. Structure of the culex egg and egg-raft in relation to function (diptera). *Transactions of the Royal Entomological Society of London*, 95(2): 25–34, 1945. [2](#)
- P. Cicuta and D. Vella. Granular character of particle rafts. *Physical review letters*, 102(13):138302, 2009. [3](#)
- T. Clark, J. Tien, D. Duffy, K. Paul, and G. Whitesides. Self-assembly of 10- $\mu$ m-sized objects into ordered three-dimensional arrays. *Journal of the American Chemical Society*, 123(31):7677–7682, 2001. [4](#)
- T. Clark, R. Ferrigno, J. Tien, K. Paul, and G. Whitesides. Template-directed self-assembly of 10- $\mu$  m-sized hexagonal plates. *Journal of the American Chemical Society*, 124(19):5419–5426, 2002. [4](#)
- M. Dalbe, D. Cosic, M. Berhanu, and A. Kudrolli. Aggregation of frictional particles due to capillary attraction. *Physical Review E*, 83(5):051403, 2011. [7](#), [82](#), [113](#), [114](#), [115](#)
- K. Danov and P. Kralchevsky. Capillary forces between particles at a liquid interface: General theoretical approach and interactions between capillary multipoles. *Advances in Colloid and Interface Science*, 154(1):91, 2010. [9](#)
- K. Danov, P. Kralchevsky, B. Naydenov, and G. Brenn. Interactions between particles with an undulated contact line at a fluid interface: Capillary multipoles of arbitrary order. *Journal of Colloid and Interface Science*, 287(1):121–134, 2005. [29](#)
- N. Denkov, I. Ivanov, P. Kralchevsky, and D. Wasan. A possible mechanism of stabilization of emulsions by solid particles. *Journal of Colloid and Interface Science*, 150(2):589–593, 1992. [8](#)
- C. Extrand and S. Moon. Using the flotation of a single sphere to measure and model capillary forces. *Langmuir*, 25(11):6239–6244, 2009. [7](#), [82](#)
- X. Gao and L. Jiang. Biophysics: water-repellent legs of water striders. *Nature*, 432(7013):36–36, 2004. [2](#), [81](#)

## References

---

- S. Gart, D. Vella, and S. Jung. The collective motion of nematodes in a thin liquid layer. *Soft Matter*, 7(6):2444–2448, 2011. [7](#)
- T. Gil, J. Ipsen, O. Mouritsen, M. Sabra, M. Sperotto, and M. Zuckermann. Theoretical analysis of protein organization in lipid membranes. *Biochimica et Biophysica Acta (BBA)-Reviews on Biomembranes*, 1376(3):245–266, 1998. [8](#)
- A. Gray. *Modern Differential Geometry of Curves and Surfaces with Mathematica, 2nd ed.* CRC Press, 1998. [14](#)
- Y. Han and M. Kim. Effect of bond and asymmetry of 2d-dumbbells on their structure in high concentration regime. *Soft Matter*, 2012. [3](#)
- S. Herminghaus. Dynamics of wet granular matter. *Advances in Physics*, 54(3):221–261, 2005. [6](#)
- A. Hill and C. Pozrikidis. On the shape of a hydrostatic meniscus attached to a corrugated plate or wavy cylinder. *Journal of Colloid and Interface Science*, 356(2):763–774, 2011. [14](#), [49](#), [59](#)
- H. Hinton. Structure and protective devices of the egg of the mosquito culex pipiens. *Journal of Insect Physiology*, 14(2):145–161, 1968. [2](#)
- Z. Hórvölgyi, G. Medveczky, and M. Zrinyi. Experimental study of the aggregate structures formed in the boundary layer of waterair phases. *Colloids and Surfaces*, 60:79–95, 1991. [3](#), [132](#)
- K. Hosokawa, I. Shimoyama, and H. Miura. Two-dimensional micro-self-assembly using the surface tension of water. *Sensors and Actuators A: Physical*, 57(2):117–125, 1996. [4](#)
- A. Jeffrey. *Handbook of mathematical formulas and integrals.* Academic, 1995. [37](#), [52](#), [54](#)
- J. B. Keller. Surface tension force on a partly submerged body. *Phys. Fluids*, 10(11):3009–3010, 1998. [36](#)

- 
- H. Kim, D. Choi, Y. Kim, S. Baik, and H. Moon. Shape optimization of symmetric cylinder shape on buoyancy using fourier series approximation. *Journal of Fluids Engineering*, 132:051206, 2010. [7](#), [82](#)
- P. Kralchevsky and N. Denkov. Capillary forces and structuring in layers of colloid particles. *Current Opinion in Colloid & Interface Science*, 6(4):383–401, 2001. [4](#), [5](#), [6](#), [9](#)
- P. Kralchevsky and K. Nagayama. Capillary forces between colloidal particles. *Langmuir*, 10(1):23–36, 1994. [7](#)
- P. Kralchevsky, V. Paunov, N. Denkov, I. Ivanov, and K. Nagayama. Energetical and force approaches to the capillary interactions between particles attached to a liquid-fluid interface. *Journal of Colloid and Interface Science*, 155:420–420, 1993. [7](#), [16](#), [29](#), [32](#), [34](#), [37](#)
- P. Kralchevsky, V. Paunov, N. Denkov, and K. Nagayama. Stresses in lipid membranes and interactions between inclusions. *Journal of the Chemical Society, Faraday Transactions*, 91(19):3415–3432, 1995a. [8](#)
- P. A. Kralchevsky and K. Nagayama. Capillary interactions between particles bound to interfaces, liquid films and biomembranes. *Advances in Colloid and Interface Science*, 85(2-3):145 – 192, 2000. ISSN 0001-8686. [4](#), [5](#), [6](#), [129](#)
- P. A. Kralchevsky and K. Nagayama. *Particles at fluid interfaces and membranes: Attachment of colloid particles and proteins to interfaces and formation of two-dimensional arrays*. Elsevier, Amsterdam, 2001. [37](#), [38](#)
- P. A. Kralchevsky, V. N. Paunov, N. D. Denkov, and K. Nagayama. Capillary image forces: I. theory. *Journal of Colloid and Interface Science*, 167(1):47 – 65, 1994. ISSN 0021-9797. [8](#)
- P. A. Kralchevsky, V. N. Paunov, and K. Nagayama. Lateral capillary interaction between particles protruding from a spherical liquid layer. *Journal of Fluid Mechanics*, 299:105–132, 1995b. ISSN 1469-7645. [8](#)

## References

---

- I. Larmour, G. Saunders, and S. Bell. Sheets of large superhydrophobic metal particles self assembled on water by the cheerios effect. *Angewandte Chemie International Edition*, 47(27):5043–5045, 2008. [82](#)
- H. Lehle, E. Noruzifar, and M. Oettel. Ellipsoidal particles at fluid interfaces. *The European Physical Journal E: Soft Matter and Biological Physics*, 26(1):151–160, 2008a. [93](#)
- H. Lehle, E. Noruzifar, and M. Oettel. Ellipsoidal particles at fluid interfaces. *The European Physical Journal E: Soft Matter and Biological Physics*, 26(1):151–160, 2008b. [47](#), [48](#), [66](#)
- E. Lewandowski, J. Bernate, A. Tseng, P. Searson, and K. Stebe. Oriented assembly of anisotropic particles by capillary interactions. *Soft Matter*, 5(4):886–890, 2008. [47](#)
- E. Lewandowski, M. Cavallaro, L. Botto, J. Bernate, V. Garbin, and K. Stebe. Orientation and self-assembly of cylindrical particles by anisotropic capillary interactions. *Langmuir*, 26(19):15142, 2010. [47](#)
- T. J. Liszka, C. A. M. Duarte, and W. W. Tworzydło. hp-meshless cloud method. *Computer Methods in Applied Mechanics and Engineering*, 139(1-4):263 – 288, 1996. ISSN 0045-7825. [18](#), [19](#), [24](#), [30](#), [38](#), [93](#)
- J. Liu, X. Feng, and G. Wang. Buoyant force and sinking conditions of a hydrophobic thin rod floating on water. *Physical Review E*, 76(6):066103, 2007. [82](#)
- X. Liu, X. Wang, Y. Liang, and F. Zhou. Floating behavior of hydrophobic glass spheres. *Journal of Colloid and Interface Science*, 336(2):743–749, 2009. [82](#)
- L. L. Lo. The meniscus on a needle a lesson in matching. *Journal of Fluid Mechanics*, 132:65–78, 1983. [14](#), [35](#), [36](#), [41](#), [96](#), [97](#), [101](#), [102](#)
- J. Loudet and B. Pouligny. Self-assembled capillary arrows. *Europhysics Letters*, 85(2):28003, 2009. [47](#)

- 
- J. Loudet and B. Pouligny. How do mosquito eggs self-assemble on the water surface? *The European Physical Journal E: Soft Matter and Biological Physics*, 34(8):1–17, 2011. [2](#), [47](#)
- J. Loudet, A. Alsayed, J. Zhang, and A. Yodh. Capillary interactions between anisotropic colloidal particles. *Physical Review Letters*, 94(1):18301, 2005. [43](#), [47](#), [48](#), [66](#)
- Y. Lu, J. Song, X. Liu, W. Xu, J. Sun, and Y. Xing. Loading capacity of a self-assembled superhydrophobic boat array fabricated via electrochemical method. *Micro & Nano Letters, IET*, 7(8):786–789, 2012. [82](#)
- J. Lucassen. Capillary forces between solid particles in fluid interfaces. *Colloids and Surfaces*, 65(2):131–137, 1992. [9](#)
- S. Lukaschuk, P. Denissenko, and G. Falkovich. Clustering of floating particles by surface waves. *Journal of Low Temperature Physics*, 145(1):297–310, 2006. [3](#)
- S. Maenosono, C. Dushkin, and Y. Yamaguchi. Direct measurement of the viscous force between two spherical particles trapped in a thin wetting film. *Colloid & Polymer Science*, 277(10):993–996, 1999. [7](#)
- E. Mansfield, H. Sepangi, and E. Eastwood. Equilibrium and mutual attraction or repulsion of objects supported by surface tension. *Philosophical Transactions: Mathematical, Physical and Engineering Sciences*, pages 869–919, 1997. [84](#)
- S. Mansfield, A. Gotch, G. Harms, C. Johnson, and C. Larive. Complementary analysis of peptide aggregation by nmr and time-resolved laser spectroscopy. *The Journal of Physical Chemistry B*, 103(12):2262–2269, 1999. [8](#)
- M. Mastrangeli, S. Abbasi, C. Varel, C. Van Hoof, J. Celis, and K. Böhringer. Self-assembly from milli-to nanoscales: methods and applications. *Journal of Microelectromechanics and Microengineering*, 19(8):083001, 2009. [4](#)
- N. W. McLachlan. *Theory and application of mathieu functions*. Dover, 1964. [55](#), [56](#), [57](#), [68](#)

## References

---

- L. C. Miall. *Round the year - a series of short nature studies*. Macmillan and co., limited, 1898. [2](#)
- M. Nicolson. *The interaction between floating particles*, volume 45. Cambridge Univ Press, 1949. [6](#)
- V. Paunov, P. Kralchevsky, N. Denkov, I. Ivanov, and K. Nagayama. Capillary meniscus interaction between a microparticle and a wall. *Colloids and Surfaces*, 67:119–138, 1992. [8](#)
- V. Paunov, P. Kralchevsky, N. Denkov, and K. Nagayama. Lateral capillary forces between floating submillimeter particles. *Journal of Colloid and Interface Science*, 157(1):100–112, 1993. [6](#)
- J. T. Petkov, N. D. Denkov, K. D. Danov, O. D. Velev, R. Aust, and F. Durst. Measurement of the drag coefficient of spherical particles attached to fluid interfaces. *Journal of colloid and interface science*, 172(1):147–154, 1995. [127](#)
- S. Pickering. Emulsions. *Journal of the Chemical Society*, 91(91):2001–2021, 1907. cited By (since 1996) 60. [8](#)
- J. Poynting and S. Thomson. *A university textbook of physics: volume I, Properties of matter*. C. Griffin, 1947. [42](#)
- C. Pozrikidis. *Fluid dynamics: theory, computation, and numerical simulation*. Springer, 2009. [14](#)
- C. Pozrikidis. Computation of three-dimensional hydrostatic menisci. *IMA Journal of Applied Mathematics*, 75(3):418–438, 2010. [14](#), [30](#), [49](#)
- C. Pozrikidis. A floating prolate spheroid. *Journal of Colloid and Interface Science*, 364(1):248–256, 2011. [14](#)
- A. Rapacchietta and A. Neumann. Force and free-energy analyses of small particles at fluid interfaces: Ii. spheres. *Journal of Colloid and Interface Science*, 59(3):555 – 567, 1977. [83](#), [96](#), [133](#)

- 
- P. Roura. Thermodynamic derivations of the mechanical equilibrium conditions for fluid surfaces: Youngs and Laplace equations. *American Journal of Physics*, 73:1139, 2005. [11](#)
- P. Roura and J. Fort. Local thermodynamic derivation of Young's equation. *Journal of Colloid and Interface Science*, 272(2):420–429, 2004. [15](#)
- Z. Saliternik. The macroscopic differentiation of anopheline eggs according to their pattern on the surface of water. *Bulletin of Entomological Research*, 33(04):221–221, 1942. [2](#), [47](#)
- P. Schiffer. Granular physics: A bridge to sandpile stability. *Nature Physics*, 1(1):21–22, 2005. [6](#)
- K. Scott, T. Hirano, H. Yang, H. Singh, R. Howe, and A. Niknejad. High-performance inductors using capillary based fluidic self-assembly. *Journal of Microelectromechanical Systems*, 13(2):300–309, 2004. [4](#)
- P. Singh and T. Hesla. The interfacial torque on a partially submerged sphere. *Journal of Colloid and Interface Science*, 280(2):542–543, 2004. [17](#)
- U. Srinivasan, M. Helmbrecht, C. Rembe, R. Muller, and R. Howe. Fluidic self-assembly of micromirrors onto microactuators using capillary forces. *IEEE Journal of Selected Topics in Quantum Electronics*, 8(1):4–11, 2002. [4](#)
- D. Stamou, C. Duschl, and D. Johannsmann. Long-range attraction between colloidal spheres at the air-water interface: The consequence of an irregular meniscus. *Physical Review E*, 62(4):5263, 2000. [9](#)
- R. Syms, E. Yeatman, V. Bright, and G. Whitesides. Surface tension-powered self-assembly of microstructures—the state-of-the-art. *Journal of Microelectromechanical Systems*, 12(4):387–417, 2003. [4](#), [47](#)
- N. Vassileva, D. van den Ende, F. Mugele, and J. Mellema. Capillary forces between spherical particles floating at a liquid-liquid interface. *Langmuir*, 21(24):11190–11200, 2005. [7](#), [113](#), [114](#), [115](#)

## References

---

- O. Velev, N. Denkov, V. Paunov, P. Kralchevsky, and K. Nagayama. Direct measurement of lateral capillary forces. *Langmuir*, 9(12):3702–3709, 1993. [7](#), [29](#), [39](#), [41](#)
- O. Velev, N. Denkov, V. Paunov, P. Kralchevsky, and K. Nagayama. Capillary image forces: II. experiment. *Journal of Colloid and Interface Science*, 167(1): 66–73, 1994. [8](#)
- K. Velikov, F. Durst, and O. Velev. Direct observation of the dynamics of latex particles confined inside thinning water-air films. *Langmuir*, 14(5):1148–1155, 1998. [7](#)
- D. Vella. Floating objects with finite resistance to bending. *Langmuir*, 24(16): 8701–8706, 2008. [81](#)
- D. Vella and L. Mahadevan. The “cheerios effect”. *American Journal of Physics*, 73(9):817–825, 2005. doi: 10.1119/1.1898523. [42](#), [43](#), [82](#), [84](#)
- D. Vella, D. Lee, and H. Kim. The load supported by small floating objects. *Langmuir*, 22(14):5979–5981, 2006a. [7](#), [81](#), [82](#), [83](#), [85](#), [100](#)
- D. Vella, P. Metcalfe, and R. Whittaker. Equilibrium conditions for the floating of multiple interfacial objects. *Journal of Fluid Mechanics*, 549:215–224, 2006b. [7](#), [82](#), [106](#), [112](#)
- J. Voise, M. Schindler, J. Casas, and E. Raphaël. Capillary-based static self-assembly in higher organisms. *Journal of The Royal Society Interface*, 8(62): 1357–1366, 2011. [47](#)
- X. Xiong, Y. Hanein, J. Fang, Y. Wang, W. Wang, D. Schwartz, and K. Bohringer. Controlled multibatch self-assembly of microdevices. *Journal of Microelectromechanical Systems*, 12(2):117–127, 2003. [4](#)
- T. Young. An essay on the cohesion of fluids. *Philosophical Transactions of the Royal Society of London*, 95:65–87, 1805. [14](#)

- C. Zeng, F. Brau, B. Davidovitcha, and A. Dinsmorea. Capillary interactions among spherical particles at curved liquid interfaces. *Soft Matter*, 8:8582–8594, 2012. [8](#)